ABSTRACT

Title of dissertation: CHARACTERIZATION OF NONLINEAR WAVEGUIDES FOR ALL-OPTICAL SIGNAL PROCESSING

Jeremiah J. Wathen, Doctor of Philosophy, 2014

Dissertation directed by: Professor Thomas E. Murphy
Department of Electrical & Computer Engineering

This dissertation documents research of the optical properties of chip-based nonlinear waveguides to assess their suitability for all-optical processing in the telecommunications spectrum. Three related topics are presented: (1) enhanced continuous-wave four-wave mixing in AlGaAs waveguides; (2) a new method to characterize nonlinear refraction and loss in waveguides; and (3) the non-instantaneous optical nonlinearity of a hydrogenated amorphous silicon waveguide.

For topic (1), enhancements of the continuous-wave four-wave-mixing efficiency and bandwidth are accomplished by engineering the growth and fabrication of AlGaAs waveguides. The bandgap of the core-layer alloy is tailored to suppress nonlinear absorption and the fabrication is optimized to produce small-mode-area, dispersion-engineered waveguides with sub-dB/cm propagation losses. A four-wave-mixing conversion efficiency of -6.8 dB is observed in an AlGaAs waveguide that exhibits a propagation loss of 0.56 dB/cm. This conversion efficiency is among the highest reported for any passive semiconductor or glass waveguide. Another

low-loss AlGaAs waveguide is featured, which is dispersion-engineered to produce a measured conversion-bandwidth of 63.8 nm with a pump wavelength of 1550 nm.

For topic (2), a new technique is described for accurately measuring the ratio between the imaginary part and the real part of a waveguide's third-order nonlinearity. Unlike most other methods, it does not depend on precise knowledge of the coupling efficiencies, the optical propagation loss, or the optical pulse shape. The method is applied to measure the nonlinear loss tangents of a GaAs waveguide, two bandgap-engineered AlGaAs waveguides, a large-area crystalline silicon waveguide, a crystalline silicon nanowire waveguide, and a hydrogenated amorphous silicon nanowire waveguide.

For topic (3), pump-probe spectroscopy and continuous-wave cross-phase- and cross-amplitude-modulation measurements are used to study the optical nonlinearity of a hydrogenated amorphous silicon nanowire waveguide. The results are compared to those of a crystalline silicon waveguide of similar dimensions. The hydrogenated amorphous silicon nanowire shows essentially zero instantaneous two-photon absorption, but it displays a strong, long-lived non-instantaneous nonlinearity that is both absorptive and refractive. Power-scaling measurements show that the non-instantaneous nonlinearity of the hydrogenated amorphous silicon scales as a third-order nonlinearity. Phase-transient measurements show that the refractive component possesses the opposite sign to that expected for free-carrier dispersion.

CHARACTERIZATION OF NONLINEAR WAVEGUIDES FOR ALL-OPTICAL SIGNAL PROCESSING

by

Jeremiah J. Wathen

Dissertation submitted to the Faculty of the Graduate School of the
University of Maryland, College Park in partial fulfillment
of the requirements for the degree of
Doctor of Philosophy
2014

Advisory Committee:
Professor Thomas E. Murphy, Co-Chair/Co-Advisor
Professor Rajarshi Roy, Co-Chair/Co-Advisor
Professor Brian R. Hunt
Professor Ian Appelbaum
Professor Ki-Yong Kim

for my family

Acknowledgments

When I separated from active duty service in the US Navy in 2010, the obvious choice would have been to do what all my "retiring" shipmates did: join the business world. Instead, I gambled, and at the ripe old age of 30, I pursued a doctorate in physics. In truth, I wasn't especially qualified to do so, and I had no idea what I was in for. Nonetheless, because of the many people who have supported me over the last four years, my decision turned out very well.

I am thankful to the people at the Laboratory for Physical Sciences – Ken Ritter, Chris Richardson, Tim Horton, Paul Petruzzi, Vince Pagán and Gary Carter – who took a chance and brought me aboard. From you, and from my colleagues John Mack, Ryan Suess and Ke-Yao Wang, I have learned so much about doing science and engineering at a professional level. I owe special thanks to Paveen Apiratikul. You taught me patience, tenacity, thoroughness, humility, and everything I know about nonlinear waveguides. Without your Herculean fabrication efforts, there would have been no waveguides to study.

I cannot give enough thanks to Professor Thomas Murphy. Aside from being a truly remarkable scientist, you have been the best possible mentor and academic advisor. You manage to balance the needs of your family and an incredible workload, and yet you still somehow make (lots of) time to work with me and all your other students. When I have finished my degree, I will miss your guidance in all things, academic and otherwise.

I wish to recognize the devoted professors from the physics and electrical and

computer engineering departments who put forth the effort to construct particularly excellent courses, including (in no particular order) Professors James Drake (for math methods and electrodynamics), Julius Goldhar (nonlinear optics), Ian Appelbaum (solid state physics), Edo Waks (quantum electronics), Ed Ott (chaotic dynamics) and Victor Yakovenko (theoretical dynamics). These classes have been especially invaluable to my development as a scientist.

To my parents, thank you and I love you.

I saved the best for last, my wife. Over the past two years, we met, we married, we renovated a bathroom, we built a deck, we sold a house, we bought a house, you got a promotion and a new job... and now you are pregnant with our baby boy. During all of this, you have picked up the slack to let me work nights and weekends to pass the qualifier and to finish my research. I am unbelievably lucky. Thank you. I love you.

Table of Contents

List of Tables

List of Figures

Chapter 1: Introduction

Today's computing devices are limited not by the performance of individual processors, but by the rate at which processors can exchange data with the outside world [1]. During the early 2000s, the old-school approach to achieving performance gains – increasing the processor's clock-frequency and increasing the density of transistors on-chip – began to reach fundamental limits. To maintain *Moore's law* scaling in the performance of individual computing components, the semiconductor industry began to introduce chip multiprocessors (CMPs, also called multi-core processors) [2].

The CMP consists of several individual processor-cores networked together on a single integrated circuit die. Performance gains are reaped by implementing parallel code execution using multiple threads across the cores. This technology has advanced to the point that CMPs now resemble highly parallel computing systems, integrated on a single chip [3]. But scaling-up this approach to continue the pace of progress is leading to new limitations. The central problem now is how to make individual cores in the CMP communicate efficiently, among themselves on-chip, with off-chip components (like RAM), and even over longer-reach rack-to-rack distances; Traditional metallic interconnects can no longer provide the bandwidth and heat-

dissipation requirements necessary to drive what amount to complicated, full-scale networks on a single chip [4].

It is now generally accepted that the future solutions to these problems will, in one form or another, consist of augmenting chip-based electronics with integrated photonics [1–5]. The idea is to shrink to the chip-scale the many advantages that optical fibers have brought to the interconnection of computers at the large scale, most importantly the huge bandwidth and low per-bit-transmitted power-cost. A future CMP might consist of numerous processor-cores, which talk to one another and with RAM via a miniature but full-fledged integrated optical network. Indeed, the concept of the photonic "Network-on-Chip" is so enticing that the Defense Advanced Research Projects Agency (DARPA) is running an active project specifically to address the integration of on-chip photonic components (the project is called "POEM" [6]).

To simplify the operation of proposed integrated photonic systems, there is a strong desire to be able to perform "all-optical" signal processing – switching, routing, multiplexing, de-multiplexing, logic operations, etc. – by operating directly on optical signals in the optical domain. Doing so will prevent slow, power-hungry optical-to-electronic-to-optical (OEO) conversions, which are complicated and space-consuming to implement. To paraphrase Monat et al. in [7], the goal is the complete integration of all-optical signal generation, signal processing, and signal detection on a single chip.

Any all-optical processing scheme will rely on the nonlinear response of the medium to the applied field. Therefore, the viability of chip-based nonlinear pho-

tonics hinges on the ability to engineer and mass produce low-loss sub-micron[1] nonlinear waveguides, which can integrate with existing electronics. For the obvious reason that silicon waveguides can readily integrate with the all-pervasive silicon-on-insulator (SOI) platform, the overwhelming majority of work in this field has focused on using SOI waveguides for nonlinear processing [5, 8]. Fortunately, crystalline silicon is transparent in the telecommunications spectral window (near $\lambda = 1.55$ μm), and it has been possible for a long time to make high-quality, low-loss, dispersion-engineered, sub-micron SOI waveguides.

However, though crystalline silicon waveguides are certainly adequate for many nonlinear photonics applications [9], the material has two key deficiencies. First, it is an indirect-gap semiconductor, and it is therefore difficult to make integrated silicon-based lasers which operate in the telecom spectrum (though some attempts have been successful, see [10]). Second is a deficiency that is highly related to the work presented in this dissertation: nonlinear absorption in the telecommunications spectrum is unavoidable in crystalline silicon – a direct result of the crystal's rather narrow bandgap [11]. Any form of optical loss is problematic for a nonlinear waveguide because loss decreases the applied optical field and therefore diminishes the nonlinear effect.

This dissertation presents experimental studies of the optical nonlinearity of competing semiconductor waveguide systems. The intent is to characterize their utility for chip-based nonlinear optical processing. The focus is mainly on bandgap-engineered AlGaAs waveguides and hydrogenated amorphous silicon waveguides,

[1]Meaning the cross-sectional dimensions are sub-micron in size.

principally because these materials should exhibit the desirable combination of a large nonlinearity and negligible nonlinear absorption. Results obtained from GaAs and SOI waveguides are also presented for comparison.

The dissertation is arranged according to the following format. Chapter 2 explores the basic physics used to describe third-order optical nonlinearities in semiconductor waveguides. It is meant to serve as a nonlinear optics refresher and it culminates with a derivation of the coupled-wave equations which describe continuous-wave four-wave mixing in nonlinear waveguides. These equations are used frequently in the subsequent chapters to model the observed nonlinear responses of waveguides. This chapter lays the foundation for the rest of the work.

Chapter 3 focuses on the nonlinear optical process of wavelength conversion using AlGaAs waveguides. It begins with a description of what wavelength conversion is and why it is needed. A review of the wavelength-conversion performance of other waveguide systems is provided. The experimental and computational apparatus used to characterize the AlGaAs waveguides is fully explained, and the chapter concludes by presenting measurements of the power-dependence and spectral bandwidth of wavelength conversion using continuous-wave four-wave mixing.

Chapter 4 discusses a new experimental method devised to measure the nonlinear loss tangent: the ratio of nonlinear loss to nonlinear refraction in a waveguide. The nonlinear loss tangent is a key parameter that determines the suitability of a material or waveguide for nonlinear optical processing. The method is applied to measure the nonlinear loss tangents of four waveguides, where one is composed of GaAs, two more are composed of AlGaAs alloys, and a fourth is composed of crys-

talline silicon. The test of the crystalline silicon waveguide is used as a benchmark to verify the validity and accuracy of the technique.

Chapter 5 presents several measurements of the delayed nonlinear response of a hydrogenated amorphous silicon waveguide. This material system, which is a relative newcomer to nonlinear photonics, is thought to be very promising because it is compatible with the SOI platform and it possesses negligible two-photon absorption. The measurements presented in Chap. 5 confirm that the waveguide lacks instantaneous nonlinear absorption, but that it does demonstrate strong, long-lived, delayed nonlinear absorption. The observations show that the nature and origin of the delayed nonlinearity of hydrogenated amorphous silicon is more complex than is ordinarily assumed for crystalline silicon, and that existing models for the nonlinearity must be re-examined before the material can be deemed suitable for nonlinear optical processing.

Chapter 6 gives a conclusion to the dissertation. The major results of this work are summarized, and the importance of these results is explained in the larger context of chip-based nonlinear photonics. Several directions for future work are outlined, pertaining to both nonlinear AlGaAs waveguides and nonlinear hydrogenated amorphous silicon waveguides.

Chapter 2: Third-Order Nonlinearity in Optical Waveguides

2.1 Overview

This chapter explores the basic physics used to describe third-order optical nonlinearities in waveguides. It begins with discussion as to how an applied electromagnetic field induces a nonlinear polarization in a medium. The polarization is then inserted into Maxwell's equations to derive the nonlinear wave equation, which describes how the nonlinear polarization feeds-back to the applied field.

A specific scenario is worked out in detail: the interaction of three monochromatic fields in a nonlinear waveguide. Starting from first principles, simplified coupled-wave equations are derived to describe this situation. These equations and the discussion leading to them are useful for understanding the experimental results documented in the subsequent chapters. The physical origins of relevant nonlinear processes – two-photon absorption, Kerr refraction, free-carrier absorption and free-carrier dispersion – are discussed in the context of semiconductor waveguides operating at telecommunications wavelengths.

2.2 The Nonlinear Polarization

For a linear and time-invariant dielectric medium, an applied electric field $\mathbf{E}(t)$ induces a polarization, $\mathbf{P}(t)$, according to a convolution integral of the form

$$P_j(t) = \epsilon_0 \int_{-\infty}^{\infty} \chi_{jk}(\tau) E_k(t-\tau)\,\mathrm{d}\tau \tag{2.1}$$

where ϵ_0 is the free-space permittivity and Einstein notation has been used for compactness. Here, the linear susceptibility χ_{jk} is a second-rank tensor (in a 3D space) that, roughly speaking, is a proportionality constant relating the component of the polarization pointing in the $\hat{j}$-direction to the components of the applied field pointing in each of the $\hat{k}$-directions. The dependence of χ_{jk} on the time-argument τ indicates the "memory" of the system: the polarization occurring at time t depends on the instantaneous electric field at t, but also on the electric field that was present before t. Applying the Fourier transform to translate Eq. (2.1) into frequency space, it becomes

$$\hat{P}_j(\omega) = \epsilon_0 \chi_{jk}(\omega) \hat{E}_k(\omega) \tag{2.2}$$

where $\hat{P}_j(\omega)$ and $\hat{E}_k(\omega)$ represent the Fourier transforms[1] of $P_j(t)$ and $E_k(t)$, respectively. Likewise – even though it lacks a "hat" in this notation – the tensor $\chi_{jk}(\omega)$ is the Fourier transform of the time-domain impulse response $\chi_{jk}(t)$. In the time domain, $\chi_{jk}(t)$ relates the two real-valued functions $P_j(t)$ and $E_k(t)$, and must therefore be real-valued itself. In turn, in the frequency domain, the elements of $\chi_{jk}(\omega)$

[1]The following conventions are adopted for the Fourier transform (FT) and its inverse (IFT):

$$\text{FT: } \hat{F}(\omega) \equiv \int_{-\infty}^{\infty} F(t) e^{i\omega t}\,\mathrm{d}t \qquad\qquad \text{IFT: } F(t) \equiv \frac{1}{2\pi} \int_{-\infty}^{\infty} \hat{F}(\omega) e^{-i\omega t}\,\mathrm{d}\omega$$

are permitted to be complex but are restricted such that $[\chi_{jk}(\omega)]^* = \chi_{jk}(-\omega)$.

When the applied field becomes sufficiently strong, the dependence of the polarization on the electric field becomes nonlinear. As a conceptual guide, the nonlinear polarization tends to become important when the strength of the applied electric force approaches that of the attractive electric forces among electrons and nuclei inside the atoms or molecules comprising the medium. At this point, the restoring forces supplied to charges in the dielectric begin to deviate significantly from *Hooke's Law*. The polarization can be expanded in powers of the applied field,

$$\mathbf{P}(t) = \mathbf{P}^{(1)}(t) + \mathbf{P}^{(2)}(t) + \mathbf{P}^{(3)}(t) + ... \tag{2.3}$$

where $\mathbf{P}^{(n)}(t)$ is the n^{th}-order response in the applied field.

The first term on the RHS of Eq. (2.3) represents the linear response of the medium via the linear susceptibility according to Eq. (2.1). The subsequent terms represent the various orders of the nonlinear response. In general, the n^{th}-order term in the expansion of the polarization relates to the applied field via a nonlinear susceptibility tensor of rank $n+1$. For a time-invariant medium, the n^{th}-order polarization is given by

$$P_j^{(n)}(t) = \epsilon_0 \int \cdots \int \chi_{jx_1\ldots x_n}(\tau_1, \ldots, \tau_n) E_{x_1}(t-\tau_1) \ldots E_{x_n}(t-\tau_n)\, \mathrm{d}\tau_1 \ldots \mathrm{d}\tau_n \tag{2.4}$$

This dissertation mainly deals with third-order nonlinear phenomena, which are manifest by the third-order polarization, $P_j^{(3)}(t)$.[2] The third-order nonlinearity of a material is characterized by its third-order susceptibility, which is sometimes

[2]Non-centrosymmetric crystals (like AlGaAs) also exhibit second-order nonlinearities via the second-order polarization, $P_j^{(2)}(t)$. However, it is typically difficult to phase-match second-order processes and we therefore neglect to address them here.

written as $\chi^{(3)}$ and sometimes as χ_{jklm}. The $\chi^{(3)}$ of a given medium is a rank-4 tensor consisting of 81 elements (though the number of distinct, non-zero elements can be reduced using symmetry arguments). As a special case of Eq. (2.4), the third-order polarization is described by the following triple convolution integral

$$P_j^{(3)}(t) = \epsilon_0 \iiint \chi_{jklm}(\tau_1, \tau_2, \tau_3) E_k(t-\tau_1) E_l(t-\tau_2) E_m(t-\tau_3)\, \mathrm{d}\tau_1 \mathrm{d}\tau_2 \mathrm{d}\tau_3 \quad (2.5)$$

It is sometimes easiest to work with the nonlinear polarization expressed in the frequency domain. This can be achieved by first Fourier-transforming Eq. (2.5) to obtain

$$\begin{aligned} \hat{P}_j^{(3)}(\omega) &= \epsilon_0 \iiint \chi_{jklm}(\tau_1, \tau_2, \tau_3) \\ &\quad \times E_k(t-\tau_1) E_l(t-\tau_2) E_m(t-\tau_3) e^{i\omega t}\, \mathrm{d}\tau_1 \mathrm{d}\tau_2 \mathrm{d}\tau_3 \mathrm{d}t, \end{aligned} \quad (2.6)$$

and then substituting the inverse-Fourier-transform representations of E_k, E_l and E_m:

$$\begin{aligned} \hat{P}_j^{(3)}(\omega) &= \frac{\epsilon_0}{4\pi^2} \int \mathrm{d}\omega_1 \int \mathrm{d}\omega_2 \int \mathrm{d}\omega_3\, \hat{E}_k(\omega_1) \hat{E}_l(\omega_2) \hat{E}_m(\omega_3) \\ &\quad \times \left[\iiint \chi_{jklm}(\tau_1, \tau_2, \tau_3) e^{i(\omega_1\tau_1 + \omega_2\tau_2 + \omega_3\tau_3)}\, \mathrm{d}\tau_1 \mathrm{d}\tau_2 \mathrm{d}\tau_3 \right] \\ &\quad \times \left[\frac{1}{2\pi} \int e^{i(\omega - \omega_1 - \omega_2 - \omega_3)t}\, \mathrm{d}t \right] \end{aligned} \quad (2.7)$$

where the first bracketed quantity in Eq. (2.7) is identified as the frequency-domain version of the third-order susceptibility,

$$\chi_{jklm}(\omega_1, \omega_2, \omega_3) \equiv \iiint \chi_{jklm}(\tau_1, \tau_2, \tau_3) e^{i(\omega_1\tau_1 + \omega_2\tau_2 + \omega_3\tau_3)}\, \mathrm{d}\tau_1 \mathrm{d}\tau_2 \mathrm{d}\tau_3 \quad (2.8)$$

Using the delta function identity, $\frac{1}{2\pi} \int e^{i\nu t} \mathrm{d}t = \delta(\nu)$, along with the definition of the

frequency-domain susceptibility, Eq. (2.7) simplifies to

$$\hat{P}_j^{(3)}(\omega) = \frac{\epsilon_0}{4\pi^2} \iiint \chi_{jklm}(\omega_1, \omega_2, \omega_3) \hat{E}_k(\omega_1) \hat{E}_l(\omega_2) \hat{E}_m(\omega_3) \times \delta(\omega - \omega_1 - \omega_2 - \omega_3)\, \mathrm{d}\omega_1 \mathrm{d}\omega_2 \mathrm{d}\omega_3 \tag{2.9}$$

This is the frequency-domain expression for the third-order polarization, analogous to the time-domain expression given in Eq. (2.5). Written in this form, it is more clear that the third-order polarization has interesting properties – the integral in Eq. (2.9) mixes the input frequencies in various combinations. Unlike the linear polarization, the third-order polarization can contain terms that oscillate at new frequencies, distinct from any of the frequencies of the input electromagnetic waves.

2.3 The Nonlinear Wave Equation

The preceding section briefly described how an electromagnetic wave polarizes a medium. This section deals with how, once induced, the polarization couples back to the field. The medium is assumed to be non-magnetic (i.e., $\mathbf{B} = \mu_0 \mathbf{H}$) and sourceless, as is the case with the materials studied for this dissertation. The starting point is Maxwell's equations:

$$\nabla \cdot \mathbf{D}(\mathbf{r}, t) = 0 \tag{2.10}$$

$$\nabla \times \mathbf{E}(\mathbf{r}, t) = -\frac{\partial \mathbf{B}(\mathbf{r}, t)}{\partial t} \tag{2.11}$$

$$\nabla \cdot \mathbf{B}(\mathbf{r}, t) = 0 \tag{2.12}$$

$$\nabla \times \mathbf{H}(\mathbf{r}, t) = \frac{\partial \mathbf{D}(\mathbf{r}, t)}{\partial t} \tag{2.13}$$

The vector displacement, $\mathbf{D}(\mathbf{r}, t)$, contains the polarization according to the con-

stitutive relation

$$\mathbf{D}(\mathbf{r},t) = \epsilon_0 \mathbf{E}(\mathbf{r},t) + \mathbf{P}(\mathbf{r},t), \tag{2.14}$$

where, in general, the polarization includes linear and nonlinear terms:

$$\mathbf{P}(\mathbf{r},t) = \mathbf{P}^{(1)}(\mathbf{r},t) + \mathbf{P}^{(\mathrm{NL})}(\mathbf{r},t) \tag{2.15}$$

The $\mathbf{P}^{(1)}(\mathbf{r},t)$ considered here is the same linear polarization stated in Eq. (2.1) (but generalized to include spatial dependence).

The wave equation is derived by combining Eqs. (2.11) and (2.13) to calculate $\nabla \times \nabla \times \mathbf{E}$,

$$\nabla \times \nabla \times \mathbf{E}(\mathbf{r},t) + \mu_0 \frac{\partial^2}{\partial t^2} \mathbf{D}(\mathbf{r},t) = 0 \tag{2.16}$$

and then using Eq. (2.14) to eliminate $\mathbf{D}(\mathbf{r},t)$:

$$\nabla \times \nabla \times \mathbf{E}(\mathbf{r},t) + \mu_0 \frac{\partial^2}{\partial t^2} \left[\epsilon_0 \mathbf{E}(\mathbf{r},t) + \mathbf{P}(\mathbf{r},t)\right] = 0 \tag{2.17}$$

The role of the nonlinear polarization is made explicit by using Eq. (2.15)

$$\nabla \times \nabla \times \mathbf{E}(\mathbf{r},t) + \mu_0 \frac{\partial^2}{\partial t^2} \left[\epsilon_0 \mathbf{E}(\mathbf{r},t) + \mathbf{P}^{(1)}(\mathbf{r},t)\right] = -\mu_0 \frac{\partial^2}{\partial t^2} \mathbf{P}^{(\mathrm{NL})}(\mathbf{r},t) \tag{2.18}$$

Equation (2.18) is the general form of the nonlinear wave equation expressed in the time domain, but it can usually be simplified further. The vector formula $\nabla \times \nabla \times \mathbf{E}(\mathbf{r},t) = \nabla(\nabla \cdot \mathbf{E}(\mathbf{r},t)) - \nabla^2 \mathbf{E}(\mathbf{r},t)$ can be used to expand the first term in Eq. (2.18). Luckily, in most cases of practical interest, the quantity $\nabla(\nabla \cdot \mathbf{E}(\mathbf{r},t))$ is either identically zero as is the case for plane-waves, or is much smaller than the quantity $-\nabla^2 \mathbf{E}(\mathbf{r},t)$ [12]. Therefore, Eq. (2.18) typically reduces to (or approximates to)

$$\nabla^2 \mathbf{E}(\mathbf{r},t) - \mu_0 \frac{\partial^2}{\partial t^2} \left[\epsilon_0 \mathbf{E}(\mathbf{r},t) + \mathbf{P}^{(1)}(\mathbf{r},t)\right] = \mu_0 \frac{\partial^2}{\partial t^2} \mathbf{P}^{(\mathrm{NL})}(\mathbf{r},t) \tag{2.19}$$

Consider the theoretical limit of a lossless, dispersionless, optically isotropic medium. In this case, the linear portion of the vector displacement, $\mathbf{D}^{(1)} = \epsilon_0\mathbf{E}(\mathbf{r},t)+\mathbf{P}^{(1)}(\mathbf{r},t)$, relates to the applied electric field via a scalar, real, dimensionless, frequency-independent relative permittivity, ϵ_r, according to $\epsilon_0\mathbf{E}(\mathbf{r},t)+\mathbf{P}^{(1)}(\mathbf{r},t) = \epsilon_0\epsilon_r\mathbf{E}(\mathbf{r},t)$. This allows further simplification of Eq. (2.19) to the form

$$\nabla^2\mathbf{E}(\mathbf{r},t) - \frac{n^2}{c^2}\frac{\partial^2}{\partial t^2}\mathbf{E}(\mathbf{r},t) = \mu_0\frac{\partial^2}{\partial t^2}\mathbf{P}^{(\mathrm{NL})}(\mathbf{r},t) \tag{2.20}$$

where $n = \sqrt{\epsilon_r}$ is the refractive index of this idealized non-magnetic, isotropic, dispersionless, lossless medium. In the form of Equation (2.20), it is particularly obvious that the nonlinear polarization acts as a driving term to the usual linear wave equation.

For the more general case of a dissipative, dispersive, anisotropic medium, the relative permittivity must be treated as a complex, frequency-dependent tensor of rank 2. However, in the experiments presented later, the interacting waves are always polarized along only one of the waveguide's polarization eigenstates. So in the following derivation of the coupled-wave equations, the relative permittivity will be treated simply as a (real) scalar quantity, which describes the frequency-dependent refractive index specific to a particular polarization eigenstate. Optical loss will be accounted by phenomenologically inserting loss into the equations once the derivation is complete.

2.4 The Coupled-Wave Equations for Four-Wave Mixing

In this section, the third-order polarization is inserted into the nonlinear wave equation to construct coupled nonlinear differential equations. There are many possible $\chi^{(3)}$ processes – e.g., third-harmonic generation, stimulated Brillouin scattering, stimulated Raman scattering, etc. Specifically, this section constructs the coupled-wave equations necessary to describe the processes of self-phase modulation (SPM), self-amplitude modulation, cross-phase modulation (XPM), cross-amplitude modulation (XAM), and partially degenerate continuous-wave four-wave mixing (FWM).

The equations we are about to derive are commonly stated as a starting point in many academic papers related to this dissertation (e.g., [13–15] and many more) and they are useful to describe the results presented later. By construction, they describe the interactions among three waves, conventionally called the pump, the signal, and the idler waves. As is the case in many of the experiments presented later, the waves are assumed to be approximately monochromatic, occurring at the frequencies ω_p, ω_s and ω_i, respectively. The complete derivation of the equations is given to highlight important physics and to point out all the assumptions inherent to the derivation.

In partially degenerate four-wave mixing, the pump wave and the signal wave interact via the third-order polarization to generate the idler at a distinct frequency. From a quantum mechanics perspective, partially degenerate four-wave mixing happens when two pump photons with frequency ω_p are annihilated and an idler and a signal photon are generated with frequencies ω_i and ω_s, respectively (the inverse

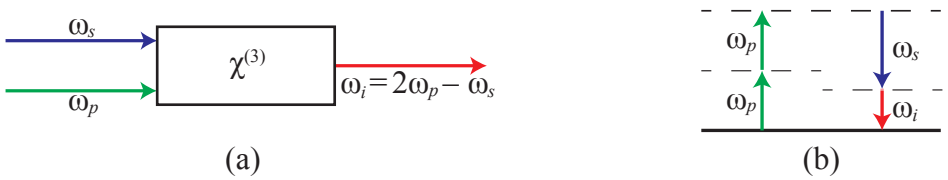

Figure 2.1: (a) Geometry of partially degenerate four-wave mixing. (b) Energy-level diagram describing partially degenerate four-wave mixing.

is also possible). The process, which is illustrated schematically in Fig. 2.1, will occur in a $\chi^{(3)}$-medium as long as energy conservation and momentum conservation (a.k.a. "phase-matching") are satisfied. Thus, from the outset, we will enforce energy conservation and set $\omega_i = 2\omega_p - \omega_s$. The requirements for phase-matching will naturally fall out of the derivation and are discussed in detail in Sect. 3.6.

For monochromatic fields, it is easiest to work with the time-domain polarization, which is found by applying the inverse Fourier transform to Eq. (2.9):

$$\begin{aligned} P_j^{(3)}(\mathbf{r},t) &= \frac{\epsilon_0}{8\pi^3}\iiint \chi_{jklm}(\omega_1,\omega_2,\omega_3) \\ &\quad \times \hat{E}_k(\mathbf{r},\omega_1)\hat{E}_l(\mathbf{r},\omega_2)\hat{E}_m(\mathbf{r},\omega_3)e^{-i(\omega_1+\omega_2+\omega_3)t}\,\mathrm{d}\omega_1\mathrm{d}\omega_2\mathrm{d}\omega_3 \end{aligned} \tag{2.21}$$

The electric field is assumed to be a superposition of monochromatic fields,

$$E_j(\mathbf{r},t) = \frac{1}{2}\sum_{\omega_n>0}\left[E_j(\mathbf{r},\omega_n)e^{-i\omega_n t} + E_j^*(\mathbf{r},\omega_n)e^{i\omega_n t}\right] \tag{2.22}$$

where the complex amplitude $E_j(\mathbf{r},\omega_n)$ includes the label ω_n in parentheses as a reminder that it represents the component of the field oscillating at frequency ω_n. Eventually, we will restrict ω_n to belong to the set $\{\omega_p,\omega_s,\omega_i\}$, but we will keep the discussion more general for the moment. In this notation, all the spatial dependence of the field has been absorbed into the complex amplitude. Applying the Fourier

transform to Eq. (2.22) yields

$$\hat{E}_j(\mathbf{r},\omega) = \pi \sum_{\omega_n>0} \left[E_j(\mathbf{r},\omega_n)\delta(\omega-\omega_n) + E_j^*(\mathbf{r},\omega_n)\delta(\omega+\omega_n) \right] \tag{2.23}$$

Now we can insert Eq. (2.23) into Eq. (2.21) to obtain

$$\begin{aligned} P_j^{(3)}(\mathbf{r},t) \;=\; & \frac{\epsilon_0}{8} \sum_{\omega_\lambda} \sum_{\omega_\mu} \sum_{\omega_\nu} \iiint \chi_{jklm}(\omega_a,\omega_b,\omega_c) e^{-i(\omega_a+\omega_b+\omega_c)t} \\ & \times [E_k(\mathbf{r},\omega_\lambda)\delta(\omega_a-\omega_\lambda) + E_k^*(\mathbf{r},\omega_\lambda)\delta(\omega_a+\omega_\lambda)] \\ & \times [E_l(\mathbf{r},\omega_\mu)\delta(\omega_b-\omega_\mu) + E_l^*(\mathbf{r},\omega_\mu)\delta(\omega_b+\omega_\mu)] \\ & \times [E_m(\mathbf{r},\omega_\nu)\delta(\omega_c-\omega_\nu) + E_m^*(\mathbf{r},\omega_\nu)\delta(\omega_c+\omega_\nu)] \; \mathrm{d}\omega_a \mathrm{d}\omega_b \mathrm{d}\omega_c \end{aligned} \tag{2.24}$$

where the sums extend only over positive frequencies. Computing the integrals in Eq. (2.24) leaves the following expression

$$\begin{aligned} P_j^{(3)}(\mathbf{r},t) = \frac{\epsilon_0}{8} \sum_{\omega_\lambda,\omega_\mu,\omega_\nu} \Big\{ & \chi_{jklm}(\omega_\lambda,\omega_\mu,\omega_\nu) E_k(\mathbf{r},\omega_\lambda) E_l(\mathbf{r},\omega_\mu) E_m(\mathbf{r},\omega_\nu) e^{-i(\omega_\lambda+\omega_\mu+\omega_\nu)t} \\ & + \chi_{jklm}(\omega_\lambda,\omega_\mu,-\omega_\nu) E_k(\mathbf{r},\omega_\lambda) E_l(\mathbf{r},\omega_\mu) E_m^*(\mathbf{r},\omega_\nu) e^{-i(\omega_\lambda+\omega_\mu-\omega_\nu)t} \\ & + \chi_{jklm}(\omega_\lambda,-\omega_\mu,\omega_\nu) E_k(\mathbf{r},\omega_\lambda) E_l^*(\mathbf{r},\omega_\mu) E_m(\mathbf{r},\omega_\nu) e^{-i(\omega_\lambda-\omega_\mu+\omega_\nu)t} \\ & + \chi_{jklm}(\omega_\lambda,-\omega_\mu,-\omega_\nu) E_k(\mathbf{r},\omega_\lambda) E_l^*(\mathbf{r},\omega_\mu) E_m^*(\mathbf{r},\omega_\nu) e^{-i(\omega_\lambda-\omega_\mu-\omega_\nu)t} \\ & + \chi_{jklm}(-\omega_\lambda,\omega_\mu,\omega_\nu) E_k^*(\mathbf{r},\omega_\lambda) E_l(\mathbf{r},\omega_\mu) E_m(\mathbf{r},\omega_\nu) e^{-i(-\omega_\lambda+\omega_\mu+\omega_\nu)t} \\ & + \chi_{jklm}(-\omega_\lambda,\omega_\mu,-\omega_\nu) E_k^*(\mathbf{r},\omega_\lambda) E_l(\mathbf{r},\omega_\mu) E_m^*(\mathbf{r},\omega_\nu) e^{-i(-\omega_\lambda+\omega_\mu-\omega_\nu)t} \\ & + \chi_{jklm}(-\omega_\lambda,-\omega_\mu,\omega_\nu) E_k^*(\mathbf{r},\omega_\lambda) E_l^*(\mathbf{r},\omega_\mu) E_m(\mathbf{r},\omega_\nu) e^{-i(-\omega_\lambda-\omega_\mu+\omega_\nu)t} \\ & + \chi_{jklm}(-\omega_\lambda,-\omega_\mu,-\omega_\nu) E_k^*(\mathbf{r},\omega_\lambda) E_l^*(\mathbf{r},\omega_\mu) E_m^*(\mathbf{r},\omega_\nu) e^{-i(-\omega_\lambda-\omega_\mu-\omega_\nu)t} \Big\} \end{aligned} \tag{2.25}$$

In the time domain, $\chi^{(3)}(\tau_1,\tau_2,\tau_3)$ is purely real. This implies the following symmetry for the frequency-domain $\chi^{(3)}$

$$[\chi_{jklm}(\omega_\lambda,\omega_\mu,\omega_\nu)]^* = \chi_{jklm}(-\omega_\lambda,-\omega_\mu,-\omega_\nu) \tag{2.26}$$

In other words, taking the complex conjugate of the frequency-domain susceptibility is equivalent to reversing the sign associated with each of its frequency arguments. Using Eq. (2.26), Eq. (2.25) simplifies to

$$\begin{aligned} P_j^{(3)}(\mathbf{r},t) = \frac{\epsilon_0}{8} \sum_{\omega_\lambda,\omega_\mu,\omega_\nu} \big\{ & \chi_{jklm}(\omega_\lambda,\omega_\mu,\omega_\nu) E_k(\mathbf{r},\omega_\lambda) E_l(\mathbf{r},\omega_\mu) E_m(\mathbf{r},\omega_\nu) e^{-i(\omega_\lambda+\omega_\mu+\omega_\nu)t} \\ & + \chi_{jklm}(\omega_\lambda,\omega_\mu,-\omega_\nu) E_k(\mathbf{r},\omega_\lambda) E_l(\mathbf{r},\omega_\mu) E_m^*(\mathbf{r},\omega_\nu) e^{-i(\omega_\lambda+\omega_\mu-\omega_\nu)t} \\ & + \chi_{jklm}(\omega_\lambda,-\omega_\mu,\omega_\nu) E_k(\mathbf{r},\omega_\lambda) E_l^*(\mathbf{r},\omega_\mu) E_m(\mathbf{r},\omega_\nu) e^{-i(\omega_\lambda-\omega_\mu+\omega_\nu)t} \\ & + \chi_{jklm}(-\omega_\lambda,\omega_\mu,\omega_\nu) E_k^*(\mathbf{r},\omega_\lambda) E_l(\mathbf{r},\omega_\mu) E_m(\mathbf{r},\omega_\nu) e^{-i(-\omega_\lambda+\omega_\mu+\omega_\nu)t} \\ & + \text{c.c.} \big\} \end{aligned} \tag{2.27}$$

where "c.c." represents the complex conjugates of the preceding terms.

It is now assumed that the electromagnetic field consists of only 3 frequency components: ω_p, ω_s and ω_i $(= 2\omega_p - \omega_s)$. In general, other frequency components will be generated via the $\chi^{(3)}$ nonlinear interaction. For example, third-harmonic generation will lead to new field components at $3\omega_p$, $3\omega_s$ and $3\omega_i$. However, unless care is taken to ensure phase matching for the generation of a specific new frequency component, it will typically remain very weak and can therefore be neglected (this is the same reason we are neglecting to consider second-order nonlinear processes here). The inserted field is defined to be

$$E_j(\mathbf{r},t) = \frac{1}{2} E_j(\mathbf{r},\omega_p) e^{-i\omega_p t} + \frac{1}{2} E_j(\mathbf{r},\omega_s) e^{-i\omega_s t} + \frac{1}{2} E_j(\mathbf{r},\omega_i) e^{-i\omega_i t} + \text{c.c.} \tag{2.28}$$

A similar notation is adopted to describe the third-order polarization in terms of its constituent Fourier components

$$P_j^{(3)}(\mathbf{r},t) = \frac{1}{2} \sum_{\omega_n} \left[P_j^{(3)}(\mathbf{r},\omega_n) e^{-i\omega_n t} + \text{c.c.} \right] \tag{2.29}$$

After inserting Eq. (2.28) into Eq. (2.27), the third-order polarization is found to contain 108 terms (and their complex conjugates). In the case considered here, the frequency components of interest are those which oscillate at ω_p, ω_s and ω_i. As an example, consider $P_j^{(3)}(\mathbf{r},\omega_p)$, the complex amplitude of the component ringing at ω_p. This component contains 21 terms (plus complex conjugates), but for brevity, only the first three terms are given here:

$$\begin{aligned} P_j^{(3)}(\mathbf{r},\omega_p) = &\frac{\epsilon_0}{4}\chi_{jklm}(-\omega_p;\omega_p,\omega_p,-\omega_p)E_k(\mathbf{r},\omega_p)E_l(\mathbf{r},\omega_p)E_m^*(\mathbf{r},\omega_p) \\ &+\frac{\epsilon_0}{4}\chi_{jklm}(-\omega_p;\omega_p,-\omega_p,\omega_p)E_k(\mathbf{r},\omega_p)E_l^*(\mathbf{r},\omega_p)E_m(\mathbf{r},\omega_p) \\ &+\frac{\epsilon_0}{4}\chi_{jklm}(-\omega_p;-\omega_p,\omega_p,\omega_p)E_k^*(\mathbf{r},\omega_p)E_l(\mathbf{r},\omega_p)E_m(\mathbf{r},\omega_p) \\ &+ 18 \text{ more terms} + \text{c.c.} \end{aligned} \tag{2.30}$$

A new frequency label has now been inserted into each $\chi_{jklm}(\omega_\sigma;\omega_\lambda,\omega_\mu,\omega_\nu)$, appearing before each semicolon. This label is not a functional argument – it is a bookkeeping device to keep track of the oscillation-frequency generated by that term. Energy conservation requires that $\omega_\sigma+\omega_\lambda+\omega_\mu+\omega_\nu=0$.

The nonlinear susceptibilities $\chi_{jklm}(\omega_\sigma;\omega_\lambda,\omega_\mu,\omega_\nu)$ exhibit intrinsic permutation symmetry [12]. This means that the three indices (k,l,m) may be permuted so long as the corresponding frequency arguments $(\omega_\lambda,\omega_\mu,\omega_\nu)$ are permuted in the same way. For example, applying intrinsic permutation symmetry allows the three terms shown in Eq. (2.30) to be re-written as one:

$$\frac{3\epsilon_0}{4}\chi_{jklm}(-\omega_p;\omega_p,\omega_p,-\omega_p)E_k(\mathbf{r},\omega_p)E_l(\mathbf{r},\omega_p)E_m^*(\mathbf{r},\omega_p)$$

After applying intrinsic permutation symmetry to simplify $P_j^{(3)}(\mathbf{r},\omega_p)$, $P_j^{(3)}(\mathbf{r},\omega_s)$

and $P_j^{(3)}(\mathbf{r},\omega_i)$ as much as possible, they reduce to the following forms:

$$\begin{aligned}
P_j^{(3)}(\mathbf{r},\omega_p) =& \frac{3\epsilon_0}{4}\chi_{jklm}(-\omega_p;\omega_p,\omega_p,-\omega_p)E_k(\mathbf{r},\omega_p)E_l(\mathbf{r},\omega_p)E_m^*(\mathbf{r},\omega_p) \\
&+\frac{3\epsilon_0}{2}\chi_{jklm}(-\omega_p;\omega_p,\omega_s,-\omega_s)E_k(\mathbf{r},\omega_p)E_l(\mathbf{r},\omega_s)E_m^*(\mathbf{r},\omega_s) \\
&+\frac{3\epsilon_0}{2}\chi_{jklm}(-\omega_p;\omega_p,\omega_i,-\omega_i)E_k(\mathbf{r},\omega_p)E_l(\mathbf{r},\omega_i)E_m^*(\mathbf{r},\omega_i) \\
&+\frac{3\epsilon_0}{2}\chi_{jklm}(-\omega_p;\omega_s,\omega_i,-\omega_p)E_k(\mathbf{r},\omega_s)E_l(\mathbf{r},\omega_i)E_m^*(\mathbf{r},\omega_p)
\end{aligned} \tag{2.31a}$$

$$\begin{aligned}
P_j^{(3)}(\mathbf{r},\omega_s) =& \frac{3\epsilon_0}{4}\chi_{jklm}(-\omega_s;\omega_s,\omega_s,-\omega_s)E_k(\mathbf{r},\omega_s)E_l(\mathbf{r},\omega_s)E_m^*(\mathbf{r},\omega_s) \\
&+\frac{3\epsilon_0}{2}\chi_{jklm}(-\omega_s;\omega_s,\omega_p,-\omega_p)E_k(\mathbf{r},\omega_s)E_l(\mathbf{r},\omega_p)E_m^*(\mathbf{r},\omega_p) \\
&+\frac{3\epsilon_0}{2}\chi_{jklm}(-\omega_s;\omega_s,\omega_i,-\omega_i)E_k(\mathbf{r},\omega_s)E_l(\mathbf{r},\omega_i)E_m^*(\mathbf{r},\omega_i) \\
&+\frac{3\epsilon_0}{4}\chi_{jklm}(-\omega_s;\omega_p,\omega_p,-\omega_i)E_k(\mathbf{r},\omega_p)E_l(\mathbf{r},\omega_p)E_m^*(\mathbf{r},\omega_i)
\end{aligned} \tag{2.31b}$$

$$\begin{aligned}
P_j^{(3)}(\mathbf{r},\omega_i) =& \frac{3\epsilon_0}{4}\chi_{jklm}(-\omega_i;\omega_i,\omega_i,-\omega_i)E_k(\mathbf{r},\omega_i)E_l(\mathbf{r},\omega_i)E_m^*(\mathbf{r},\omega_i) \\
&+\frac{3\epsilon_0}{2}\chi_{jklm}(-\omega_i;\omega_i,\omega_p,-\omega_p)E_k(\mathbf{r},\omega_i)E_l(\mathbf{r},\omega_p)E_m^*(\mathbf{r},\omega_p) \\
&+\frac{3\epsilon_0}{2}\chi_{jklm}(-\omega_i;\omega_i,\omega_s,-\omega_s)E_k(\mathbf{r},\omega_i)E_l(\mathbf{r},\omega_s)E_m^*(\mathbf{r},\omega_s) \\
&+\frac{3\epsilon_0}{4}\chi_{jklm}(-\omega_i;\omega_p,\omega_p,-\omega_s)E_k(\mathbf{r},\omega_p)E_l(\mathbf{r},\omega_p)E_m^*(\mathbf{r},\omega_s)
\end{aligned} \tag{2.31c}$$

Inserting Eqs. (2.31a-c) and (2.28) into the nonlinear wave equation results in an equation for each Fourier component,

$$\nabla\times\nabla\times E_j\left(\mathbf{r},\omega_\sigma\right)-\epsilon\left(\omega_\sigma\right)\mu_0\omega_\sigma^2E_j(\mathbf{r},\omega_\sigma)=\mu_0\omega_\sigma^2P_j^{(3)}(\mathbf{r},\omega_\sigma) \tag{2.32}$$

where $\sigma\in\{p,s,i\}$. We will assume that the frequency-dependent permittivity, $\epsilon(\omega_\sigma)\equiv\epsilon_0[1+\chi^{(1)}(-\omega_\sigma;\omega_\sigma)]$, is approximately a purely real quantity. We will also treat it as a scalar quantity, because the materials studied in this dissertation are

optically isotropic. As discussed previously, this allows the substantial simplification $\nabla \times \nabla \times \mathbf{E}(\mathbf{r}, \omega_\sigma) \approx -\nabla^2 \mathbf{E}(\mathbf{r}, \omega_\sigma)$, which leaves us with

$$\nabla^2 E_j(\mathbf{r}, \omega_\sigma) + \frac{n_0^2 \omega_\sigma^2}{c^2} E_j(\mathbf{r}, \omega_\sigma) = -\mu_0 \omega_\sigma^2 P_j^{(3)}(\mathbf{r}, \omega_\sigma) \tag{2.33}$$

where n_0 represents the frequency-dependent refractive index of the medium. When Eq. (2.33) is applied to a waveguide as opposed to a bulk medium, n_0 becomes a spatially varying quantity, which is different for the various layers comprising the waveguide.

Our ultimate intent is to apply the coupled-wave equations to nonlinear processes in semiconductor ridge or channel waveguides, where the various frequency components of the field propagate along the longitudinal axis of the waveguide (the z-direction), confined laterally to the waveguide's optical eigenmodes. The waveguides studied for this dissertation tend to support only a single guided mode, or at most just a few guided modes. Additionally, the rectangular geometry of the waveguides causes the fundamental mode to split into two orthogonal, non-degenerate polarization eigenstates, one of which is quasi-transverse-electric (TE; $E_z \approx 0$ everywhere) and the other quasi-transverse-magnetic (TM; $B_z \approx 0$ everywhere). To reflect the experimental conditions of the measurements presented later, we will assume from here on that all of the waves excite only the fundamental TE mode of the waveguide.

Omitting the nonlinear perturbation, Eq. (2.33) becomes

$$\nabla^2 E_j(\mathbf{r}, \omega_\sigma) + \frac{n_0^2 \omega_\sigma^2}{c^2} E_j(\mathbf{r}, \omega_\sigma) = 0, \tag{2.34}$$

By assuming that all the field-components display a z-dependence of $\exp(i\beta_j z)$,

this eigenvalue equation can be solved to give the frequency-dependent effective propagation constant, $\beta_j(\omega_\sigma)$, and transverse mode shape, $f_j(x, y, \omega_\sigma)$, of the unperturbed waveguide. As discussed in Sect. 2.4.1, the waveguides considered later exhibit complex geometries (relative to, say, a cylindrically symmetrical step-index optical fiber), so computational techniques are used to find the approximate effective propagation constants (i.e., the $\beta_j(\omega_\sigma)$'s) and eigenfunctions of each waveguide.

In practice, the nonlinear polarization is usually only a small perturbation to the linear wave equation. We therefore assume the shape of the mode, to first order, is unaffected by the nonlinear perturbation to the refractive index. This assumption is especially justified for the type of highly confining waveguides studied for this dissertation, where the peak nonlinear change in the refractive index might be only a few parts in 1000 relative to the unperturbed core-cladding index difference. This assumption allows us to write the electric field of the perturbed system as

$$E_j(\mathbf{r}, \omega_\sigma) \approx f_j(x, y, \omega_\sigma) A_j(z, \omega_\sigma) \tag{2.35}$$

We have explicitly included the dependence of $f(x, y, \omega)$ on ω for completeness. Later, we will ignore its ω-dependence in the vicinity of some central frequency. (In Eq. (2.35), the subscript j on the RHS is not an Einstein-index. It is simply a label to associate $f_j(x, y, \omega_\sigma)$ with the j^{th} component of $\mathbf{A}(z, \omega_\sigma)$. Any confusion potentially caused by this mixing of conventions will be eliminated in a moment by using the polarization unit vectors.)

Inserting Eq. (2.35) into Eq. (2.33), multiplying through by $f_j^*(x, y, \omega_\sigma)$ and

integrating over the transverse plane gives

$$\frac{\partial^2}{\partial z^2}A_j(z,\omega_\sigma)+\beta_j^2(\omega_\sigma)A_j(z,\omega_\sigma)=-\mu_0\omega_\sigma^2\frac{\iint f_j^*(x,y,\omega_\sigma)P_j^{(3)}(\mathbf{r},\omega_\sigma)\,\mathrm{d}x\mathrm{d}y}{\iint|f_j(x,y,\omega_\sigma)|^2\,\mathrm{d}x\mathrm{d}y} \tag{2.36}$$

where $\beta_j(\omega_\sigma)$ is the frequency-dependent eigenvalue. Again, in practice, a finite-difference modesolver is used to determine the eigenvalue (discussed in Sec. 2.4.1), but it can be expressed using the following integral equation:

$$\beta_j^2(\omega_\sigma)\equiv\frac{\iint f_j^*(x,y,\omega_\sigma)\nabla_\mathrm{T}^2 f_j(x,y,\omega_\sigma)\,\mathrm{d}x\mathrm{d}y}{\iint|f_j(x,y,\omega_\sigma)|^2\,\mathrm{d}x\mathrm{d}y}+\frac{\omega_\sigma^2\iint n_0^2(x,y,\omega_\sigma)\,|f_j(x,y,\omega_\sigma)|^2\,\mathrm{d}x\mathrm{d}y}{c^2\iint|f_j(x,y,\omega_\sigma)|^2\,\mathrm{d}x\mathrm{d}y}$$

where $\nabla_\mathrm{T}^2=\frac{\partial^2}{\partial x^2}+\frac{\partial^2}{\partial y^2}$ is the transverse Laplacian operator and n_0 represents the spatially varying material refractive index.

We now assume that any changes in the field due to the effects of the nonlinear polarization occur on a scale much longer than the optical wavelength, in which case:

$$\frac{\partial}{\partial z}A_j(z,\omega_\sigma)\approx i\beta_j(\omega_\sigma)A_j(z,\omega_\sigma) \tag{2.37}$$

In other words, we are assuming that the complex amplitude of the wave and the refractive index change very slowly in z. We may therefore ignore any backward-propagating waves (i.e., reflected waves) and reduce Eq. (2.36) from second-order to first-order via the slowly varying envelope approximation (SVEA):

$$\frac{\partial^2}{\partial z^2}+\beta_j^2(\omega_\sigma)=\big(\frac{\partial}{\partial z}+i\beta_j(\omega_\sigma)\big)\big(\frac{\partial}{\partial z}-i\beta_j(\omega_\sigma)\big)\approx 2i\beta_j(\omega_\sigma)(\frac{\partial}{\partial z}-i\beta_j(\omega_\sigma)) \tag{2.38}$$

Inserting Eq. (2.38) into Eq. (2.36), we obtain

$$\frac{\partial}{\partial z}A_j(z,\omega_\sigma)=i\beta_j(\omega_\sigma)A_j(z,\omega_\sigma)+i\frac{\mu_0\omega_\sigma^2}{2\beta_j(\omega_\sigma)}\frac{\iint f_j^*(x,y,\omega_\sigma)P_j^{(3)}(\mathbf{r},\omega_\sigma)\,\mathrm{d}x\mathrm{d}y}{\iint|f_j(x,y,\omega_\sigma)|^2\,\mathrm{d}x\mathrm{d}y} \tag{2.39}$$

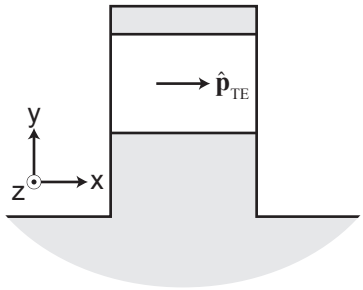

Figure 2.2: The cross-section of a typical ridge waveguide. The coordinate-system is chosen such that the z-axis is the direction of propagation and the x-axis is aligned horizontally, in the same direction as the electric field of the TE eigenstate.

Or, if we choose to break $A_j(z,\omega_\sigma)$ into its slow- and fast-varying parts using $A_j(z,\omega_\sigma) = a_j(z,\omega_\sigma)\exp(i\beta_j(\omega_\sigma)z)$, we can write

$$\frac{\partial}{\partial z}a_j(z,\omega_\sigma) = i\frac{\mu_0\omega_\sigma^2}{2\beta_j(\omega_\sigma)}\frac{\iint f_j^*(x,y,\omega_\sigma)P_j^{(3)}(\mathbf{r},\omega_\sigma)\,\mathrm{d}x\mathrm{d}y}{\iint|f_j(x,y,\omega_\sigma)|^2\,\mathrm{d}x\mathrm{d}y}e^{-i\beta_j(\omega_\sigma)z} \tag{2.40}$$

In all the experiments presented later, light is launched into the waveguide-under-test so as to excite only the fundamental TE eigenstate. Thus the state-of-polarization of the light remains linearly polarized, and does not rotate as a function of distance along the waveguide. Formally, the polarization of each field is accounted for using

$$\mathbf{a}(z,\omega_p) = \hat{\mathbf{p}}_p a_p(z) \qquad \mathbf{a}(z,\omega_s) = \hat{\mathbf{p}}_s a_s(z) \qquad \mathbf{a}(z,\omega_i) = \hat{\mathbf{p}}_i a_i(z) \tag{2.41}$$

where the $\hat{\mathbf{p}}$'s represent polarization unit vectors. By construction, the polarization unit vectors are all aligned parallel to the TE eigenstate:

$$\hat{\mathbf{p}}_p = \hat{\mathbf{p}}_s = \hat{\mathbf{p}}_i = \hat{\mathbf{p}}_{\mathrm{TE}} \tag{2.42}$$

where $\hat{\mathbf{p}}_{\mathrm{TE}}$ is the polarization unit vector which points parallel to the direction of the E-field of the TE eigenstate. For all the waveguides presented later, this happens to be the horizontal dimension. In general, the polarization unit vectors are defined to have unit length such that, for example,

$$\hat{\mathbf{p}}_p^* \cdot \hat{\mathbf{p}}_p = 1 \tag{2.43}$$

In our case, the complex conjugate symbol in Eq. (2.43) is unnecessary because the polarization unit vectors are describing linearly polarized light, and they can be chosen to be purely real. Following the coordinate system defined in Fig. 2.2, which is the convention that will be used throughout this dissertation, we will associate $\hat{\mathbf{p}}_{\mathrm{TE}}$ with the $\hat{\mathbf{x}}$ unit vector: $\hat{\mathbf{p}}_{\mathrm{TE}} = \hat{\mathbf{x}}$.

We now identify $f_j(x, y, \omega_\sigma)$ as the transverse mode distribution of the TE eigenstate for the Fourier component at ω_σ. To simplify things further, we assume the distribution is frequency-independent in the spectral range of interest. We can therefore assign a single distribution to describe the transverse mode, independent of the optical frequency: $f_{\mathrm{TE}}(x, y) \equiv f_{\mathrm{TE}}(x, y, \omega_s) \approx f_{\mathrm{TE}}(x, y, \omega_i) \approx f_{\mathrm{TE}}(x, y, \omega_p)$. Likewise, we identify $\beta_j(\omega_\sigma)$ as the eigenvalue associated with the TE eigenstate, and re-label it $\beta_{\mathrm{TE}}(\omega_\sigma)$, where

$$\beta_{\mathrm{TE}}(\omega_\sigma) = n_{\mathrm{TE}}(\omega_\sigma)\frac{\omega_\sigma}{c} \tag{2.44}$$

and $n_{\mathrm{TE}}(\omega_\sigma)$ is the frequency-dependent effective refractive index of the waveguide's TE eigenstate.

To follow the common convention, we choose to re-normalize the amplitudes appearing in Eq. (2.41). All equations will now be cast in terms of the normalized

fields $u_m(z)$ with $m \in \{p, s, i\}$ such that $|u_m(z)|^2$ represents the total power in the wave according to the prescription

$$\begin{aligned} |u_m(z)|^2 = P_m = \int I_m \,\mathrm{d}x\mathrm{d}y \\ = \frac{1}{2} n_{\mathrm{TE}}(\omega_m)\epsilon_0 c \iint |f_{\mathrm{TE}}(x,y)|^2 |a_m(z)|^2 \,\mathrm{d}x\mathrm{d}y \end{aligned} \tag{2.45}$$

where P_m is the total power carried by u_m and I_m is the intensity. In other words, for all the $E_j(\mathbf{r}, \omega_m)$ appearing in Eqs. (2.31), we have

$$\mathbf{E}(\mathbf{r}, \omega_m) = \frac{\sqrt{2} f_{\mathrm{TE}} \hat{\mathbf{p}}_{\mathrm{TE}} u_m(z) e^{i\beta_{\mathrm{TE}}(\omega_m) z}}{\sqrt{n_{\mathrm{TE}}(\omega_m)\epsilon_0 c}\left[\iint |f_{\mathrm{TE}}|^2 \,\mathrm{d}x\mathrm{d}y\right]^{1/2}} \tag{2.46}$$

where, again, $m \in \{p, s, i\}$, and the spatial dependence of f_{TE} has been suppressed for brevity.

Using Eqs. (2.41)–(2.46), we can now re-write (as an example) Eq. (2.31a) in the following form:

$$\begin{aligned} \mathbf{P}^{(3)}(\mathbf{r}, \omega_p) = & \frac{3}{\sqrt{2\epsilon_0}} \frac{\chi_{jklm}(-\omega_p; \omega_p, \omega_p, -\omega_p) \hat{p}_{\mathrm{TE}\,k}\, \hat{p}_{\mathrm{TE}\,l}\, \hat{p}^*_{\mathrm{TE}\,m}}{\left(n_{\mathrm{TE}}(\omega_p) c\right)^{3/2}} \\ & \times \frac{f_{\mathrm{TE}} |f_{\mathrm{TE}}|^2}{[\iint |f_{\mathrm{TE}}|^2 \,\mathrm{d}x\mathrm{d}y]^{3/2}} |u_p|^2 u_p \exp\{i\beta_{\mathrm{TE}}(\omega_p) z\} \\ & + 2\frac{3}{\sqrt{2\epsilon_0}} \frac{\chi_{jklm}(-\omega_p; \omega_p, \omega_s, -\omega_s) \hat{p}_{\mathrm{TE}\,k}\, \hat{p}_{\mathrm{TE}\,l}\, \hat{p}^*_{\mathrm{TE}\,m}}{\sqrt{n_{\mathrm{TE}}(\omega_p)} n_{\mathrm{TE}}(\omega_s) c^{3/2}} \\ & \times \frac{f_{\mathrm{TE}} |f_{\mathrm{TE}}|^2}{[\iint |f_{\mathrm{TE}}|^2 \,\mathrm{d}x\mathrm{d}y]^{3/2}} |u_s|^2 u_p \exp\{i\beta_{\mathrm{TE}}(\omega_p) z\} \\ & + 2\frac{3}{\sqrt{2\epsilon_0}} \frac{\chi_{jklm}(-\omega_p; \omega_p, \omega_i, -\omega_i) \hat{p}_{\mathrm{TE}\,k}\, \hat{p}_{\mathrm{TE}\,l}\, \hat{p}^*_{\mathrm{TE}\,m}}{\sqrt{n_{\mathrm{TE}}(\omega_p)} n_{\mathrm{TE}}(\omega_i) c^{3/2}} \\ & \times \frac{f_{\mathrm{TE}} |f_{\mathrm{TE}}|^2}{[\iint |f_{\mathrm{TE}}|^2 \,\mathrm{d}x\mathrm{d}y]^{3/2}} |u_i|^2 u_p \exp\{i\beta_{\mathrm{TE}}(\omega_p) z\} \\ & + 2\frac{3}{\sqrt{2\epsilon_0}} \frac{\chi_{jklm}(-\omega_p; \omega_s, \omega_i, -\omega_p) \hat{p}_{\mathrm{TE}\,k}\, \hat{p}_{\mathrm{TE}\,l}\, \hat{p}^*_{\mathrm{TE}\,m}}{\sqrt{n_{\mathrm{TE}}(\omega_p) n_{\mathrm{TE}}(\omega_s) n_{\mathrm{TE}}(\omega_i)} c^{3/2}} \\ & \times \frac{f_{\mathrm{TE}} |f_{\mathrm{TE}}|^2}{[\iint |f_{\mathrm{TE}}|^2 \,\mathrm{d}x\mathrm{d}y]^{3/2}} u_p^* u_s u_i \exp\left\{i\big(\beta_{\mathrm{TE}}(\omega_s) + \beta_{\mathrm{TE}}(\omega_i) - \beta_{\mathrm{TE}}(\omega_p)\big) z\right\} \end{aligned} \tag{2.47}$$

Similar re-normalized equations exist for Eqs. (2.31b) and (2.31c). As long as the dispersion of the waveguide is relatively small, the effective refractive index will not change substantially over the spectral range of interest. We are then justified to replace the refractive indexes appearing in the denominators of Eq. (2.47) with a single effective refractive index for the TE eigenstate, $n_{\mathrm{TE}} \equiv n_{\mathrm{TE}}(\omega_p) \approx n_{\mathrm{TE}}(\omega_s) \approx n_{\mathrm{TE}}(\omega_i)$. Using the re-normalized versions of Eqs. (2.31) and Eqs. (2.41)–(2.46) in Eq. (2.39), we arrive at the following coupled-wave equations:

$$\begin{aligned}\frac{\mathrm{d}u_p}{\mathrm{d}z} &= i\frac{3\omega_p}{4\epsilon_0 n_{\mathrm{TE}}^2 c^2}\chi^{(3)}_{\mathrm{xxxx}}(-\omega_p;\omega_p,\omega_p,-\omega_p)\frac{|u_p|^2}{A_{\mathrm{eff}}}u_p \\ &+ i2\frac{3\omega_p}{4\epsilon_0 n_{\mathrm{TE}}^2 c^2}\chi^{(3)}_{\mathrm{xxxx}}(-\omega_p;\omega_p,\omega_s,-\omega_s)\frac{|u_s|^2}{A_{\mathrm{eff}}}u_p \\ &+ i2\frac{3\omega_p}{4\epsilon_0 n_{\mathrm{TE}}^2 c^2}\chi^{(3)}_{\mathrm{xxxx}}(-\omega_p;\omega_p,\omega_i,-\omega_i)\frac{|u_i|^2}{A_{\mathrm{eff}}}u_p \\ &+ i2\frac{3\omega_p}{4\epsilon_0 n_{\mathrm{TE}}^2 c^2}\chi^{(3)}_{\mathrm{xxxx}}(-\omega_p;\omega_s,\omega_i,-\omega_p)\frac{1}{A_{\mathrm{eff}}}u_p^* u_s u_i e^{i\Delta\beta z}\end{aligned} \tag{2.48a}$$

$$\begin{aligned}\frac{\mathrm{d}u_s}{\mathrm{d}z} &= i\frac{3\omega_s}{4\epsilon_0 n_{\mathrm{TE}}^2 c^2}\chi^{(3)}_{\mathrm{xxxx}}(-\omega_s;\omega_s,\omega_s,-\omega_s)\frac{|u_s|^2}{A_{\mathrm{eff}}}u_s \\ &+ i2\frac{3\omega_s}{4\epsilon_0 n_{\mathrm{TE}}^2 c^2}\chi^{(3)}_{\mathrm{xxxx}}(-\omega_s;\omega_s,\omega_p,-\omega_p)\frac{|u_p|^2}{A_{\mathrm{eff}}}u_s \\ &+ i2\frac{3\omega_s}{4\epsilon_0 n_{\mathrm{TE}}^2 c^2}\chi^{(3)}_{\mathrm{xxxx}}(-\omega_s;\omega_s,\omega_i,-\omega_i)\frac{|u_i|^2}{A_{\mathrm{eff}}}u_s \\ &+ i\frac{3\omega_s}{4\epsilon_0 n_{\mathrm{TE}}^2 c^2}\chi^{(3)}_{\mathrm{xxxx}}(-\omega_s;\omega_p,\omega_p,-\omega_i)\frac{1}{A_{\mathrm{eff}}}u_p^2 u_i^* e^{-i\Delta\beta z}\end{aligned} \tag{2.48b}$$

$$\begin{aligned}\frac{\mathrm{d}u_i}{\mathrm{d}z} &= i\frac{3\omega_i}{4\epsilon_0 n_{\mathrm{TE}}^2 c^2}\chi^{(3)}_{\mathrm{xxxx}}(-\omega_i;\omega_i,\omega_i,-\omega_i)\frac{|u_i|^2}{A_{\mathrm{eff}}}u_i \\ &+ i2\frac{3\omega_i}{4\epsilon_0 n_{\mathrm{TE}}^2 c^2}\chi^{(3)}_{\mathrm{xxxx}}(-\omega_i;\omega_i,\omega_p,-\omega_p)\frac{|u_p|^2}{A_{\mathrm{eff}}}u_i \\ &+ i2\frac{3\omega_i}{4\epsilon_0 n_{\mathrm{TE}}^2 c^2}\chi^{(3)}_{\mathrm{xxxx}}(-\omega_i;\omega_i,\omega_s,-\omega_s)\frac{|u_s|^2}{A_{\mathrm{eff}}}u_i \\ &+ i\frac{3\omega_i}{4\epsilon_0 n_{\mathrm{TE}}^2 c^2}\chi^{(3)}_{\mathrm{xxxx}}(-\omega_i;\omega_p,\omega_p,-\omega_s)\frac{1}{A_{\mathrm{eff}}}u_p^2 u_s^* e^{-i\Delta\beta z}\end{aligned} \tag{2.48c}$$

where $\Delta\beta \equiv \beta_{\mathrm{TE}}(\omega_s) + \beta_{\mathrm{TE}}(\omega_s) - 2\beta_{\mathrm{TE}}(\omega_p)$ is the local wave-vector mismatch and A_{eff} represents the third-order effective mode area of the TE eigenstate, defined by

$$A_{\mathrm{eff}} \equiv \frac{\left[\iint |f_{\mathrm{TE}}|^2 \,\mathrm{d}x\mathrm{d}y\right]^2}{\iint |f_{\mathrm{TE}}|^4 \,\mathrm{d}x\mathrm{d}y} \tag{2.49}$$

2.4.1 Calculating the modes of semiconductor waveguides

A publicly available modesolver called WGMODES [16] is used to compute the modes of the waveguides studied in this dissertation. WGMODES solves the eigenvalue equation

$$\nabla \times (\epsilon^{-1} \nabla \times \mathbf{H}) - \omega^2 \mu_0 \mathbf{H} = 0 \tag{2.50}$$

which is the magnetic field analog to Eq. (2.34) (generalized to allow for an optically anisotropic medium). The modesolver assumes that each field-component exhibits a z-dependence of $\exp(i\beta z)$. It then uses a full-vector finite-difference method to determine the waveguide's frequency-dependent effective propagation constant, $\beta(\omega)$, and the two transverse components of the magnetic field, H_x and H_y, at all vertices in the computational mesh [17]. (The modesolver is designed to solve for components of $\mathbf{H}$ rather than $\mathbf{E}$ because enforcing the zero-divergence condition on $\mathbf{H}$ ensures against spurious modes.) All other components of the electromagnetic fields are subsequently calculated from H_x and H_y. Once calculated, the numerical representation of the eigenfunction is used to estimate the effective mode area by numerically integrating Eq. (2.49).

To calculate the modes of a particular waveguide, the eigenvalue problem is specified by the user-defined 2D computational mesh, which represents the permit-

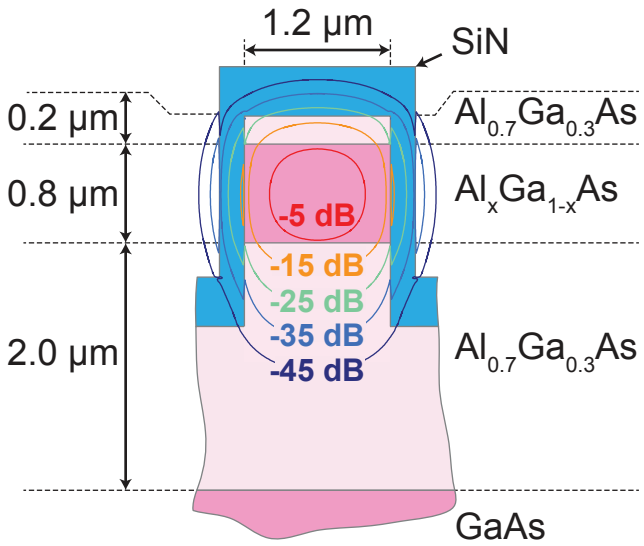

Figure 2.3: An example of the calculated TE mode of an AlGaAs waveguide for the case $x = 0.17$. The contours depict the magnitude of the horizontal component of the electric field in dB relative to the peak value at the center of the core.

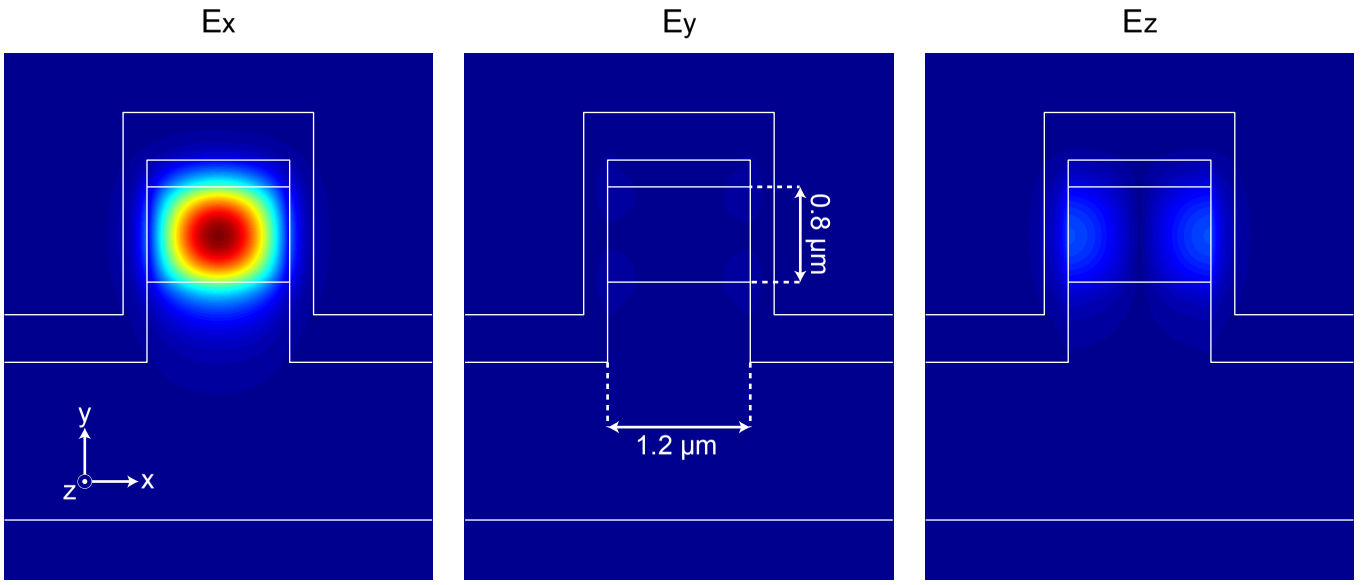

Figure 2.4: False color images depicting each of the orthogonal components of the electric field for the fundamental TE mode. This structure is the same as that pictured in Fig. 2.3.

tivity as a function of the transverse coordinates, x and y. The materials studied for this dissertation are all optically isotropic, so their permittivity tensors reduce to scalar quantities, which significantly reduces the computational expense of the problem.

The modesolver is used extensively in the following chapter to calculate the dispersion properties of AlGaAs ridge waveguides, which is discussed further in Sect. 3.3.2. For these waveguides, an empirical model constructed by Gehrsitz et al., is used to specify the wavelength- and mole-fraction-dependence of AlGaAs's refractive index [18]. As an example, Fig. 2.3 shows the horizontal component (i.e., the x-component) of the electric field, calculated for the TE mode of an AlGaAs waveguide where the mole-fraction of aluminum in the core layer is $x = 0.17$. Related pictures of the x-, y- and z-components of the electric field for the TE mode of the same structure are shown in Fig. 2.4. The y- and z-components of the field are very weak, and the E-field of the TE mode essentially consists of only a horizontal component.

2.5 The Scalar Effective Susceptibilities, Nonlinear Absorption and Nonlinear Refraction

We return now to considering the coupled-wave equations, Eqs (2.48a-c). The $\chi^{(3)}_{xxxx}$'s appearing in these equations are the scalar effective susceptibilities for these particular third-order wave-mixing processes, where all of the waves are co-polarized along the x-direction. The scalar effective susceptibilities are obtained from the χ_{jklm}

tensor by contracting it using the polarization unit vectors:

$$\chi^{(3)}_{(\mathrm{eff})}(\omega_\sigma;\omega_\lambda,\omega_\mu,\omega_\nu) \equiv \chi_{jklm}(\omega_\sigma;\omega_\lambda,\omega_\mu,\omega_\nu)\,\hat{p}^*_{\mathrm{TE}\,j}\,\hat{p}_{\mathrm{TE}\,k}\,\hat{p}_{\mathrm{TE}\,l}\,\hat{p}^*_{\mathrm{TE}\,m} \tag{2.51}$$

Here, we have re-named $\chi^{(3)}_{\mathrm{xxxx}}$ as $\chi^{(3)}_{(\mathrm{eff})}$ to emphasize that similar contracted versions exist for other scalar effective susceptibilities (for example, $\chi^{(3)}_{\mathrm{yyyy}}$ would be the scalar effective susceptibility for the case where all the waves excite the TM eigenstate). In general, the scalar effective susceptibility is a complex quantity, $\chi^{(3)}_{(\mathrm{eff})} = \chi^{(3)}_{(\mathrm{eff})\,R} + i\chi^{(3)}_{(\mathrm{eff})\,I}$. Roughly speaking, the real part of $\chi^{(3)}_{(\mathrm{eff})}$ accounts for processes which introduce a nonlinear phase change to the optical wave (i.e., nonlinear refraction), while the imaginary part accounts for processes which introduce a nonlinear change in the magnitude (i.e., nonlinear absorption or gain, depending on the sign of $\chi^{(3)}_{(\mathrm{eff})\,I}$).

To illustrate the nonlinear effects caused by the scalar effective susceptibility, consider a single quasi-continuous-wave optical beam with frequency ω propagating in the TE eigenstate. In this simple case, the signal and idler amplitudes may be set equal to zero and Eqs. (2.48) reduce to

$$\frac{\mathrm{d}u}{\mathrm{d}z} = i\frac{3\omega}{4\epsilon_0 n^2_{\mathrm{TE}} c^2}\chi^{(3)}_{(\mathrm{eff})}(-\omega;\omega,\omega,-\omega)\frac{|u|^2}{A_{\mathrm{eff}}}u \tag{2.52}$$

Representing the complex amplitude in phasor notation, $u(z) = m(z)e^{i\phi(z)}$, where m is the z-dependent magnitude and ϕ the z-dependent phase, we can split Eq. (2.52) into its real and imaginary parts to obtain

$$\frac{\mathrm{d}m}{\mathrm{d}z} = -\frac{3\omega\chi^{(3)}_{(\mathrm{eff})\,I}}{4\epsilon_0 n^2_{\mathrm{TE}} c^2}\frac{m^3}{A_{\mathrm{eff}}} \qquad\qquad \frac{\mathrm{d}\phi}{\mathrm{d}z} = \frac{\omega}{c}\left(\frac{3\chi^{(3)}_{(\mathrm{eff})\,R}}{4\epsilon_0 n^2_{\mathrm{TE}} c}\right)\frac{m^2}{A_{\mathrm{eff}}} \tag{2.53}$$

Recalling that m^2 is normalized to equal the power of the wave, we can recast Eqs. (2.53) in terms of the z-dependent average intensity defined as $I(z) \equiv P(z)/A_{\text{eff}}$:

$$\frac{\mathrm{d}I}{\mathrm{d}z} = -\left(\frac{3\omega\chi^{(3)}_{(\text{eff})\,I}}{2\epsilon_0 n_{\text{TE}}^2 c^2}\, I\right) I \qquad\qquad \frac{\mathrm{d}\phi}{\mathrm{d}z} = \frac{\omega}{c}\left(\frac{3\chi^{(3)}_{(\text{eff})\,R}}{4\epsilon_0 n_{\text{TE}}^2 c}\, I\right) \tag{2.54}$$

Equations (2.54) show that the third-order polarization leads to intensity-dependent modifications of the waveguide's absorption and refraction, where the quantities $3\omega\chi^{(3)}_{(\text{eff})\,I}\, I/\left(2\epsilon_0 n_{\text{TE}}^2 c^2\right)$ and $3\chi^{(3)}_{(\text{eff})\,R}\, I/\left(4\epsilon_0 n_{\text{TE}}^2 c\right)$ play nonlinear roles analogous to the waveguide's linear absorption coefficient and refractive index, respectively. It is therefore natural to associate the imaginary part of the effective susceptibility appearing in Eq. (2.52) with a nonlinear absorption coefficient, α_2, and the real part with a nonlinear refraction coefficient, n_2, according to the following definitions:

$$\alpha_2 \equiv \frac{3\omega}{2n_{\text{TE}}^2\epsilon_0 c^2}\mathbf{Im}\left\{\chi^{(3)}_{(\text{eff})}\right\} \qquad\qquad n_2 \equiv \frac{3}{4n_{\text{TE}}^2\epsilon_0 c}\mathbf{Re}\left\{\chi^{(3)}_{(\text{eff})}\right\} \tag{2.55}$$

It is understood that these coefficients are specific to the particular interaction described by the $\chi^{(3)}_{(\text{eff})}(-\omega;\omega,\omega,-\omega)$. The notation in Eq. (2.55) is often compacted even further by assigning a complex nonlinear parameter to the TE eigenstate,

$$\gamma_{=}\gamma_R + i\gamma_I \equiv \frac{1}{A_{\text{eff}}}\left(n_2\frac{\omega}{c} + i\frac{\alpha_2}{2}\right) \tag{2.56}$$

Using Eqs. (2.55) and (2.56), Eq. (2.52) becomes

$$\frac{\mathrm{d}u}{\mathrm{d}z} = i\frac{1}{A_{\text{eff}}}\left(\frac{\omega}{c}n_2 + i\frac{\alpha_2}{2}\right)|u|^2 u = i\gamma|u|^2 u \tag{2.57}$$

Written in terms of the waveguide's nonlinear parameter, Eqs. (2.53) become, very simply,

$$\frac{\mathrm{d}m}{\mathrm{d}z} = -\gamma_I m^3 \qquad\qquad \frac{\mathrm{d}\phi}{\mathrm{d}z} = \gamma_R m^2 \tag{2.58}$$

Without loss of generality, we can take the initial phase of the wave to be zero for $z = 0$, in which case Eqs. (2.58) have the following solutions:

$$m(z) = \frac{m(0)}{\sqrt{1 + 2\gamma_I m^2(0) z}} \qquad \phi(z) = \frac{\gamma_R}{2\gamma_I} \ln(1 + 2\gamma_I m^2(0) z) \tag{2.59}$$

where $m(0)$ is the magnitude at $z = 0$. Written in terms of power, these solutions become

$$P(z) = \frac{P_0}{1 + 2\gamma_I P_0 z} \qquad \phi(z) = \frac{\gamma_R}{2\gamma_I} \ln(1 + 2\gamma_I P_0 z) \tag{2.60}$$

where P_0 is the power at $z = 0$. Alternatively, written in terms of the intensity and the nonlinear refraction and absorption coefficients, they become

$$I(z) = \frac{I_0}{1 + \alpha_2 I_0 z} \qquad \phi(z) = \frac{\omega}{c} \left(\frac{n_2}{\alpha_2} \right) \ln(1 + \alpha_2 I_0 z) \tag{2.61}$$

where I_0 represents the average intensity at $z = 0$. Often, the quantity $\alpha_2 I_0 z$ remains much less than unity. In this case, to first order, the z-dependent nonlinear phase (the second equation in Eq. (2.61) reduces to

$$\phi(z) = \frac{\omega}{c} n_2 I_0 z \tag{2.62}$$

For simplicity in the preceding discussion (and for most of the remainder of the dissertation), we have assumed the optical mode is completely contained within the core material of the waveguide. If a significant portion of the optical mode samples the cladding material, then the model used to describe the interaction must account for a weighted average of the overlap of the mode with the nonlinear coefficients associated with the various layers comprising the waveguide. This becomes particularly important for very-small-area semiconductor waveguides, where a significant portion of the mode can "leak" into the cladding layers. When necessary,

the nonlinear effects associated with interactions in the cladding can be included using mode confinement factors (for example, see [19]).

For the semiconductor waveguides presented in this dissertation, the most important physical mechanisms responsible for the nonlinear response are Kerr refraction and two-photon absorption (2PA), and free-carrier absorption (FCA) and dispersion (FCD). Kerr refraction and two-photon absorption are nearly instantaneous, meaning they respond to the applied field on a timescale similar to the period of an optical cycle. On the other hand, free-carrier absorption and dispersion are non-instantaneous nonlinearities which persist throughout the free-carrier lifetime. These effects are discussed in more detail in the following subsection.

2.5.1 Two-photon absorption, free carriers, and the Kerr effect

As the name implies, two-photon absorption occurs when the medium simultaneously absorbs two photons from the applied field to transition to an excited state. The two photons can be absorbed from the same Fourier component of the applied field (degenerate two-photon absorption), which leads to self-induced change of that component's amplitude. Or, if the applied field is not monochromatic, each photon can be absorbed from different Fourier components (non-degenerate two-photon absorption), which leads to cross-modification and interaction between the components. Two-photon absorption in a particular material or waveguide is characterized by $\chi^{(3)}_{(\mathrm{eff})\,I}$, and α_2 is commonly referred to as the two-photon-absorption coefficient.

Two-photon absorption is deleterious to many applications of nonlinear op-

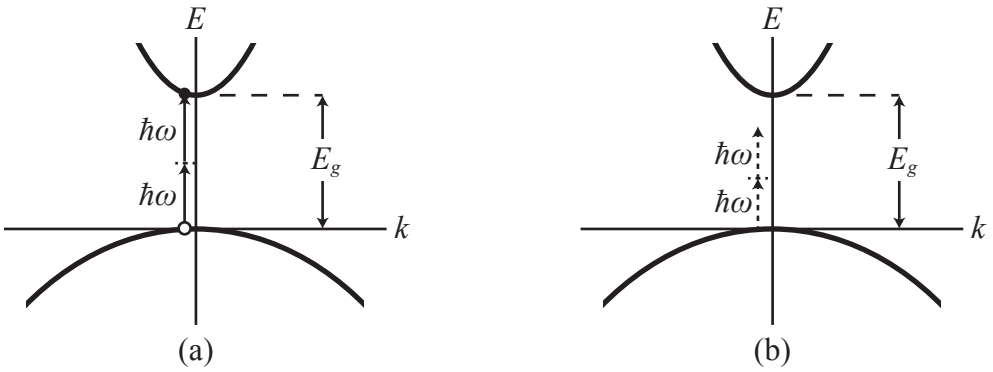

Figure 2.5: Simplified zone-center band-diagrams showing: (a) two-photon absorption is allowed when $2\hbar\omega$ exceeds the bandgap; (b) it is not allowed when the bandgap exceeds $2\hbar\omega$. The case depicted is that of a direct-gap semiconductor like GaAs.

tics [20]; optical loss of any kind depletes the field, which then reduces the nonlinear response. In semiconductors, the strength of two-photon absorption is largely determined by the proximity of the two-photon energy to the bandgap. So, one way to minimize two-photon absorption in a semiconductor waveguide is to engineer the bandgap-energies of the constituent materials to be significantly larger than the two-photon energy.

In the technologically important telecommunications C-band (1530–1565 nm), the two-photon energy exceeds the bandgaps of both GaAs and crystalline silicon (the two-photon energy for 1550-nm light is $2\hbar\omega = 1.60$ eV). Therefore, these materials, which otherwise have very desirable properties for making waveguides, display relatively large two-photon absorption in the spectral range of interest for optical communications [21]. In other words, the ratio γ_I/γ_R is of order unity for waveguides composed of these materials. The case for GaAs, a direct-gap semiconductor, is illustrated by the simplified band-diagram in Fig. 2.5(a), where the two-photon

transition is allowed because the two-photon energy exceeds the bandgap, E_g. On the other hand, when the ratio $\hbar\omega/E_g$ is less than 0.5, the two-photon transition becomes disallowed. This is the case illustrated in Fig. 2.5(b).

When it can occur (i.e., when $\hbar\omega/E_g > 0.5$), two-photon absorption excites an electron to the conduction band and a hole to the valence band, which constitute a pair of free carriers. For passive sub-micron waveguides composed of silicon, the free-carrier lifetime is typically on the order of nanoseconds (but can be as short as hundreds of picoseconds – the rate of recombination in waveguides is enhanced relative to that of the bulk material due to surface recombination). Once created, the free-carrier pair leads to an enhancement of the nonlinear absorption. While they survive, the electron and/or hole can absorb even more photons from the applied field, which is called free-carrier absorption. In addition to the absorptive effect, the phase of the applied field is also modified due to dispersion from the plasma of free carriers, a process called free-carrier refraction. Both these effects scale in proportion to the local density of free carriers, which in turn scales with the local rate of two-photon absorption.

The nonlinear effects caused by a free-carrier plasma are "non-instantaneous" or "delayed" in the sense that they persist long after the impulse-like two-photon absorptions that generate the free carriers. Free-carrier nonlinearities can be very important in semiconductor waveguides, particularly when the applied field is strong enough to cause substantial two-photon absorption (and therefore a large density of free carriers) and when the duration on the applied field is of the same order or longer than the free-carrier lifetime. In this case, free carriers generated by the leading

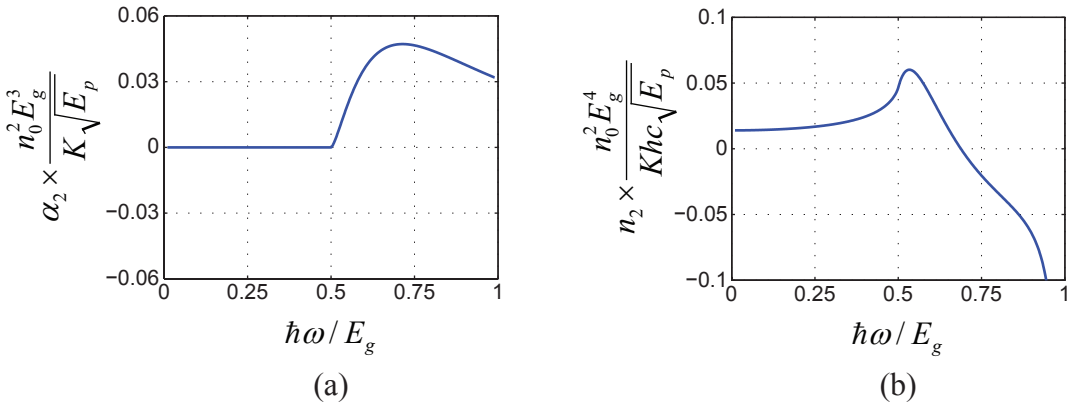

Figure 2.6: (Reproduced from [22]) Calculated dependence of (a) degenerate two-photon absorption and (b) Kerr refraction on the photon energy, based on a two-band model. The material-dependence of the coefficients has been normalized-out. These curves describe the wavelength-dependence of the nonlinear coefficients of a wide class of semiconductor crystals. The normalization factors K and E_p are material independent, while n_0 and E_g represent the frequency-dependent refractive index and the bandgap of the material, respectively.

edge of the pulse-envelope can strongly absorb power from the trailing portions of the envelope, which leads to undesirable patterning of optical pulses [23]. In the context of the four-wave mixing experiments presented later, free-carrier absorption becomes especially important when the applied field is continuous-wave. In this case, the free-carrier population approaches a constant steady state, and free carriers are always present to absorb light from the applied field, which leads to saturation of the achievable four-wave-mixing conversion efficiency.

As an alternative to GaAs or crystalline silicon, $Al_xGa_{1-x}As$ is a promising semiconductor material for nonlinear waveguides because it has a large third-order susceptibility and its bandgap can be adjusted by controlling the mole fraction x in the alloy [24, 25]. The measurements presented later show that for x greater than about 0.18, two-photon absorption in the telecommunications C-band becomes immeasurably small. In and of itself, the reduction of two-photon absorption benefits most nonlinear optical processes. But reduced two-photon absorption also provides the added benefit that fewer free-carriers are generated, and therefore free-carrier effects become less observable as two-photon absorption is decreased.

Kerr refraction (or the optical Kerr effect) happens when the nonlinear polarization effectively changes the refractive index of the medium in a manner directly proportional to the optical intensity. The intensity-dependent refractive index then modifies the phase of the optical field. As with two-photon absorption, Kerr refraction can be a self-induced effect where a single beam modifies the refractive index it is sampling itself, or it can be a cross-modification effect where an intense beam at one wavelength changes the refractive index sampled by a probe at another wave-

length. The strength of nonlinear refraction is characterized by $\chi^{(3)}_{(\mathrm{eff})\,R}$, and n_2 is commonly called the Kerr refraction coefficient. Nonlinear refraction is typically the physical effect exploited for all-optical processing applications, and therefore a large n_2 is usually considered desirable.

Sheik-Bahae, et al., performed an in-depth study of the dispersion of bound electronic nonlinearities in semiconductors [22]. They constructed a quantum mechanical theory that successfully describes the sub-bandgap dependence of n_2 and α_2 on the ratio $\hbar\omega/E_g$ for a wide class of materials (semiconductors and some wide-gap dielectrics). Their theoretical predictions are depicted in Fig. 2.6, which plots the dependence of the (material-normalized) α_2 and n_2 coefficients on the photon energy. Both n_2 and α_2 tend to decrease as the bandgap increases beyond the two-photon-absorption resonance (alternatively, as $\hbar\omega/E_g$ decreases less than 0.5). Thus, for nonlinear optical signal processing, careful selection of the nonlinear medium is important. For many applications, the ideal material exhibits large nonlinear refraction but essentially no nonlinear absorption – an engineering requirement that can be difficult to meet.

2.5.2 Further simplification of the coupled-wave equations

We return now to the scalar effective susceptibilities in Eqs. (2.48a-c). It is often acceptable to simplify things by identifying all of the effective susceptibilities with a single one

$$\chi^{(3)}_{(\mathrm{eff})} \equiv \chi^{(3)}_{\mathrm{xxxx}}(-\omega_p;\omega_p,\omega_p,-\omega_p) \approx \cdots \approx \chi^{(3)}_{\mathrm{xxxx}}(-\omega_i;\omega_p,\omega_p,-\omega_s) \tag{2.63}$$

where the "$\cdots$" represents all the other scalar effective susceptibilities in Eqs. (2.48a-c). This simplification is appropriate when all the frequencies (the ω's appearing in Eq. (2.63)) are sufficiently close that the frequency-dependence of the effective susceptibility can be ignored [13].

Using Eq. (2.63) to identify a single effective nonlinear parameter for the waveguide, Eqs. (2.48a-c) simplify substantially. We arrive at

$$\frac{\mathrm{d}u_p}{\mathrm{d}z} = i\gamma|u_p|^2u_p + i2\gamma|u_s|^2u_p + i2\gamma|u_i|^2u_p + i2\gamma u_p^* u_s u_i \exp(i\Delta\beta z) \tag{2.64a}$$

$$\frac{\mathrm{d}u_s}{\mathrm{d}z} = i\gamma|u_s|^2u_s + i2\gamma|u_p|^2u_s + i2\gamma|u_i|^2u_s + i\gamma u_p^2 u_i^* \exp(-i\Delta\beta z) \tag{2.64b}$$

$$\frac{\mathrm{d}u_i}{\mathrm{d}z} = i\gamma|u_i|^2u_i + i2\gamma|u_p|^2u_i + i2\gamma|u_s|^2u_i + i\gamma u_p^2 u_s^* \exp(-i\Delta\beta z) \tag{2.64c}$$

where $\gamma = (\frac{\omega}{c}n_2 + i\frac{\alpha_2}{2})/A_{\mathrm{eff}}$ is the complex nonlinear parameter discussed in the previous section and ω is the central optical frequency, which is the same as that of the pump wave, $\omega = \omega_p$. Again, $\Delta\beta \equiv \beta(\omega_s)+\beta(\omega_i)-2\beta(\omega_p)$ is the local wave-vector mismatch. Equations (2.64a-c) are identical to those found in several well-cited works on four-wave mixing and parametric amplification in nonlinear optical fibers [13, 14], except they have been generalized to include non-zero nonlinear absorption (i.e., γ is complex).

In contrast to the case of optical fibers, which tend to exhibit negligibly small linear propagation losses, it is usually important to include propagation losses when modeling the behavior of semiconductor waveguides. This is achieved by phenomenologically modeling the waveguide's propagation loss using the loss coefficient

α. Inserting the propagation loss into the equations, we finally obtain

$$\frac{\mathrm{d}u_p}{\mathrm{d}z} = -\frac{\alpha}{2}u_p + i\gamma|u_p|^2u_p + i2\gamma|u_s|^2u_p + i2\gamma|u_i|^2u_p + i2\gamma u_p^* u_s u_i \exp(i\Delta\beta z) \quad (2.65a)$$

$$\frac{\mathrm{d}u_s}{\mathrm{d}z} = -\frac{\alpha}{2}u_s + i\gamma|u_s|^2u_s + i2\gamma|u_p|^2u_s + i2\gamma|u_i|^2u_s + i\gamma u_p^2 u_i^* \exp(-i\Delta\beta z) \quad (2.65b)$$

$$\frac{\mathrm{d}u_i}{\mathrm{d}z} = -\frac{\alpha}{2}u_i + i\gamma|u_i|^2u_i + i2\gamma|u_p|^2u_i + i2\gamma|u_s|^2u_i + i\gamma u_p^2 u_s^* \exp(-i\Delta\beta z) \quad (2.65c)$$

where we have assumed that α is constant over the spectral range of interest. The waveguide's loss coefficient can be measured in various ways, to be discussed later.

It is interesting to inspect the terms in Eqs. (2.65a-c). Consider the differential equation for the pump beam, (2.65a). The first term on the RHS represents the linear absorption of the pump; if the nonlinearity of the waveguide were negligibly small, then the power of the pump beam would simply decay like $P_p(z) = P_p(0)\exp(-\alpha z)$. The second term describes how the pump affects itself through the processes of self-phase and self-amplitude modulation, which are caused by nonlinear refraction and nonlinear absorption, respectively. Likewise, the third and fourth terms represent how the signal and the idler affect the pump through cross-phase and cross-amplitude modulation.[3]

The last term on the RHS of Eq. (2.65a) describes how the pump is affected by the four-wave-mixing interaction. Unlike in the previous terms, the three complex amplitudes multiply in such a way that the phase of this term includes contributions from all three complex amplitudes. And, the four-wave-mixing term includes the exponential factor $\exp(i\Delta\beta z)$. Together, these factors determine how efficiently the four-wave mixing occurs, and the spectral range over which the process remains

[3]Notice that the cross-effects are a factor of two stronger than the self-effects. This is perhaps a surprising consequence of the algebraic steps used to obtain Eqs. (2.31a-c).

phase-matched. The equations for the signal and idler look similar. But, in the last term of both Eq. (2.65b) and (2.65c), the complex amplitude of the pump appears twice and the argument of the complex exponential has the opposite sign compared to Eq. (2.65a). It may not be obvious, but these factors indicate that – depending on the phase relationship among the three complex amplitudes – power can flow out of the pump and into the signal and idler (called parametric amplification), or it can flow from the signal and idler to the pump (known as parametric attenuation) [13]. The conditions required to achieve one case or the other are detailed in Sect. 3.6.

As they stand, Eqs. (2.65a-c) are too complicated to permit tidy analytical solutions. However, for certain initial conditions (i.e., $P_i(z=0) = 0$) and under certain assumptions (i.e., $P_p \gg P_s \gg P_i$ and $\Delta\beta \approx 0$ for all z), approximate analytical solutions are possible. These solutions are given in Appendix A.

2.6 Continuous-wave versus pulsed measurements

The preceding derivation assumes that the field consists only of monochromatic continuous waves, and that the complex field envelopes $A_j(z, \omega_\sigma)$ have no time-dependence. This is an excellent approximation to model experiments where the optical sources are themselves continuous-wave lasers.

There are two chief advantages to using continuous-wave lasers to probe the nonlinearity of a waveguide. First, the coupled-wave equations reduce to a time-independent form, which makes analysis of experimental results particularly simple. It is also easier to measure the optical power of a continuous-wave beam because the

measured average power is the same as the peak power. In contrast, when measuring the power of a short pulse, the experimenter is forced to make assumptions about the shape of the optical pulse to deduce the instantaneous power from the measured average power. As a result, there is typically a higher degree of uncertainty in nonlinear measurements made with short pulses.

That said, to obtain adequate optical power to observe nonlinear behavior clearly, it is often necessary to use short optical pulses. Pulsed lasers such as Q-switched or mode-locked lasers can easily produce peak powers several orders of magnitude larger than those generated by commonplace continuous-wave lasers. The tradeoff is the increased complexity due to the time-dependence of the complex field amplitude. Some of the measurements presented later do employ short optical pulses. To simulate these experiments, computational techniques are used to account for the pulse-shape while solving the nonlinear wave equation.

2.7 Summary

This chapter discusses how the nonlinear polarization is generated, and how it feeds-back to the optical field. Starting from first principles, coupled-wave equations are derived to describe the process of continuous-wave four-wave mixing. The assumptions used to generate the coupled-wave equations are clearly described. These equations are frequently used throughout the remainder of the dissertation to model experimental observations.

The instantaneous effects of two-photon absorption and Kerr refraction are

introduced, as well as the non-instantaneous effects of free-carrier absorption and refraction. These effects are especially important for semiconductor waveguides designed for the telecommunications spectrum.

Chapter 3: Wavelength Conversion in AlGaAs Waveguides

3.1 Overview

The efficient management of wavelength-division-multiplexed (WDM) optical networks relies on a key piece of technology: the wavelength converter [26]. This device takes a data-bearing signal at one carrier wavelength and replicates the same signal to a new carrier wavelength. Illustrated schematically in Fig. 3.1, wavelength conversion is useful for routing and switching to maintain spectral efficiency in WDM networks. The conventional way to wavelength-convert a signal is to detect the original optical signal electrically, and then use the electrical domain signal to modulate

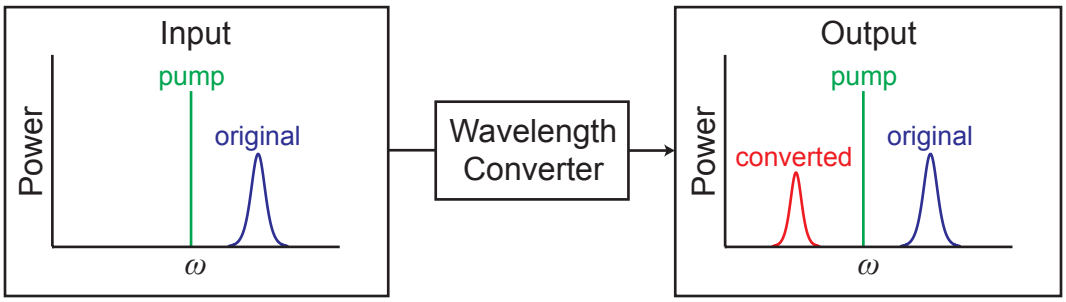

Figure 3.1: Conversion of a generic signal from its original frequency (blue) to a lower frequency (red). The scheme shown here uses the interaction between the pump and the incident signal to generate the converted signal.

another laser operating at a different wavelength.

Using a nonlinear waveguide for wavelength conversion – achieved by exploiting the waveguide's ultrafast nonlinearities – offers an all-optical alternative to the conventional optical-electrical-optical wavelength converter. This scheme could provide several key performance benefits compared to the conventional converter, including reduced latency, increased bandwidth,[1] transparency to the input data format, simplicity of implementation, and decreased wall-plug power demand [26, 27]. These benefits will become more important as data-rates continue to rise and per-bit power-consumption requirements become more strict.

The idea to exploit nonlinear waveguides for wavelength conversion is not new. Four-wave mixing in standard optical fiber has long been used to achieve wavelength conversion in the telecommunications spectrum [13, 14]. But, standard silica-glass fibers exhibit a relatively weak optical nonlinearity. And, even for specially designed highly nonlinear fibers such as bismuth-oxide photonic crystal fibers (PCFs), at least several meters of fiber are required to achieve efficient wavelength conversion (and for longer spans, pump-induced stimulated Brillouin scattering (SBS) can degrade the converted signal quality) [28,29]. The same is true for highly nonlinear chalcogenide-glass fibers [30]. Thus, fiber-based wavelength converters do not readily integrate with ever-shrinking, chip-based photonic systems.

On the other hand, low-loss, sub-micron semiconductor waveguides could enable all-optical wavelength conversion in a compact, integrated platform. And,

[1] In this context, bandwidth refers both to the spectral distance over which the original signal can be converted (the conversion bandwidth) *and* to the maximum bit-rate the device can convert (the signal bandwidth).

while many nonlinear-waveguide-on-chip systems have been proposed, advances in this field have been mainly dominated by the silicon-on-insulator (SOI) platform. SOI is the obvious choice for on-chip optical processing because the electronics industry has, over the course of decades, driven the development of sophisticated and low-cost fabrication techniques for silicon devices.

Silicon possesses a large Kerr nonlinearity (≈ 200 times that of silica glass [21, 31, 32]). And, the maturity of complementary-metal-oxide-semiconductor (CMOS) fabrication techniques means it is relatively easy to make high-quality, low-linear-loss, dispersion-engineered SOI waveguides (for example, see [33]). In fact, were it not for two fundamental flaws, which are both related to the band structure of crystalline silicon, it would be nearly ideal for chip-based all-optical processing: First, because crystalline silicon possesses a relatively narrow bandgap, it unavoidably exhibits two-photon absorption in the telecom spectrum. Second, because it is an indirect-gap semiconductor, it is difficult to make an integrated optical source using silicon [11, 34]. Indeed, despite the two-photon absorption (and subsequent free-carrier absorption) intrinsic to the material, several groups have managed to demonstrate efficient and broad-band wavelength conversion, and even parametric gain, via four-wave mixing in dispersion-engineered silicon nanowire waveguides [35–37].

The search for the ideal nonlinear-waveguide material has recently shifted to other silicon-based materials. These candidates include: silicon nitride (SiN), first proposed for nonlinear optics in [38]; high-index doped silica glass (Hydex®), proposed in [39]; and hydrogenated amorphous silicon (a-Si:H), proposed in [40]. All of these are CMOS-compatible. SiN exhibits fairly large Kerr refraction ($n_2 \approx 10$

times that of silica glass) and virtually no nonlinear absorption in the telecom spectrum [11]. And, using chemical vapor deposition techniques, it has recently become possible to fabricate SiN nanowire waveguides with ultra-low propagation loss, on the order of dB/m rather than dB/cm [41]. Similarly, though the Kerr nonlinearity of Hydex® is relatively small ($n_2 \approx 5$ times that of silica glass [42]), sub-micron waveguides composed of Hydex® can also exhibit dB/m propagation loss [43]. Finally, though the role of nonlinear absorption in a-Si:H is still a matter of debate, it has been reported to have a very large Kerr nonlinearity ($n_2 \approx 1000$ times that of silica glass [44]). And, in a very recent report, the linear loss observed in an a-Si:H nanowire rivaled those observed in the best SOI nanowires [45]. All of these alternative silicon materials are very promising. Very efficient and broad-band four-wave mixing, and even parametric gain, have been demonstrated in dispersion-engineered waveguides composed of each of these material systems (see [46, 47] for SiN, [48] for Hydex®, and [49, 50] for a-Si:H).

Another material system receiving a lot of attention for telecom nonlinear optics (even though it's not a semiconductor) is chalcogenide glass (ChG). This is a generic name for glass whose major components include a group-6a element (the chalcogens) covalently bonded to a network-forming element like As, Ge, Sb, Ga, Si or P. CMOS-compatible fabrication techniques have been developed to make low-loss (several dB/cm), sub-micron rib and ridge waveguides mounted on silicon substrates [51, 52]. And, chalcogenide glass can be engineered to have very desirable nonlinear properties – several presented in [53] exhibit Kerr nonlinearities significantly larger than that of silicon (with n_2 values $\approx$ 500 to 1000 times that of silica glass) *and*

negligibly small nonlinear absorption. Even when ChG does exhibit two-photon absorption, it does not exhibit subsequent free carrier effects (whereas silicon does). Very efficient, broad-band four-wave mixing (using a CW pump, [54]) and parametric amplification with net gain (using optical pulses, [55]) have been demonstrated in dispersion-engineered, chip-based ChG waveguides. Chalcogenide glasses – like the alternative silicon-based materials discussed above – remain very promising for chip-based nonlinear optics and wavelength conversion.

This chapter investigates AlGaAs waveguides for wavelength conversion via continuous-wave four-wave mixing. In this context, the "continuous-wave" refers to using a strong monochromatic pump light, which is always on. Therefore, there is no need to achieve temporal alignment between the incident signal and the pump, and any arbitrarily formatted signal can be converted. The drawback to this scheme is that it is difficult to achieve efficient four-wave mixing using a continuous-wave pump. The high average pump-power required to amplify the idler wave (the converted signal) often leads to irreversible damage of the waveguide.

AlGaAs was actually one of the first materials proposed for chip-based nonlinear optics in the telecom spectrum [25]. This is because it demonstrates broadband transparency throughout the telecommunication band. And, as discussed in Sect. 2.5.1, $Al_xGa_{1-x}As$ possesses a large nonlinearity and its bandgap can be adjusted by controlling the mole fraction x in the alloy. It is therefore possible to produce AlGaAs waveguides that exhibit the combination of high nonlinearity and no nonlinear absorption by using an alloy with the optimal mole fraction of aluminum. For comparison to the other materials listed above, the AlGaAs waveguides presented in

Table 3.1: Properties of competing nonlinear waveguide systems at 1550 nm

System	α (dB/cm)	A_{eff} (μm^2)	γ_R (W $\cdot$ m)$^{-1}$	γ_I (W $\cdot$ m)$^{-1}$
SMF-28 fiber [56]	5×10^{-7}	80	1.1×10^{-3}	≈ 0
Bismuth oxide PCF [28]	1.9	3.17	0.58	≈ 0
As_2Se_3 glass fiber [30]	0.01	37	1.2	0.04
Silicon waveguide [37]	0.6	0.28	58	8.9
Si_3N_4 waveguide [11]	0.5 Note 1	– Note 2	1.2	≈ 0
Hydex® waveguide [42]	< 0.06 Note 3	2.0	0.22	≈ 0
a-Si:H waveguide [44]	4.5 Note 4	0.07	1200	18
As_2S_3 waveguide [55]	0.5	1.2	10	≈ 0
AlGaAs waveguide Note 5	1.11	0.45	81	≈ 0

In this table, the real and imaginary parts of the nonlinear parameter are defined as

$$\gamma_R \equiv \frac{\omega}{cA_{\text{eff}}} n_2 \qquad\qquad \gamma_I \equiv \frac{\alpha_2}{2A_{\text{eff}}}$$

Note 1: A sub-micron silicon nitride waveguide with 9 dB/m loss was demonstrated in [41].
Note 2: A_{eff} not given in [11].
Note 3: A sub-micron Hydex® waveguide with 6 dB/m loss was demonstrated in [43].
Note 4: A sub-micron a-Si:H waveguide with ≈ 1 dB/cm loss was demonstrated in [45].
Note 5: This waveguide was used for the four-wave-mixing results shown in Fig. 3.15.

this chapter exhibit Kerr refraction coefficients ranging from 500 to 1000 times that of silica glass. The reported nonlinear parameters of various competing nonlinear waveguide systems (including an AlGaAs waveguide studied for this dissertation) are summarized in Table 3.1.

AlGaAs waveguides have been studied extensively for four-wave mixing and other third-order nonlinear processes [57–61]. But, while it is well known that suppression of nonlinear absorption can be achieved by tailoring the bandgap, the wavelength conversion efficiency and conversion bandwidth in this material system have lagged behind those of competing waveguide platforms – even those that do suffer from nonlinear absorption.

The performance-lag of AlGaAs waveguides stems from the fact that they are usually fabricated in smaller cleanrooms which do not maintain photolithography tools competitive with those found in commercial CMOS foundries (in terms of achievable feature size and line-edge roughness). Until now [62], it has not been possible to fabricate AlGaAs waveguides with the right combination of cross-sectional dimensions and linear loss to achieve good wavelength-conversion performance. These variables – the cross-sectional dimensions and the linear loss – are coupled: As it turns out, to achieve phase-matching of the four-wave-mixing interaction over a broad spectral range requires a very narrow waveguide (less than 1 μm wide). At the same time, the (linear) propagation loss of AlGaAs ridge waveguides is typically dominated by scattering from sidewall roughness, and this becomes exponentially worse as the width of the waveguide-ridge decreases. So, to make a low-loss AlGaAs waveguide for efficient and broadband wavelength conversion,

the engineering requirements push the fabrication limits in two ways. First, the minimum possible photolithographic feature size is required to achieve the desired dispersion. Second, the minimum possible line-edge roughness is required to maintain acceptable linear loss. The AlGaAs waveguides presented here were designed, grown and fabricated by a team at the Laboratory for Physical Sciences consisting of Paveen Apiratikul, Gyorgy Porkolab, John Hyrniewicz and Christopher J. K. Richardson. They devised a fabrication process to produce AlGaAs waveguides which are simultaneously narrow *and* low-loss.

3.2 Device fabrication

The waveguide epitaxial structure is grown using solid-source molecular beam epitaxy (MBE) on top of a n-doped GaAs substrate. The AlGaAs epilayer heterostructure consists of three layers: lower cladding, core, upper-cladding. Many geometries were tested to determine the dependence of the dispersion on the cross-sectional dimensions. For the waveguides presented here, the lower cladding layer is typically about 2 microns thick, the guiding core layer is either 0.5 μm or 0.8 μm, and the upper cladding is typically about 0.2 μm thick.

The refractive index and bandgap of each layer is determined by the mole fraction x in the alloy (an empirical model that relates x to the refractive index and the bandgap is presented in [18]). Typical values for the percent-aluminum in the high-index core-layer range from $x = 0.14$ to $x = 0.24$. These alloy compositions lead to core-bandgaps ranging from 1.60 eV to 1.8 eV, measured using photoluminescence

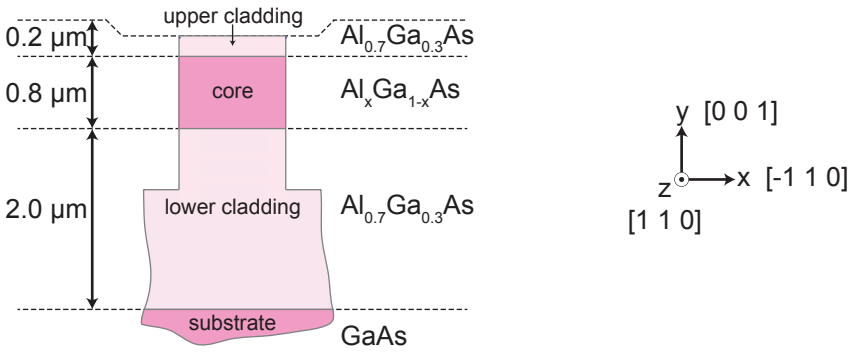

Figure 3.2: The geometry and composition of a typical AlGaAs waveguide. The labels on the coordinate axes are Miller indices indicating the orientation of the crystal axes relative to the coordinate system of the waveguide.

(PL) spectroscopy. The low-index cladding layers have $x = 0.70$. The epilayer structure of a typical fabricated waveguide is shown in Fig. 3.2, which also shows the orientation of the crystal's axes with respect to the coordinate system used to describe the waveguide. (Many of the AlGaAs waveguides include curved segments where the crystalline plane normal to [0 0 1] continuously rotates in the xz-plane of the waveguide's coordinate system. Figure 3.2 shows the orientation of the crystal axes in the straight segments of the waveguides. The facets are always cleaved along the crystalline plane normal to [1 1 0] and straight segments of the waveguides always run along the [1 1 0] direction.)

The waveguides are defined using projection lithography with positive i-line photoresist ("i-line" refers to a particular line in the emission spectrum of a mercury vapor lamp, meaning the photoresist is sensitive to exposure at 365 nm). On the mask, the waveguide widths range from 0.4 to 2 microns and the lengths range from 0.5 cm to 2.5 cm. The width of each waveguide is flared at both ends (to about 2.2

μm) to improve the fiber-to-waveguide coupling. The mask is projected onto the photoresist by a 5$\times$ i-line stepper.

For some of the waveguides, after development, the photoresist is smoothed using a nitrogen plasma-assisted reflow (detailed in [62]). This process raises the temperature of the photoresist above its glass transition temperature, which causes it to "reflow." The reflow smooths the developed photoresist, which translates directly to smoother waveguide-sidewalls after the etch. Unfortunately, the reflow process also causes the developed photoresist to expand, which increases the minimum achievable feature size to about 0.65 μm (0.4 μm prior to the reflow). The photoresist (either as-developed or reflowed, as the case may be) then acts as the etch-mask in an inductively coupled plasma (ICP) etch, using a mixture of BCl_3 and N_2 gas. Figure 3.3 shows a side-by-side comparison of a waveguide fabricated without using the reflow process and one fabricated with the reflow process.

The waveguides are cleaved to length and coated with a conformal layer of silicon nitride (SiN). This layer coats the entire structure, including the sidewalls and the facets. It acts as an encapsulant and as a single-layer anti-reflection (AR) coating. The measured reflectivity of a typical AR-coated waveguide-facet is less that 1×10^{-2}. As detailed later, the conformal SiN does alter the dispersion of the waveguide. In an attempt to achieve zero group-velocity dispersion in some of the narrowest waveguides, the SiN layer is removed from the sidewalls. This is achieved by first protecting the facets with photoresist, removing the naked SiN using an oxygen plasma, and then washing the remaining photoresist from the facets. This process maintains the SiN layer on the facets to act as an anti-reflection coating,

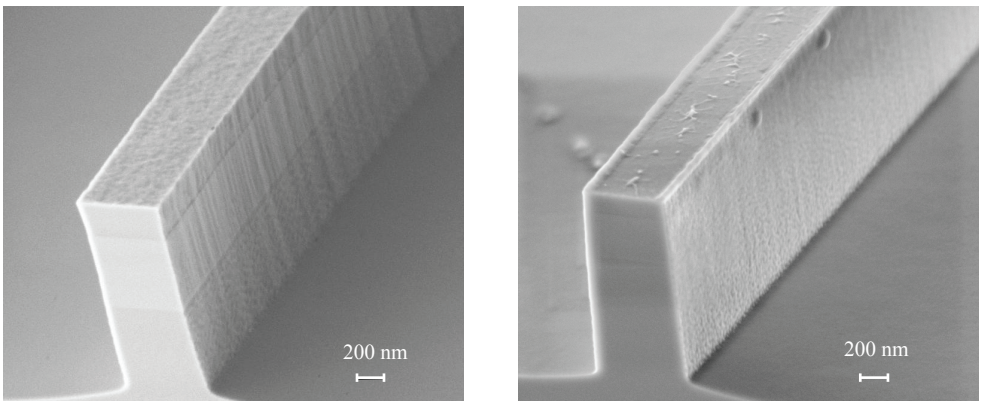

(a) (b)

Figure 3.3: Scanning electron micrographs of etched waveguides patterned using (a) the as-developed photoresist and (b) the re-flowed photoresist. Reduction of the deep-etched sidewall roughness is evident in the waveguide fabricated using the photoresist-reflow process.

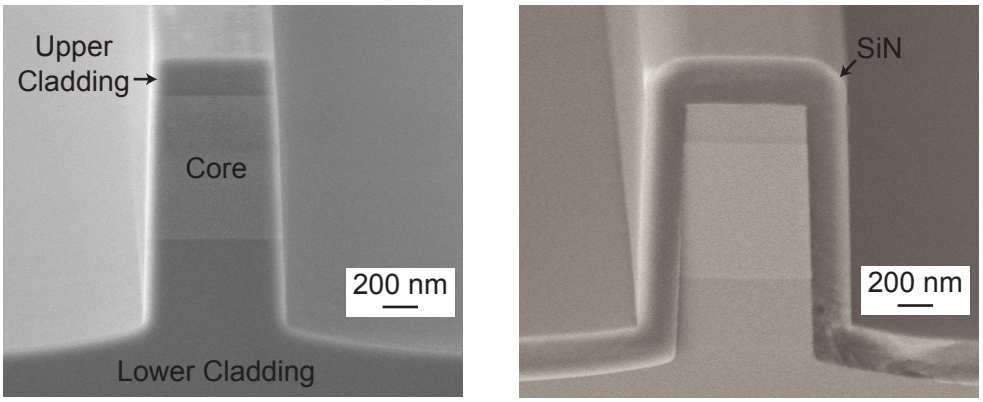

(a) (b)

Figure 3.4: (a) Scanning electron micrograph of a 0.75-μm-wide AlGaAs waveguide, fabricated using the reflow process. (b) The same waveguide, after coating with silicon nitride.

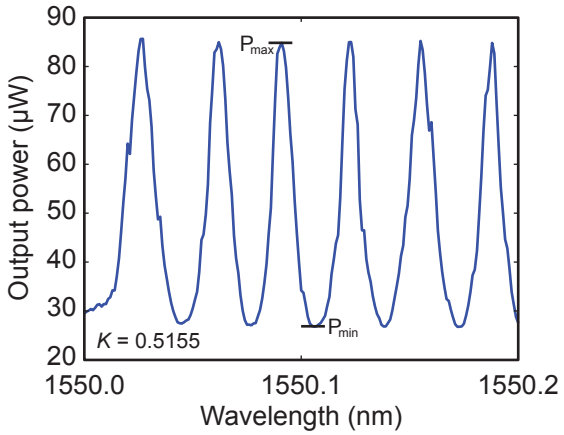

Figure 3.5: An example of the measured wavelength-dependent transmission of an AlGaAs waveguide (prior to deposition of the anti-reflection coating). The contrast of the fringes is used to calculate the propagation loss of the waveguide using Eq. (3.3).

but removes it everywhere else. Scanning electron micrographs of a 0.75-μm-wide AlGaAs waveguide are shown in Fig. 3.4, before and after the structure has been coated with SiN.

3.3 Evaluating the linear properties of AlGaAs waveguides

The linear properties of a waveguide – the linear propagation loss, the effective mode area, the length – must be known before accurate measurements of the nonlinear properties can be made. The method used to compute the mode area has already been discussed in Sect. 2.4.1. The following section details the methods used to measure the linear propagation loss and to estimate the group-velocity dispersion.

3.3.1 Propagation loss measurements

The linear propagation loss of the AlGaAs waveguides is determined using the Fabry-Pérot technique, first described in [63]. The technique relies on measuring the finesse of the Fabry-Pérot cavity that forms when the waveguide facets are cleaved (prior to anti-reflection coating). This technique provides a way to measure the propagation loss independent of the coupling losses.

Light from a tunable continuous-wave laser is coupled into the waveguide and the transmitted power is measured while the wavelength is swept. The state of polarization of the light is aligned with the TE or TM eigenstate. The relative transmission of the cavity is periodic as a function of the wavelength, given by [63]

$$T(\phi) = \frac{(1-R)^2 \exp(\alpha L)}{(1-\tilde{R})^2 + 4\tilde{R}\sin^2\phi} \tag{3.1}$$

where $\phi \equiv 2\pi n_{\text{eff}} L/\lambda_0$, n_{eff} is the mode's effective refractive index, α is the propagation loss coefficient, λ_0 is the central wavelength, R is the facet reflectivity, and $\tilde{R}$ is the normalized facet reflectivity given by $\tilde{R} = R\exp(-\alpha L)$. The contrast, K, of the oscillations is given by

$$K \equiv \frac{T_{\max} - T_{\min}}{T_{\max} + T_{\min}} = \frac{2\tilde{R}}{1+\tilde{R}^2} \tag{3.2}$$

and therefore the loss coefficient can be calculated from the contrast via

$$\ln[(1-\sqrt{1-K^2})/K] = \ln R - \alpha L \tag{3.3}$$

where it is assumed that $R = 0.3$ to account for the Fresnel reflectivity between air and the AlGaAs alloy used in the waveguide's core.

3.3.2 Estimating the dispersion

The dispersion of the waveguide is one important parameter that determines whether phase-matching of a nonlinear interaction can be achieved. As discussed in Sec. 2.4.1, the modesolver is used to calculate the frequency-dependent effective propagation constant, $\beta(\omega)$, of an AlGaAs waveguide. This provides a computational method to estimate the waveguide's dispersion.

In many cases, the frequency-dependence of β can be accurately modeled by expanding β to second order in the vicinity of some central frequency ω_0,

$$\beta(\omega) \approx \beta(\omega_0) + (\omega - \omega_0) \left.\frac{\mathrm{d}\beta}{\mathrm{d}\omega}\right|_{\omega_0} + \frac{(\omega - \omega_0)^2}{2!} \left.\frac{\mathrm{d}^2\beta}{\mathrm{d}\omega^2}\right|_{\omega_0} \tag{3.4}$$

The curvature of $\beta(\omega)$ in ω is referred to as the group-velocity dispersion, usually represented by β_2 but sometimes as "GVD." (Many authors use β_2 to represent the two-photon-absorption coefficient. In this dissertation, β_2 is reserved for the group-velocity dispersion while α_2 is reserved for two-photon absorption.) The group-velocity dispersion is given by

$$\beta_2(\omega_0) \equiv \left.\frac{\mathrm{d}^2\beta}{\mathrm{d}\omega^2}\right|_{\omega_0} \tag{3.5}$$

which, for obvious reasons, is also referred to as the second-order-dispersion. Historically, $\beta_2 > 0$ is referred to as "normal" dispersion (because the majority of bulk materials exhibit normal dispersion) while $\beta_2 < 0$ is referred to as "anomalous" dispersion.

In the context of continuous-wave four-wave mixing, recall that the coupled-wave equations for four-wave mixing, Eqs. (2.65), depend on the group-velocity

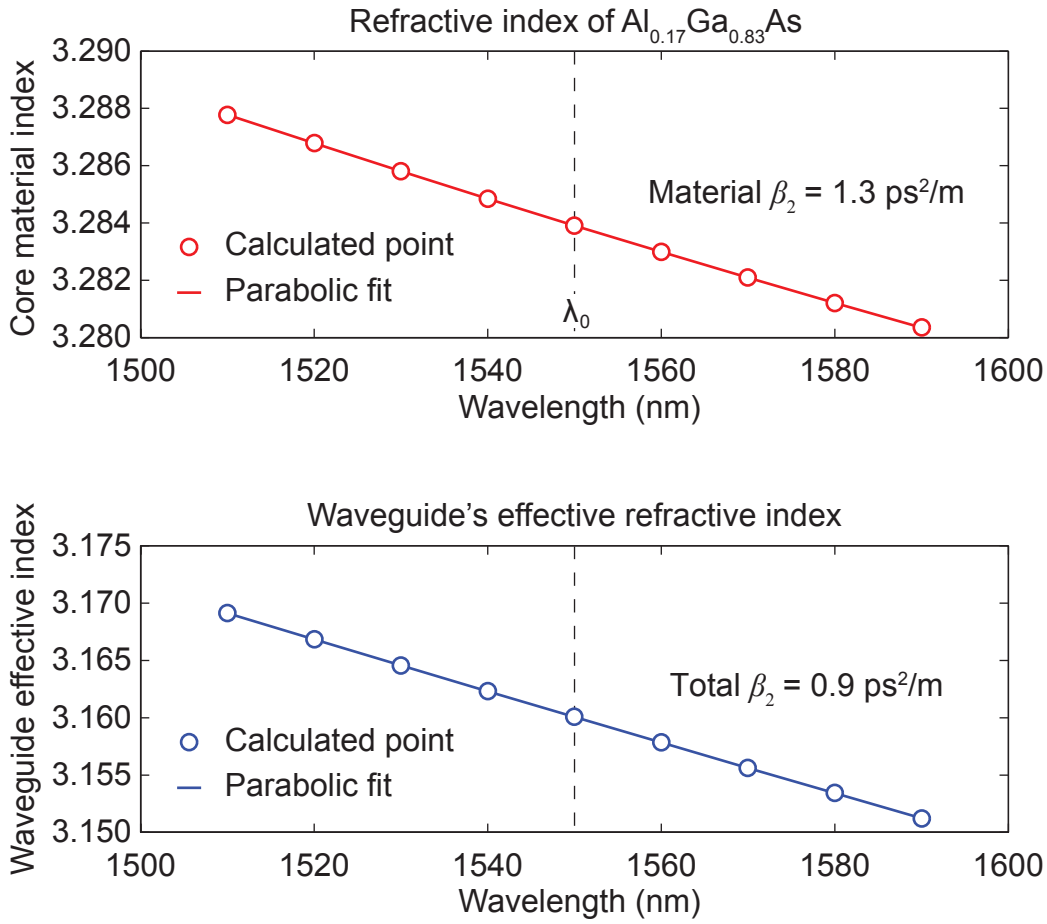

Figure 3.6: (Top) The red circles show the wavelength-dependent material refractive index of the core-layer material used in the waveguide of Fig. 2.3, which is $Al_{0.17}Ga_{0.83}As$. These points were calculated using the empirical model of [18]. The red line is a best-fit 2nd-degree polynomial, used to estimate the material dispersion at $\lambda_0 = 1550$ nm. (Bottom) The blue circles show the wavelength-dependent effective refractive index of the waveguide's TE eigenstate, calculated using the modesolver. The blue line is a best-fit 2nd-degree polynomial, used to estimate the waveguide's total dispersion. The modal dispersion of this structure reduces the total dispersion relative to the material dispersion.

mismatch parameter $\Delta\beta$, where $\Delta\beta \equiv \beta(\omega_s) + \beta(\omega_i) - 2\beta(\omega_p)$. Expanding $\beta(\omega_s)$ and $\beta(\omega_i)$ to second order about ω_p, we have

$$\beta(\omega_s) + \beta(\omega_i) - 2\beta(\omega_p) \approx (\Delta\omega)^2 \times \beta_2(\omega_p) \tag{3.6}$$

where $\Delta\omega$ is the frequency separation between the pump and signal (or idler and pump). Note that even if higher orders of dispersion are considered in the expansions of $\beta(\omega_s)$ and $\beta(\omega_i)$, the odd orders (i.e., $\mathrm{d}^n\beta/\mathrm{d}\omega^n$ for n an odd positive integer) will always cancel when evaluating the sum on the LHS of Eq. (3.6). Typically only the second-order dispersion needs to be considered when evaluating the group-velocity mismatch parameter over a modest range of $\Delta\omega$.

The total dispersion of a waveguide includes contributions from the geometry-dependent "waveguide" dispersion (a.k.a. "modal" dispersion) and the material-dependent "material" dispersion. In the modesolving calculations, the waveguide dispersion is accounted for by properly defining the geometry of the structure while the material dispersion is inserted by using Gehrsitz's model [18] to account for the frequency-dependent refractive index of each layer in the geometry.

For example, the dispersion characteristics of the waveguide pictured in Fig. 2.3 are depicted in Fig. 3.6. The core-layer material in this waveguide is $Al_{0.17}Ga_{0.83}As$. The top axes in Fig. 3.6 shows the dispersion of bulk $Al_{0.17}Ga_{0.83}As$, where the red circles are calculated using Gehrsitz's empirical model [18]. The red line is a best-fit 2nd-degree polynomial. The bottom axes in Fig. 3.6 shows the total dispersion of the waveguide. The blue circles represent the effective refractive index of the TE eigenstate as a function of wavelength, calculated using the modesolver. The

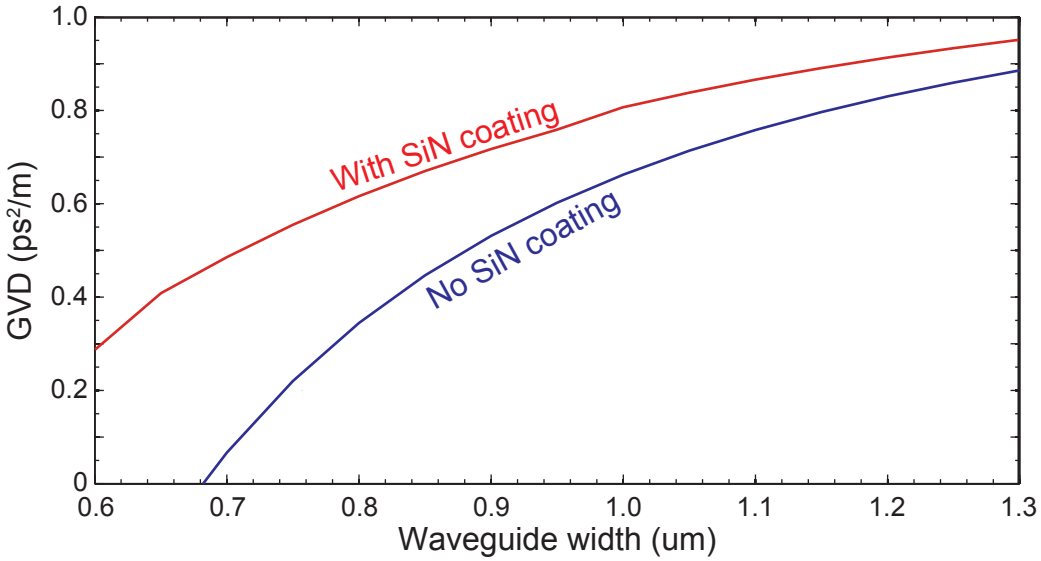

Figure 3.7: The calculated group-velocity dispersion of the TE eigenstate of an AlGaAs waveguide as a function of the waveguide-width. The red curve represents the case when the waveguide is coated with SiN, the blue represents the case without SiN. These calculations were performed assuming the same vertical profile shown in Fig. 2.3.

blue line is the best-fit 2nd-degree polynomial. In each case, the curvature of the dispersion is extracted from the fit parameters, and the group-velocity dispersion is calculated using

$$\beta_2 = \frac{\lambda_0^3}{2\pi c^2} \frac{\mathrm{d}^2 n}{\mathrm{d}\lambda^2}\Big|_{\lambda_0} \tag{3.7}$$

where n is the wavelength-dependent refractive index. For this waveguide, the material GVD of the core-layer material is 1.3 ps^2/m, while the total GVD is 0.9 ps^2/m for $\lambda_0 = 1550$ nm. Therefore, the modal dispersion of this structure reduces the total dispersion relative to the material dispersion.

As highlighted in this example, for this type of AlGaAs ridge waveguide, the modal contribution to the total dispersion has the opposite sign compared to the material dispersion of the core. And, the magnitude of the modal contribution grows as the width of the ridge decreases [64, 65]. This allows the net dispersion to be adjusted by engineering the waveguide-geometry. For a structure similar to that pictured in Fig. 2.3, the calculated group-velocity dispersion of the fundamental TE eigenstate (at 1550 nm) approaches zero and then becomes anomalous as the width of the waveguide decreases less than about 550 nm. Similar calculations show that the TM eigenstate never achieves zero GVD, regardless how narrow the waveguide is made. For this reason, all the following experiments were arranged to test four-wave mixing by exclusively exciting the TE eigenstate. The calculated dependence of the GVD of the TE eigenstate on the width of the waveguide is shown in Fig. 3.7. Calculations were performed with (represented by the red line) and without (the blue line) the SiN layer included in the structure. When included, the SiN layer is

assumed to be 200 nm thick, with a refractive index of 1.86. Removal of the SiN encapsulant plays an important role in the near-zero-GVD regime.

3.4 Nonlinear transmission of AlGaAs waveguides

To illustrate the impact of tailoring the core-bandgap on two-photon absorption, this section compares the power-dependent transmission of picosecond optical pulses through two different waveguides. The MBE growth of these waveguides – referred to as Waveguide I and Waveguide II – was controlled to provide different bandgap energies for the core layers. In the core of Waveguide I, the mole fraction of aluminum is approximately $x = 0.14$, which corresponds to a bandgap of 1.60 eV. For Waveguide II, the core-mole-fraction is $x = 0.18$, for a bandgap of 1.66 eV. These mole fractions are estimates based on x-ray diffraction spectroscopy of the core layer, conducted *in situ* during the MBE growth. The corresponding bandgap-energies are measured using low-temperature photoluminescence spec-

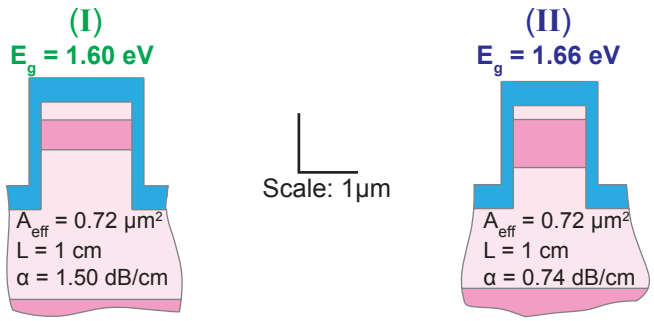

Figure 3.8: Waveguides I (left) and II (right), with relevant properties of the fundamental TE eigenstate. The energies are the measured bandgaps of the core layers.

troscopy. Based on the measured bandgaps, two-photon absorption is expected to be significant for $\lambda \leq 1550$ nm in Waveguide I. For Waveguide II, it is expected to be significant for $\lambda \leq 1494$ nm.

The cross-sections of Waveguides I and II are depicted in Fig. 3.8. While the waveguide-cores have slightly different aspect ratios, the calculated effective mode area for the fundamental TE eigenstate at 1550 nm is the same for both waveguides, $A_{\text{eff}} = 0.72\ \mu\text{m}^2$. The 1550-nm propagation loss of the TE eigenstate, measured using the Fabry-Pérot technique described in Sect. 3.3.1, is 1.50 dB/cm for Waveguide I and 0.74 dB/cm for Waveguide II. Both waveguides are cleaved to a length of 1 cm and covered with a single-layer SiN anti-reflection coating.

To measure the power-dependent transmission, pulses from a mode-locked fiber laser with a repetition rate of 10 MHz (an inter-pulse interval of 100 ns) are launched into the waveguide using a polarization-maintaining (PM), lensed optical fiber (purchased from Oz Optics, Ltd.). An identical lensed fiber collects the light

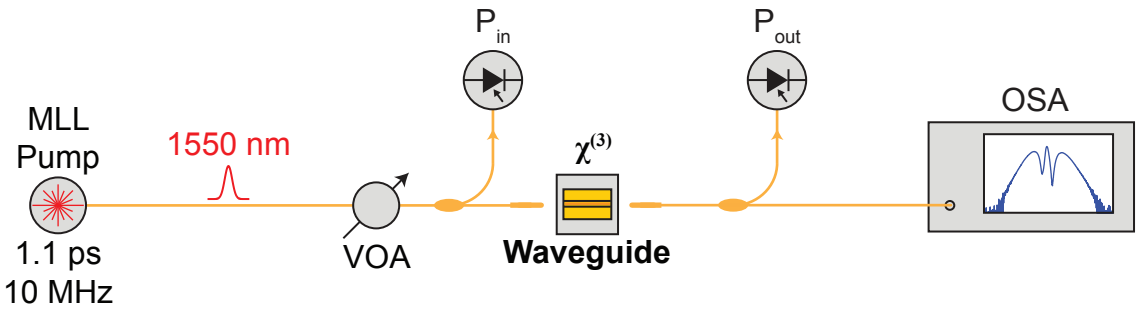

Figure 3.9: The experimental setup used to measure the power-dependent transmission and spectral broadening of Waveguides I and II. MLL: mode-locked laser; VOA: variable optical attenuator; OSA: optical spectrum analyzer.

at the output of the waveguide. Each lensed fiber consists of a standard PM optical fiber, where the fiber-tip is shaped into a conical lens using laser ablation, and is then anti-reflection coated. Recall that the waveguide facets are flared to a width of 2.2 μm to facilitate fiber-to-waveguide coupling. The lensed fiber is designed to produce a focused $1/e^2$ spot-diameter of 2.5 μm and modesolving calculations show that the theoretical coupling loss between the focused spot and the mode of the flared structure should be approximately 2 dB. In practice, it is typical to achieve between 2.5 and 4 dB of coupling loss at each facet. (Without the flare at the facet, modesolving calculations show that the per-facet coupling loss would be several dB larger, depending on the width of the waveguide.)

Prior to the experiment, the slow axis of the input-side PM lensed fiber is aligned such that the launched light only excites the TE eigenstate of the waveguide. A 5% tap-coupler is used to monitor the power and spectrum before the waveguide. The inserted power is swept using a variable optical attenuator and the transmitted spectrum and power are measured as a function of the input power. The experimental setup is depicted in Fig. 3.9 and Fig. 3.10 shows the inverse transmission ($P^{\text{in}}_{\text{avg}}/P^{\text{out}}_{\text{avg}}$) of each waveguide as a function of the inserted intensity. Figure 3.11 shows the power-dependent spectral broadening generated by each waveguide.

The pulses emitted by the laser have a central wavelength of 1550 nm. The power-envelope of each pulse is approximately hyperbolic-secant-squared in shape, $P(t) = P_0\text{sech}^2(t/t_0)$, with a measured pulse-width of $t_0 = 0.63$ ps (which corresponds to a full-width at half-maximum of 1.1 ps). Using the process described in Sect. 3.3.2, the net GVD of Waveguide I is estimated to be 1.05 ± 0.05 ps^2/m while

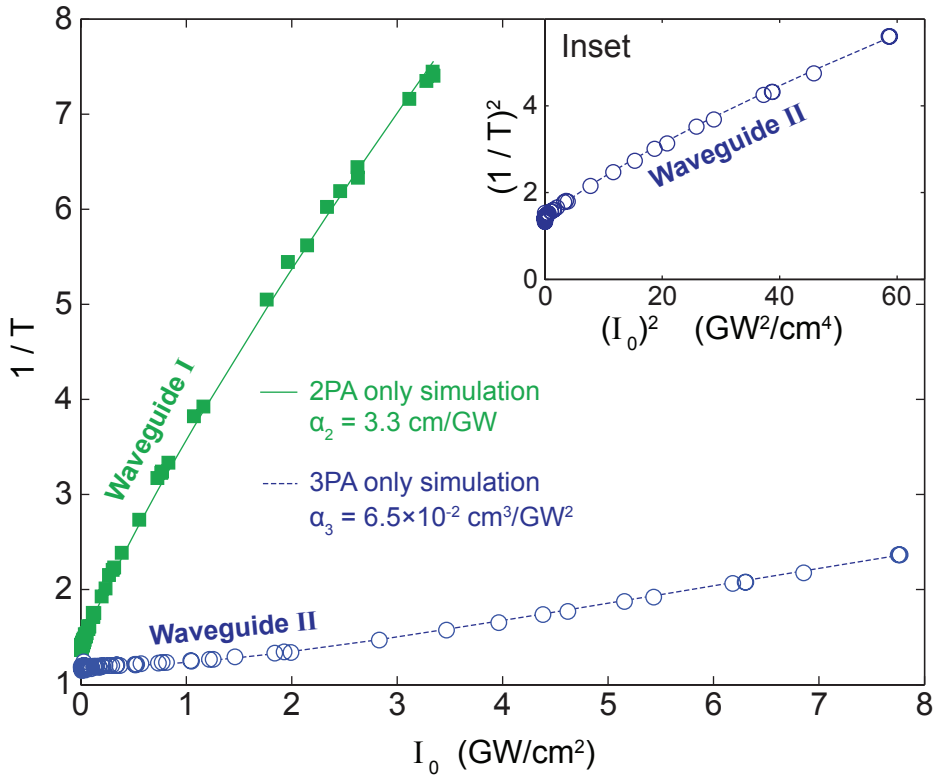

Figure 3.10: Measured and simulated inverse transmission vs. peak input intensity for Waveguides I and II. Inset: Inverse transmission squared vs. the square of the peak input intensity for Waveguide II.

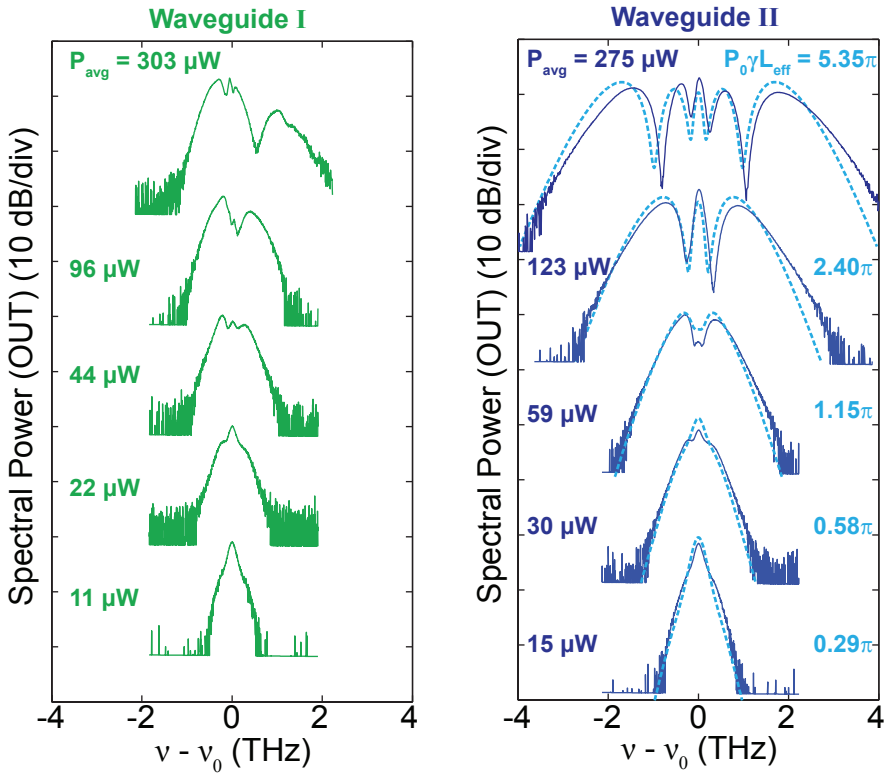

Figure 3.11: Measured output spectra (solid lines) as a function of average input power for Waveguides I and II. The spectra are vertically offset for clarity. Labels on the left of each column indicate the average power launched into the waveguide. The dashed cyan lines are simulations of the spectra for Waveguide II, and cyan labels on the right indicate the simulated peak phase shift.

for Waveguide II it is 0.9 ± 0.05 ps^2/m. For the 0.63-ps pulse-duration used in this experiment, the dispersion-length of these waveguides, L_D, is much greater than the physical length, where L_D is given by [66]

$$L_D = \frac{t_0^2}{|\beta_2|} \tag{3.8}$$

We can therefore neglect dispersion-induced pulse-broadening when considering the nonlinear transmission of the waveguides.

To simulate the experiments of Fig. 3.10, the propagation of the pulse-envelope through distance z in the waveguide can be modeled according to [24, 25, 67]

$$\frac{\partial I(z,t)}{\partial z} = -\alpha I(z,t) - \alpha_2 I^2(z,t) - \Gamma\alpha_3 I^3(z,t) \tag{3.9}$$

where $I(z,t)$ is the mode-averaged intensity defined as $I(z,t) \equiv P(z,t)/A_{\text{eff}}$, α is the linear loss, and α_2 and α_3 represent two- and three-photon absorption, respectively. The factor Γ, given by $\Gamma \equiv (A_{\text{eff}}/A_{5,\text{eff}})^2$, is a normalization constant included to account for the fact that three-photon absorption is a fifth-order nonlinearity. Here, the fifth-order effective mode area, $A_{5,\text{eff}}$, is given by [19, 25]

$$A_{5,\text{eff}} \equiv \left[\frac{\iint |f(x,y)|^6 \mathrm{d}x\mathrm{d}y}{\iint |f(x,y)|^2 \mathrm{d}x\mathrm{d}y}\right]^{1/2} \tag{3.10}$$

where $f(x,y)$ is the transverse mode distribution of the TE eigenstate discussed in Sec. 2.4. For simplicity, we have assumed that the entire transverse mode lies within the core region, and we have therefore omitted the use of mode confinement factors in Eq. (3.9), which could be included to account for the partial overlap of the mode with the cladding.

We note that the model given in Eq. (3.9) does not account for free-carrier nonlinearities, which can occur once free carriers are generated by two- or three-photon absorption. In this respect, α_2 and α_3 represent "effective" nonlinear absorption coefficients as they potentially include free-carrier contributions. However, for the range of intensities achieved during the experiment, free-carrier absorption is expected to be a small effect [67], which will be discussed further in the following paragraphs.

The green squares in Fig. 3.10 show the inverse-transmission data of Waveguide I. For the intensity-regime achieved in the experiment, we expect $I(z,t)$ to remain much less than the ratio α_2/α_3 [67], and the three-photon-absorption term in Eq. (3.9) may be neglected. In this approximation, Eq. (3.9) can be integrated to yield

$$I(L,t) = \frac{e^{-\alpha L} I(0,t)}{1 + \alpha_2 I(0,t) L_{\text{eff}}} \tag{3.11}$$

where L is the waveguide's physical length and $L_{\text{eff}} \equiv (1 - e^{-\alpha L})/\alpha$. For a sech-squared pulse-shape, where $I(0,t) = I_0 \operatorname{sech}^2(t/t_0)$, we have [68]

$$\frac{1}{T} = \frac{e^{\alpha L}(1 + \alpha_2 L_{\text{eff}} I_0)^{1/2} (\alpha_2 L_{\text{eff}} I_0)^{1/2}}{\ln[(1 + \alpha_2 L_{\text{eff}} I_0)^{1/2} + (\alpha_2 L_{\text{eff}} I_0)^{1/2}]} \tag{3.12}$$

The $1/T$-trend of Waveguide I is nearly linear as a function of the input intensity. According to Eq. (3.12), this type of intensity-dependence is indicative of a system dominated by two-photon absorption, which is expected due to Waveguide I's relatively narrow bandgap. (The slight downward curvature of the linear trend results from modification of the pulse-shape due to preferential nonlinear absorption of the pulse-center.) The solid green line in Fig. 3.10 is a best-fit using Eq. (3.12) and

adjusting α_2 as a free parameter. The best-fit two-photon-absorption coefficient is $\alpha_2 = 3.3$ cm/GW.

Again, in analyzing the nonlinear response of Waveguide I, we have used a model which ignores free-carrier effects. To justify this simplification, we employ the approach of Yin and Agrawal, detailed in [69]. Including the effects of free carriers using a simple Drude model, the equation which describes the propagation of the pulse-envelope is [23, 68–70]

$$\begin{aligned}\frac{\partial u(z,t)}{\partial z} =& -\frac{\alpha}{2}u(z,t) \\ &+\Big(i\frac{\omega}{c}n_2 - \frac{\alpha_2}{2}\Big)\frac{|u(z,t)|^2}{A_{\text{eff}}}u(z,t) \\ &-\Big(i\frac{\omega}{c}\Delta n_{\text{FCD}} + \frac{\Delta\alpha_{\text{FCA}}}{2}\Big)u(z,t)\end{aligned} \tag{3.13}$$

where, as usual, $u(z,t)$ represents the envelope of the field normalized such that $|u(z,t)|^2 = P(z,t)$, and we have again omitted any effects due to the waveguide's dispersion. The factors Δn_{FCD} and $\Delta\alpha_{\text{FCA}}$ represent, respectively, free-carrier dispersion and free-carrier absorption. We assume Δn_{FCD} and $\Delta\alpha_{\text{FCA}}$ are proportional to the instantaneous carrier concentration, $N_c(z,t)$, which is zero prior to the arrival of the pulse:

$$\Delta\alpha_{\text{FCA}}(z,t) = \sigma_{\text{FCA}}N_c(z,t) \tag{3.14}$$

$$\Delta n_{\text{FCD}}(z,t) = k_{\text{FCD}}N_c(z,t) \tag{3.15}$$

Here, σ_{FCA} and k_{FCD} are the free-carrier-absorption cross-section and the free-carrier-dispersion coefficient, respectively. We assume the free-carriers are generated exclusively by two-photon absorption and that all the carrier recombination

processes are described by a single time constant. Therefore, the instantaneous carrier concentration (which is averaged across the third-order effective mode-area), evolves according to

$$\frac{\partial N_c(z,t)}{\partial t} = \frac{\alpha_2}{2\hbar\omega}\left(\frac{|u(z,t)|^2}{A_{\text{eff}}}\right)^2 - \frac{N_c(z,t)}{\tau_c} \tag{3.16}$$

where τ_c is the free-carrier lifetime.

To obtain an estimate of the importance of free-carrier absorption relative to two-photon absorption, we consider the limiting case of the highest possible free-carrier density. Focusing on the waveguide's input port, where the pulse-intensity is strongest, we assume none of the free-carriers have sufficient time to recombine as the pulse passes through the input port. We can then estimate the upper limit of the free-carrier density at the input port at the instant just after the pulse has passed by setting the second term in Eq. (3.16) to zero and integrating over all time. To make the integration possible, the pulse is assumed to have a Gaussian shape (rather than a sech^2 shape) such that $|u(z=0,t)|^2/A_{\text{eff}} = I_0 \exp\left[-4\ln 2(t/\tau_g)^2\right]$, where I_0 is the peak mode-averaged intensity at the input port and τ_g is the full-width at half-maximum of the intensity profile of the Gaussian pulse. The upper limit of the free-carrier concentration at the input port is therefore

$$N_{\max}(z=0) = \frac{\sqrt{\pi}}{4\sqrt{\ln 4}}\left(\frac{\alpha_2 I_0^2 \tau_g}{\hbar\omega}\right) \tag{3.17}$$

For the Waveguide-I experiment, $\tau_g = 1.7$ ps and $I_0 \leq 3.5$ GW/cm^2.

Inspecting the terms in Eq. (3.13), we can define a figure-of-merit, r_{FCA}, to specify the importance of free-carrier absorption relative to two-photon absorption.

This ratio consists of the peak free-carrier absorption compared to the peak two-photon absorption:

$$r_{\mathrm{FCA}} = (\frac{\sigma_{\mathrm{FCA}} N_{\max}}{2})/(\frac{\alpha_2}{2} I_0) = \frac{\sqrt{\pi}\tau_g}{4\sqrt{\ln 4}\hbar\omega}\sigma_{\mathrm{FCA}} I_0 \tag{3.18}$$

We assume the cross-section for free-carrier absorption is the same as that for GaAs, $\sigma_{\mathrm{FCA}} = 1.5 \times 10^{-16}$ cm^2 [70]. The figure-of-merit for the highest intensity launched into Waveguide I is therefore $r_{\mathrm{FCA}} \approx 2.5$. This suggests that, at least for the highest intensities used in the experiment, free-carrier absorption may be comparable to two-photon absorption. However, the free-carrier density used to calculate r_{FCA} is a conservative over-estimate of the actual density at the input port. Furthermore, the calculations leading to this figure-of-merit assume the entire pulse samples this maximum free-carrier concentration. In reality, the free-carrier concentration builds up continuously as the pulse passes the input port, and only the trailing edge of the pulse samples the peak free-carrier concentration. Also, because Waveguide I exhibits substantial nonlinear absorption, the pulse power quickly decays with distance along the waveguide and r_{FCA} therefore also quickly decays as a function of z. This means that free-carrier absorption is probably only important over a relatively small distance at the waveguide's input port, while two-photon absorption remains important over the entire waveguide-length.

Finally, we note that the single-parameter model of Eq. (3.12) predicts the entire observed nonlinear-transmission trend of Waveguide I very well. This provides further evidence that nonlinear absorption in this system is dominated by two-photon absorption. Free-carrier absorption is effectively a fifth-order nonlin-

earity; if it were significant, free-carrier absorption would cause the $1/T$-trend of Waveguide I to follow a different functional form than that predicted by Eq. (3.12). Thus, we are justified to apply Eq. (3.12) to estimate the waveguide's two-photon-absorption coefficient. However, as we have already acknowledged, the estimated two-photon-absorption coefficient probably includes a small contribution caused by free-carrier nonlinearities. Indeed, as discussed later, the power-dependent asymmetry of the Waveguide-I output spectra indicates that free-carrier dispersion is important for the highest powers launched into the waveguide (the Waveguide-I spectra in Fig. 3.11 exhibit a blue-shift as the launched power is increased). No doubt, there is some degree of free-carrier absorption contributing to the nonlinear transmission of Waveguide I. Our intent here is not so much to obtain an exact value for the two-photon absorption coefficient of Waveguide I as it is to show that, due to its narrow bandgap, nonlinear absorption in this waveguide is relatively large.

We now consider the trend observed for Waveguide II. The core-bandgap of Waveguide II is 1.66 eV, and two-photon absorption should be absent for wavelengths significantly longer than 1494 nm. Indeed, the small slope and upward curvature of the $1/T$-data (the blue circles in Fig. 3.10) suggest two-photon absorption is negligible. Omitting the two-photon-absorption term, Eq. (3.9) takes the solution

$$I(L,t) = \frac{e^{-\alpha L} I(0,t)}{\left[1 + \Gamma \frac{\alpha_3}{\alpha} I^2(0,t)(1 - e^{-2\alpha L})\right]^{1/2}} \tag{3.19}$$

and the transmittance of a sech-squared pulse then becomes

$$T = (2t_0\, e^{\alpha L})^{-1} \int_{-\infty}^{\infty} \frac{\operatorname{sech}^2(t/t_0)}{\left[1 + \Gamma \frac{\alpha_3}{\alpha} I_0^2 \operatorname{sech}^4(t/t_0)(1 - e^{-2\alpha L})\right]^{1/2}}\, \mathrm{d}t \tag{3.20}$$

Equation (3.20) has no analytical solution. But, numerical integration of the equation predicts that the quantity $(1/T)^2$ should be approximately linear when plotted as a function I_0^2 for a system dominated by three-photon absorption [71], which is the behavior observed in the Inset of Fig. 3.10. By numerically evaluating Eq. (3.20) and adjusting α_3 to match the experimental results (see the solid blue lines in Fig. 3.10), we obtain an estimate for α_3. The best fit uses $\alpha_3 = 6.5 \times 10^{-2}$ cm^3/GW^2, in excellent agreement with published values [67]. (Using the modesolver, Γ is calculated to be 1.27 for Waveguide II.)

Now we consider the power-dependent changes to the output spectra, shown in Fig. 3.11. These spectra were observed with the same experimental conditions used for the power-dependent transmission experiments. The spectra of Waveguide I, depicted in green, become asymmetric and exhibit a blue-shift as the power is increased – a telltale marker produced by non-instantaneous nonlinear refraction from a plasma of free carriers [72, 73]. In contrast, the spectra of Waveguide II remain symmetric as the power is increased. Additionally, for a given power level, the Waveguide-II spectrum displays a larger nonlinear phase shift compared to the Waveguide-I spectrum; this is because Waveguide II possesses smaller linear and nonlinear losses and therefore the optical field remains undepleted, able to generate a larger phase shift.

The dashed cyan lines in the right-hand column of Fig. 3.11 are calculations of the output spectra for Waveguide II. These were obtained using the Split-Step Fourier Transform (SSFT) method [66] to simulate propagation of a hyperbolic-secant-squared pulse in the nonlinear waveguide. The SSFT method was imple-

mented using publicly available software called SSPROP [74], modified to include three-photon absorption. The mathematical model used to simulate the pulse propagation is

$$\frac{\partial}{\partial z}u(z,t) = -\frac{\alpha}{2}u(z,t) + i\gamma_3|u(z,t)|^2u(z,t) + i\gamma_5|u(z,t)|^4u(z,t) \tag{3.21}$$

where $u(z,t)$ is the slowly-varying field amplitude, normalized such that $|u(z,t)|^2$ is the instantaneous power in the fundamental TE mode. As with the model of Eq. (3.9), this model neglects the effects of linear dispersion because the dispersion-length of the waveguide is much longer than its physical length.

The factors γ_3 and γ_5 appearing in Eq. (3.21) are the third-order and fifth-order nonlinear parameters, respectively. To be consistent with the observations of Fig. 3.10, the two-photon absorption is assumed to be negligibly weak, such that γ_3 includes only a refractive component, $\gamma_3 \approx \omega n_2/(cA_{\text{eff}})$. It is also assumed that the third-order nonlinear refraction dominates any fifth-order nonlinear refraction, such that γ_5 only includes an absorption term, $\gamma_5 \approx i\alpha_3/(2A_{5,\text{eff}}^2)$.

For Waveguide II, $A_{5,\text{eff}}$ is calculated to be 0.64 μm^2. The value assigned to α_3 is that measured during the nonlinear transmission experiment: $\alpha_3 = 6.5 \times 10^{-2}$ cm^3/GW^2. The value of n_2 is adjusted as a free parameter to match the calculated spectra to the experimental spectra. The best-fit value is $n_2 = 1.45 \times 10^{-4}$ cm^2/GW. It is important to point out that it is only possible to achieve a nice match between the simulations and the experimental data when the effects of both n_2 and α_3 are included in the model. Trial and error shows that no combination of two-photon absorption and Kerr refraction can produce the observed spectra. In

combination with the observations of Fig. 3.10, this provides evidence that the larger bandgap of Waveguide II completely quenches two-photon absorption at 1550 nm.

3.5 Power-dependence of four-wave mixing in AlGaAs waveguides

This section compares the continuous-wave four-wave-mixing efficiency of four waveguides, which include the two waveguides just discussed in Sect. 3.4. The cross sections and linear properties of the waveguides are depicted in Fig. 3.12, and they are labeled Waveguides I through IV in order of ascending bandgap (Waveguides I and II of the preceding section retain the same labels).

The measured core-bandgaps of the four waveguides range from $E_g = 1.60$ eV to $E_g = 1.79$. As demonstrated in Sect. 3.4, two-photon absorption at 1550 nm is expected only for Waveguide I. The calculated group-velocity dispersions range from $\beta_2 = 0.45 \pm 0.05$ ps^2/m (for Waveguide IV) to $\beta_2 = 1.05 \pm 0.05$ ps^2/m (for Waveguide I).

To measure the continuous-wave four-wave-mixing efficiency, two continuous-wave external cavity lasers are separately amplified to produce the pump and signal, respectively. The wavelength range over which efficient four-wave-mixing can be achieved is constrained by the dispersion, device length, and the pump power [75]. For the measurements presented in this section, the wavelength separation between the pump and signal, $\Delta\lambda$, is fixed less than 1 nm to ensure the group-velocity mismatch is essentially zero. In other words, the intentionally small pump-signal spacing guarantees that $\Delta\beta \approx 0$. Therefore the complex exponential factors in

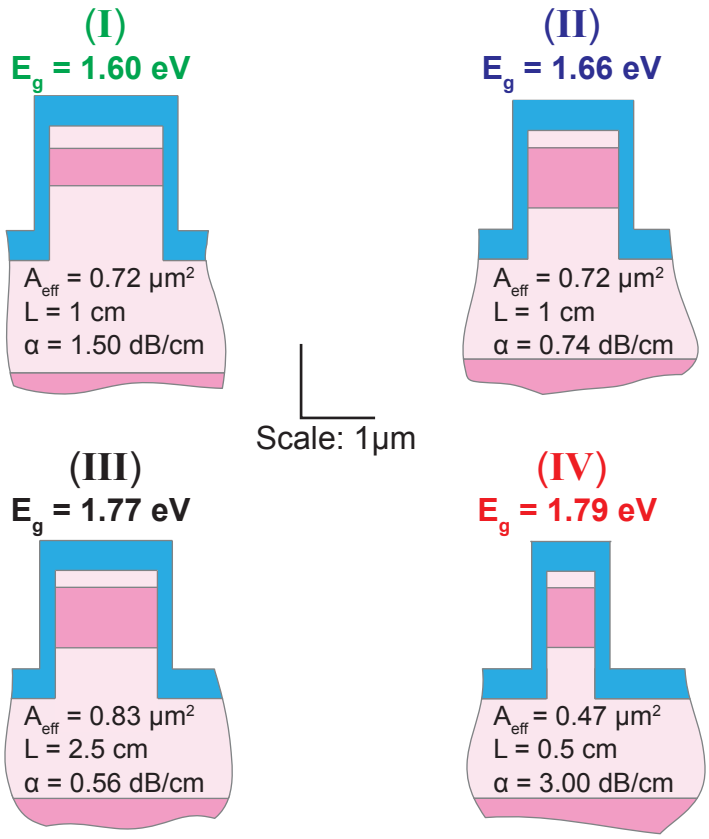

Figure 3.12: Cross sections and properties of the waveguides studied in the four-wave-mixing experiments, labeled I through IV in order of ascending core-bandgap. (Waveguides I and II here are the same as those in Fig. 3.8.)

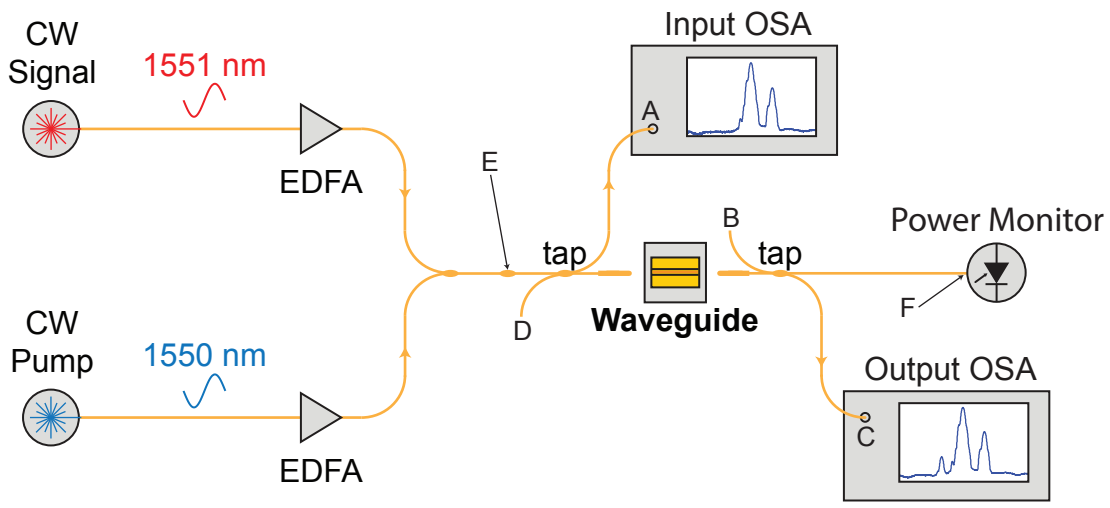

Figure 3.13: The experimental setup used to measure the power-dependent four-wave-mixing efficiency of Waveguides I through IV. CW: continuous-wave; EDFA: erbium-doped fiber amplifier; OSA: optical spectrum analyzer; tap: 2×2 polarization-maintaining 95/5 combiner. The points labeled A-F indicate FC/APC connectors which are arranged to run the experiment either in the left-to-right or the right-to-left direction.

Eqs. (2.65a-c) play no role in determining the four-wave-mixing efficiency. (The bandwidth of phase-matching is considered in Sect. 3.6.)

The pump and signal are combined using a 50/50 polarization-maintaining combiner. The co-polarized waves are then launched into the waveguide under test using a polarization-maintaining lensed fiber, which is rotated to ensure only the TE eigenstate is excited. A 95/5 tap coupler immediately prior to the waveguide is used to monitor the power and spectrum. At the output, a second lensed fiber and tap coupler collect the idler, signal and pump to measure the output power and spectrum. The experimental setup is depicted in Fig. 3.13.

The input and output coupling assemblies are identical and symmetrical about

the waveguide. During the experiment, the pump power is swept and the power-dependent four-wave-mixing efficiency is recorded. Experiments are run in both directions through the waveguide. In Fig. 3.13, the experiment is setup to run in the left-to-right direction through the waveguide. To conduct the same experiment in the right-to-left direction, the FC/APC connectors at points E and F are exchanged to reverse the direction of the optical waves relative to the waveguide. The connectorized pigtails of the power taps are also rearranged such that the connectors at A and B are exchanged and the connectors at C and D are exchanged. By comparing experiments run in both directions through the waveguide, the facet loss at each side is independently measured. This approach takes advantage of the fact that, while no two lensed fibers and/or waveguide facets are identical, FC/APC connectors are quite uniform and allow for repeatable connections.

The four-wave-mixing conversion efficiency is defined as the ratio of the output idler power to the input signal power,

$$\eta_{\mathrm{FWM}} \equiv \frac{P_i(L)}{P_s(0)} \tag{3.22}$$

As derived in Appendix A, in the low-conversion-efficiency limit (i.e., $P_p \gg P_s \gg P_i$) and assuming zero group-velocity mismatch (i.e., $\Delta\beta = 0$), the conversion efficiency can be approximated as

$$\eta_{\mathrm{FWM}} \approx e^{-\alpha L}(|\gamma| P_{p0} L_{\mathrm{eff}})^2 \tag{3.23}$$

where $\gamma = (\frac{\omega n_2}{c} + i\frac{\alpha_2}{2})/A_{\mathrm{eff}}$ is the waveguide's complex nonlinear parameter, P_{p0} is the inserted pump power, $L_{\mathrm{eff}} = (1 - e^{-\alpha L})/\alpha$ is the effective nonlinear length, α is the propagation loss and L is the waveguide's physical length. Again, Eq. (3.23) is

valid only in the low-conversion-efficiency limit and does not model the saturation of the conversion efficiency caused by two-photon absorption. It is worth pointing out that, at least in principle, it is possible to derive an expression for the conversion efficiency that includes the saturation-effect caused by two-photon absorption, as in Eq. (A.26) of Appendix A. However, once two-photon absorption begins, other loss mechanisms (like free-carrier absorption) become important and limit the conversion efficiency more strongly than predicted by Eq. (A.26).

Figure 3.14 shows the measured conversion efficiencies. For data such as these, it is conventional simply to graph the dependence on the inserted pump power in order to observe whether the trend adheres to the square-law form predicted by Eq. (3.23). However, here we compare the nonlinear performance of several waveguides having different linear characteristics. Therefore, to normalize-out the linear properties, Fig. 3.14 shows the efficiencies versus the quantity $\frac{L_{\text{eff}}}{A_{\text{eff}}} e^{-\frac{1}{2}\alpha L} \times P_{p0}$; this allows a direct comparison of material-dependent nonlinearity of the waveguides.

Perhaps counter-intuitively (because it *does* exhibit two-photon absorption), Waveguide I initially generates the largest conversion efficiency. This is because Waveguide I has the narrowest bandgap of the four waveguides, and therefore possesses the largest Kerr refraction coefficient and two-photon absorption coefficient, as predicted by the model of Sheik-Bahae, et al. [22] (see Fig. 2.6). Thus, the magnitude of its nonlinear parameter is the largest. However, nonlinear absorption limits the achievable conversion efficiency, and the Waveguide-I efficiency saturates as the inserted power increases.

In contrast, the nonlinear absorption of Waveguides II through IV is negligible,

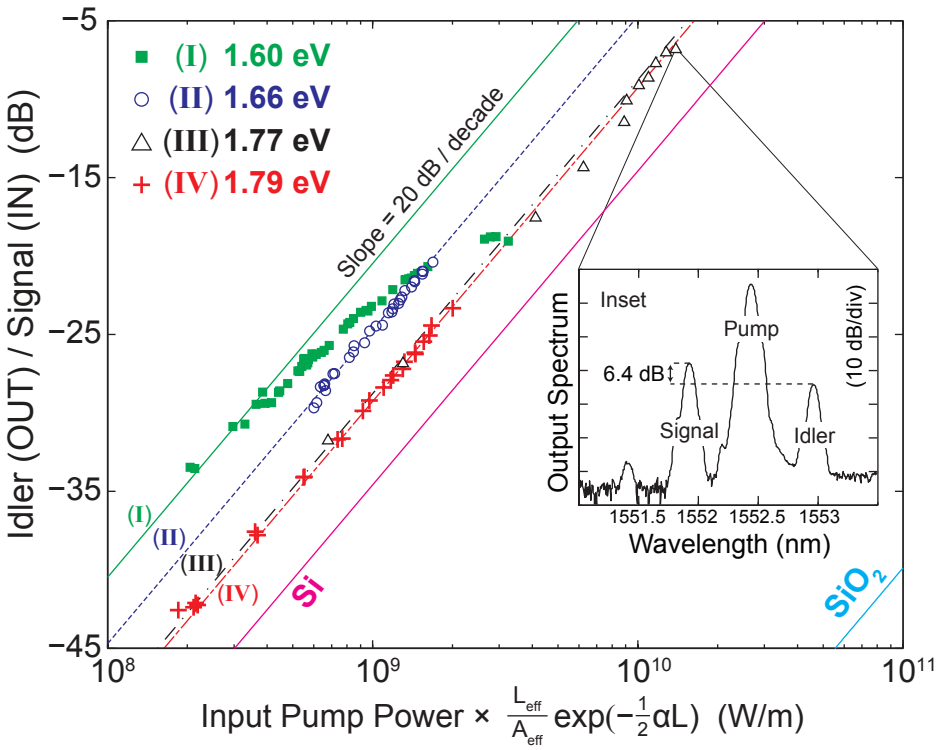

Figure 3.14: The continuous-wave four-wave-mixing conversion efficiency of Waveguides I through IV as a function of the quantity $P_{p0}\frac{L_{\rm eff}}{A_{\rm eff}}e^{-\frac{1}{2}\alpha L}$. The symbols represent the measured efficiencies and the solid lines represent calculations according to Eq. (3.23). Inset: The output spectrum observed for the highest conversion efficiency.

and the conversion efficiency scales quadratically up to the damage threshold of the waveguide. The highest conversion efficiency was obtained in Waveguide III, and the corresponding output spectrum is shown in the inset to Fig. 3.14. Waveguide III possesses the unique combination of negligible two-photon absorption, small propagation loss, and a large physical length. In particular, the low propagation loss of this waveguide – achieved using the reflow process discussed in Sect. 3.2 – allowed the insertion of significantly more pump power (up to 630 mW) without damage to the device. The output spectrum shows that the ratio of the output idler to the output signal is -6.4 ± 0.1 dB. Accounting for the facet losses and propagation loss, the peak conversion efficiency (${P_i}^{\text{out}}/{P_s}^{\text{in}}$) is therefore -6.8 ± 1.2 dB; the larger uncertainty in this quantity stems from the compounded uncertainties in partitioning all the contributions to the total insertion loss. This result is comparable with the highest reported continuous-wave conversion efficiency achieved in any passive semiconductor or glass waveguides [37,46,50,54,76]. It is orders of magnitude higher than any previously reported continuous-wave conversion efficiency for an AlGaAs waveguide [59, 61], and marks an important step in the development of AlGaAs waveguides for nonlinear optical processing.

It is important to mention that while the properties of Waveguide III allow for very efficient four-wave mixing, the measured peak conversion efficiency does not represent a fundamental limit. If Waveguide III were much longer, substantial gains would occur in terms of the expected peak conversion efficiency for the same inserted power. All other things held equal, the ideal-case length for a waveguide similar to Waveguide III is $L_{\text{opt}} = \frac{\ln 3}{\alpha} = 8.5$ cm [77], which is found by optimizing

Table 3.2: The nonlinear coefficients used to calculate the low-conversion-efficiency lines of Fig. 3.14.

	Bandgap (eV)	n_2 ($\mathrm{cm}^2/\mathrm{GW} \times 10^4$)	α_2 (cm/GW)
Waveguide I	1.60	2.3	3.3
Waveguide II	1.66	1.45	0
Waveguide III	1.77	0.90	0
Waveguide IV	1.79	0.85	0
Crystalline Silicon [21, 78]	1.2	0.45	0.79
Silica Glass [66]	–	0.002	0

Eq. (3.23) with respect to the length of the waveguide. Such a waveguide would be expected to produce the same conversion efficiency for less than half the pump power inserted in Waveguide III. Alternatively, the expected conversion efficiency would be 0 dB if the same maximum pump power (630 mW) were launched into the optimal-length device.

The straight lines in Fig. 3.14 show the low-conversion-efficiency scaling relationships predicted by Eq. (3.23). The positions of these lines depend only on the quantity $|\frac{\omega n_2}{c} + i\frac{\alpha_2}{2}|$. Because both n_2 and α_2 decrease as the bandgap increases (as discussed in Sect. 2.5), these lines are ordered in increasing bandgap from top-left to bottom-right. Included for comparison are the low-efficiency relationships expected for crystalline silicon and silica glass. Table 3.2 gives the nonlinear coefficients used to generate the low-efficiency scaling relationships. The nonlinear coefficients used for each of the AlGaAs waveguides are in good agreement with published values [25, 58].

3.6 Bandwidth of four-wave mixing in AlGaAs waveguides

To achieve a large FWM conversion bandwidth, the GVD of the waveguide needs to be near zero or anomalous. It is easiest to see this by re-casting Eqs. (2.65) in terms of the optical power of each wave. Doing so results in the following coupled equations [13, 15, 79]:

$$\begin{aligned}\frac{dP_p}{dz} =& -\alpha P_p - \frac{\alpha_2}{A_{\text{eff}}}\left(P_p + 2P_s + 2P_i\right)P_p \\ &- 4\frac{\omega n_2}{cA_{\text{eff}}}P_p\sqrt{P_sP_i}\sin\theta - 2\frac{\alpha_2}{A_{\text{eff}}}P_p\sqrt{P_sP_i}\cos\theta \end{aligned} \tag{3.24a}$$

$$\begin{aligned}\frac{dP_s}{dz} =& -\alpha P_s - \frac{\alpha_2}{A_{\text{eff}}}\left(2P_p + P_s + 2P_i\right)P_s \\ &+ 2\frac{\omega n_2}{cA_{\text{eff}}}P_p\sqrt{P_sP_i}\sin\theta - \frac{\alpha_2}{A_{\text{eff}}}P_p\sqrt{P_sP_i}\cos\theta \end{aligned} \tag{3.24b}$$

$$\begin{aligned}\frac{dP_i}{dz} =& -\alpha P_i - \frac{\alpha_2}{A_{\text{eff}}}\left(2P_p + 2P_s + P_i\right)P_i \\ &+ 2\frac{\omega n_2}{cA_{\text{eff}}}P_p\sqrt{P_sP_i}\sin\theta - \frac{\alpha_2}{A_{\text{eff}}}P_p\sqrt{P_sP_i}\cos\theta \end{aligned} \tag{3.24c}$$

$$\begin{aligned}\frac{d\theta}{dz} =& (\beta_s + \beta_i - 2\beta_p) + \frac{\omega n_2}{cA_{\text{eff}}}\left(2P_p - P_s - P_i\right) \\ &+ \frac{\omega n_2}{cA_{\text{eff}}}\left(P_p\sqrt{\frac{P_s}{P_i}} + P_p\sqrt{\frac{P_i}{P_s}} - 4\sqrt{P_sP_i}\right)\cos\theta \\ &+ \frac{\alpha_2}{A_{\text{eff}}}\left(P_p\sqrt{\frac{P_s}{P_i}} + P_p\sqrt{\frac{P_i}{P_s}} - 4\sqrt{P_sP_i}\right)\sin\theta \end{aligned} \tag{3.24d}$$

where P_m and β_m with $m = \{p, s, i\}$ represent the powers and propagation constants of the pump, signal and idler waves, and $\omega = \omega_p$ is the optical center frequency. In Eqs. (3.24a-d), $\theta(z)$ represents the local relative phase among the four interacting waves:

$$\theta(z) = \Delta\beta z + \phi_s(z) + \phi_i(z) - 2\phi_p(z) \tag{3.25}$$

The first term on the RHS of Eq. (3.25) represents the (linear) effect of the dispersion of the waveguide. Any non-zero group-velocity mismatch will tend to cause the angle θ to change in z. The remaining terms represent the phases of the complex amplitudes of the signal, idler and pump, respectively. These include the phase of each wave at $z = 0$ and any additional phase accumulated due to the nonlinear interaction in the waveguide.

Equation (3.24d) governs the extent to which phase-matching is satisfied. To define what this means exactly, consider what happens at the waveguide's input port. The idler is not present at $z = 0$, and it initially builds up as a result of parametric amplification of background electromagnetic fluctuations. Evaluating the buildup of the idler across the infinitesimal distance $\mathrm{d}z$ at the input port, according to Eq. (2.65c), we have

$$\mathrm{d}u_i = i\gamma u_p^2 u_s^* e^{-i\Delta\beta z}\mathrm{d}z \tag{3.26}$$

Using phasor notation, Eq. (3.26) becomes

$$\mathrm{d}(m_i e^{i\phi_i}) = i\gamma m_p^2 m_s e^{i(-\Delta\beta z + 2\phi_p - \phi_s)}\mathrm{d}z, \tag{3.27}$$

from which we can conclude that the phase of the generated idler is $\phi_i = \pi/2 - \Delta\beta z + 2\phi_p - \phi_s$. Inserting this into Eq. (3.25), it is clear the local phase mismatch auto-initializes to $\theta = \pi/2$ at the waveguide's input port, regardless the relative phases of the pump and signal [79].

According to Eqs. (3.24a–c), $\theta = \pi/2$ allows power to flow most efficiently from the pump to the signal and idler. This is the case of ideal parametric amplification. The four-wave-mixing process is then said to be "perfectly phase-matched."

Some degree of parametric amplification will occur so long as θ remains on the interval $(0, \pi)$. But, once θ crosses to the interval $(-\pi, 0)$, the direction of power flow reverses, and the idler and signal begin to feed the pump (parametric attenuation) [13]. Therefore, to achieve broadband four-wave mixing, the waveguide must be engineered to maintain $\theta(z)$ as close as possible to $\pi/2$ considering all the contributions to Eq. (3.24d).

Consider the case of a bandgap-engineered AlGaAs waveguide, where two-photon absorption is negligibly small. Close to the input port, θ remains sufficiently close to $\pi/2$ that $\cos\theta \approx 0$. We will assume $P_p \gg P_s \gg P_i$ and therefore, near the input port, Eq. (3.24d) is approximately [13, 35, 80]

$$\frac{d\theta}{dz} \approx (\beta_s + \beta_i - 2\beta_p) + 2\frac{\omega n_2}{cA_{\text{eff}}}P_p \tag{3.28}$$

To maintain $\theta(z)$ at $\pi/2$ along the length of the waveguide, we require that the terms on the RHS of Eq. (3.28) sum to zero. In the small-power limit, the power-dependent term becomes exceedingly small, and the phase-matching condition can be met simply by tailoring a zero-dispersion waveguide, as discussed in Sect. 3.3.2. For large optical power, the power-dependent term becomes important. Because the Kerr nonlinearity is positive, ideal phase-matching can then be maintained only if the group-velocity mismatch is negative, meaning anomalous dispersion. Anomalous dispersion is a prerequisite to achieve broadband parametric gain (simultaneous wavelength conversion and net signal gain), which has been achieved in many of the other semiconductor waveguide platforms described in Sect. 3.1 (albeit using short optical pulses rather than a continuous-wave pump; continuous-wave parametric

gain has not yet been demonstrated in a passive semiconductor waveguide).

Unfortunately, with the installed fabrication tools, it is not possible to fabricate low-loss AlGaAs waveguides with anomalous GVD at 1550 nm. According to the calculations shown in Fig. 3.7, the width of a SiN-coated waveguide must be less than 600 nm to achieve zero GVD, a feature-size which leads to unacceptably high propagation loss due to increased sidewall scattering. However, by removing the SiN encapsulant layer from the narrowest waveguide with acceptable propagation loss, it is at least possible to approach zero GVD and this allows for a very large conversion bandwidth.

To measure the four-wave-mixing bandwidth, the same experimental setup depicted in Fig. 3.13 is used. The wavelength of the pump is fixed and the power and spectrum of the pump, signal and idler are recorded as the signal wavelength is swept. The largest recorded bandwidth is shown in Fig. 3.15, which was obtained using a 5-mm-long, 0.69-μm-wide AlGaAs waveguide having the same vertical profile shown in Fig. 2.3. The measured propagation loss of the device is 1.11 dB/cm. The same waveguide was tested before and after removal of the SiN encapsulant from the sidewalls (but not from the facets), and as predicted the bandwidth increases substantially when the encapsulant is removed. In these experiments, the pump wavelength is fixed at 1550 nm, and the signal wavelength varies from 1551 nm to 1630 nm, as limited by the laser tuning range. The half-width 3-dB conversion bandwidth is measured to be 44.4 nm for the coated waveguide, and 63.8 nm for the uncoated waveguide.

The solid lines in Fig. 3.15 show the calculated conversion efficiencies, which

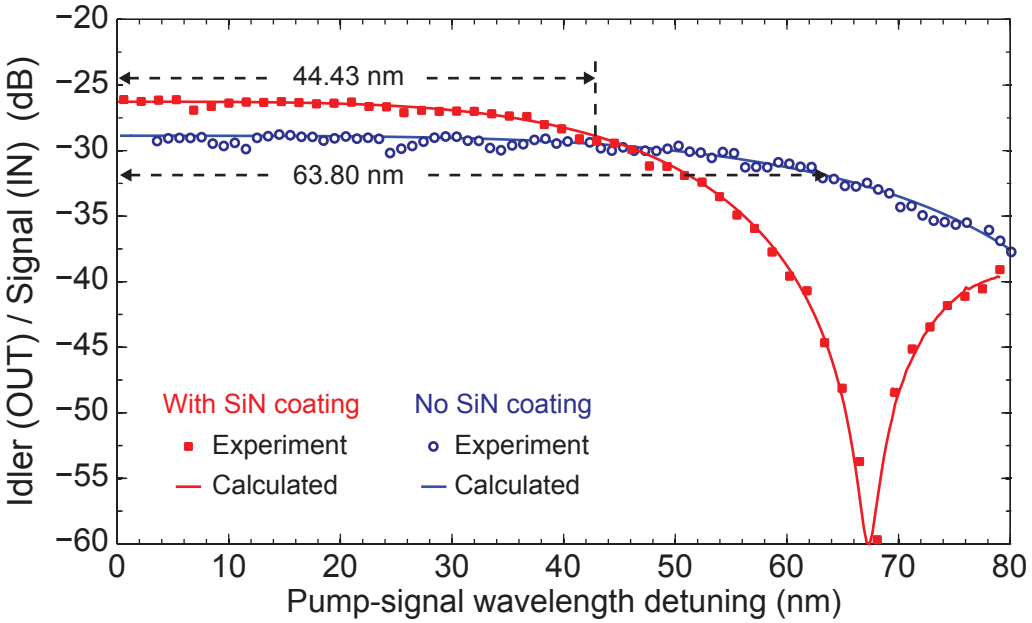

Figure 3.15: Measured and calculated conversion efficiencies as a function of the pump-signal wavelength detuning. The waveguide-under-test is similar to that depicted in Fig. 2.3, but the width of the core-layer is 0.69 μm. The data shown in red are the results when the waveguide is coated with a layer of SiN encapsulant. The data shown in blue are the results for the same waveguide after the encapsulant layer is removed from the sidewalls; the waveguide then exhibits a larger bandwidth indicating a smaller group-velocity dispersion.

are obtained by numerically integrating Eqs. (3.24). In these calculations, the group-velocity mismatch is approximated using the second-order expansion of Eq. (3.6), and β_2 is adjusted as the only free parameter in the calculation. The core-layer of this waveguide is the same material as that in Waveguide III of Sect. 3.5, and the corresponding nonlinear coefficients shown in Table 3.2 are incorporated into the calculations. The calculated effective mode area of the waveguide is 0.4 μm^2. By adjusting β_2 to match the experimental data, the GVD at the pump wavelength is estimated to be $\beta_2 = +0.44$ ps^2/m for the coated waveguide and $\beta_2 = +0.22$ ps^2/m after the coating is removed. These estimates of the total dispersion closely match the predictions of the modesolving calculations, shown in Fig. 3.7.

It is important to mention that many AlGaAs waveguides of various dimensions were tested to verify the role of the waveguide's geometry in determining the net dispersion. The results shown in Fig. 3.15 are the only results included here because they represent the largest bandwidth achieved in any of the tested devices. Comparison of the observed FWM bandwidths of all the tested waveguides to the corresponding calculated group-velocity dispersions confirms that the dispersion-calculation method explained in Sec. 3.3.2 is quite accurate (for further details, see [81]).

While it is not yet possible to achieve the combination of anomalous dispersion with low propagation loss in an AlGaAs waveguide, the results of this section represent a major step forward for large-bandwidth, efficient wavelength conversion in AlGaAs waveguides. Anomalous GVD has been previously demonstrated in an AlGaAs waveguide [57], but only in a waveguide with propagation loss so high (80

dB/cm) as to render it essentially useless. Here, we have demonstrated a bandgap-engineered AlGaAs waveguide with near-zero GVD *and* low propagation loss, which allows high-efficiency conversion over a 63.8-nm band (or 127.6 nm, measured from signal to idler).

3.7 Summary

This chapter reports several measurements of nonlinear AlGaAs waveguides, with the intent to characterize their suitability for all-optical wavelength conversion. The chapter begins by describing what a wavelength converter is, why such a device is useful, and justifies the need for an ultrafast all-optical wavelength converter based on exploiting continuous-wave four-wave mixing in nonlinear waveguides. The relative merits and achievements of various competing nonlinear-waveguide material systems are discussed, and bandgap-engineered AlGaAs is presented as an attractive alternative to other material systems, principally because it possesses a large nonlinearity and it is possible to minimize nonlinear absorption by tailoring the bandgap of the alloy.

The MBE growth and photolithographic fabrication of the waveguides is explained with special emphasis on the photoresist-reflow method, which allows for the fabrication of narrow, low-loss AlGaAs ridge waveguides. The experimental and computational techniques used to characterize the linear properties of the waveguides – the propagation loss, the effective mode area, the core-bandgap, and the group-velocity dispersion – are discussed.

Measurements of the power-dependent nonlinear transmission and spectral broadening are presented for two AlGaAs waveguides: one which has a narrow bandgap and therefore exhibits two-photon absorption, and one which has a wide bandgap and therefore exhibits no two-photon absorption. Mathematical modeling is used to estimate the nonlinear coefficients of the waveguides by matching calculated results to the experimental results. The analysis of the experiments confirms that tailoring the bandgap of the core-layer suppresses two-photon absorption but retains a large refractive nonlinearity, ideal for nonlinear signal processing.

The power-dependence of continuous-wave four-wave mixing is documented for four AlGaAs waveguides, which have different core-layer bandgaps. It is observed that nonlinear absorption in the narrowest-bandgap waveguide limits the achievable conversion efficiency. The remaining waveguides exhibit no two-photon absorption, and the achievable efficiency is limited by the damage threshold of each device. In particular, a high-quality, bandgap-engineered AlGaAs waveguide with sub-dB/cm propagation loss is used to generate a continuous-wave conversion efficiency of -6.8 dB, which is comparable to the highest reported continuous-wave efficiencies of competing material systems.

The continuous-wave four-wave mixing bandwidth of dispersion-engineered AlGaAs waveguides is presented. The dependence of the four-wave-mixing bandwidth on the group-velocity dispersion is described, and the requirements to achieve phase-matching are outlined. Near-zero GVD is achieved by removing the SiN encapsulant from a narrow, low-loss AlGaAs waveguide. This results in a 3-dB spectral bandwidth of 63.8 nm with adequate conversion efficiency for real applications.

Chapter 4: Measuring the Nonlinear Loss Tangent

4.1 Overview

As discussed extensively in the preceding chapters, low-loss, sub-micron waveguides are promising candidates for nonlinear optical signal processing, and could enable chip-scale devices for wavelength conversion, optical switching, and an array of other processes. Extensive research has focused on the use of semiconductor waveguides for these purposes, and it is generally recognized that two-photon absorption (and subsequent free-carrier absorption) is a factor that limits the efficiency of many desirable nonlinear processes [82, 83]. Therefore, the conventional figure-of-merit (FOM) used to assess the suitability of a material or waveguide for nonlinear optics is the ratio of the imaginary part to the real part of the effective third-order susceptibility [20].

In the literature, this FOM takes many related forms, but here we choose to follow the convention FOM $= \gamma_I/\gamma_R = \lambda\alpha_2/(4\pi n_2)$. Here, as usual, α_2 is the two-photon absorption coefficient, n_2 is the Kerr refraction coefficient, λ is the wavelength of interest, and γ_R and γ_I are, respectively, the real and imaginary parts of the waveguide's nonlinear parameter given by $\gamma = (\frac{2\pi n_2}{\lambda} + i\frac{\alpha_2}{2})/A_{\text{eff}}$. Written in this form, we choose to refer to the figure-of-merit as the "nonlinear loss tangent"

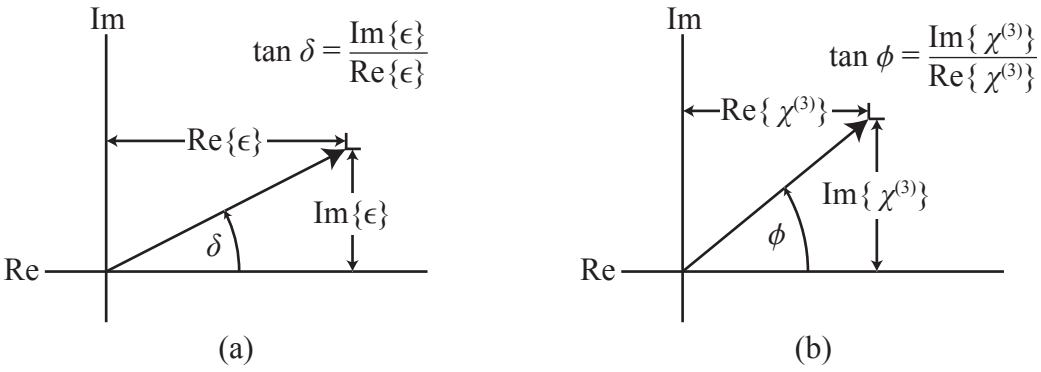

Figure 4.1: (a) A phasor diagram representing the (linear) loss tangent. (b) An analogous phasor diagram showing the nonlinear loss tangent.

because it is the nonlinear analog to the conventional (linear) loss tangent: the ratio of the imaginary to the real part of the permittivity of a dielectric medium. The analogy between the loss tangent and the nonlinear loss tangent is depicted in Fig. 4.1.

A variety of methods can be used to characterize the nonlinear properties of waveguides, including power-dependent spectral broadening (good examples include [84–86]), power-dependent nonlinear transmission (e.g., [87, 88]), four-wave mixing (e.g., [31, 89, 90]), and coherent pump-probe measurements (e.g., [91–93]). But, each of these experimental methods has its shortcomings. Spectral broadening experiments often ignore the effects of dispersion and/or nonlinear absorption in order to estimate n_2. Nonlinear transmission experiments are sensitive only to α_2. Measurements using short optical pulses often ignore effects associated with the pulse shape and repetition rate. Four-wave mixing measurements are only sensitive to the magnitude of $\chi^{(3)}$. To deduce the nonlinearity of the waveguide, all of

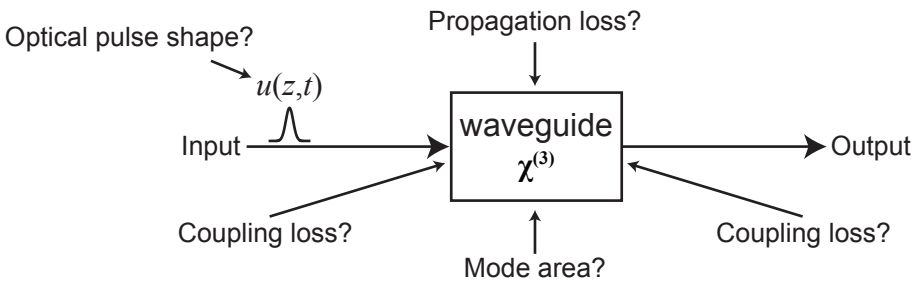

Figure 4.2: Factors which contribute error to the measurement of the nonlinear susceptibility.

these methods require precise *a priori* knowledge of the coupling losses, the mode area, and the propagation loss. (For example, Eq. (3.12) shows how all of these factors enter into the analysis of a nonlinear transmission experiment.) The error in these parameters compounds quickly, and in practice it is difficult to characterize the nonlinearity of a waveguide. Experiments to measure α_2 or n_2 are typically no more precise than $\pm 15\%$. The potential sources of experimental error are depicted in Fig. 4.2

This chapter presents a new method to characterize nonlinear refraction and loss in optical waveguides. It is a continuous-wave technique, and therefore does not suffer from uncertainty related to optical pulse-shapes or repetition rates. The technique directly probes the nonlinear loss tangent and is insensitive to coupling loss, propagation loss and the effective mode area. The method is applied to measure the nonlinear loss tangent of waveguides made from Si, GaAs and AlGaAs waveguides.

4.2 Description of the method

Figure 4.3 depicts the experiment used to measure the nonlinear loss tangent. A Mach-Zehnder modulator imparts a sinusoidal intensity modulation to a strong continuous-wave pump. The pump is combined with a weak continuous-wave probe, and the co-polarized beams are launched into the waveguide using a polarization-maintaining lensed fiber. The lensed fiber is positioned such that the pump and probe excite only one of the waveguide's fundamental polarization eigenstates, TE or TM. In the waveguide, the sinusoidal modulation of the pump is transferred to the probe via a combination of cross-phase and cross-amplitude modulation (XPM and XAM, respectively). Following the waveguide, an optical bandpass filter suppresses the pump and the probe passes through a spool of dispersive single-mode fiber. The dispersion of the fiber converts intensity modulation to phase modulation (and vice versa) in a manner that depends on the modulation frequency. The probe is

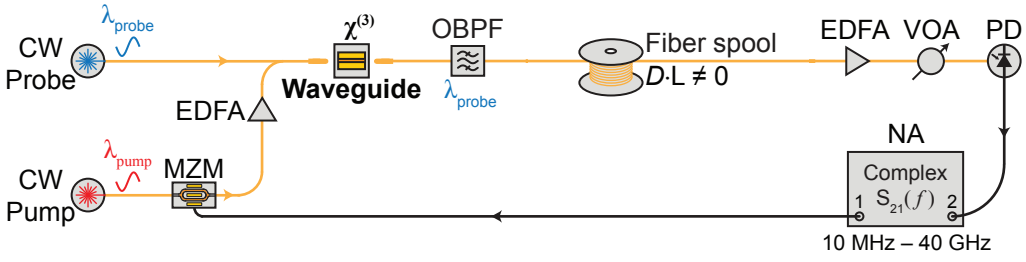

Figure 4.3: The experimental setup used to measure the nonlinear loss tangent. MZM: Mach-Zehnder modulator; EDFA: erbium-doped fiber amplifier; OBPF: optical bandpass filter; D·L: dispersion-length product of the fiber spool; VOA: variable optical attenuator; PD: high-speed photodiode; NA: network analyzer.

amplified by an erbium-doped fiber amplifier, then detected by a 65-GHz square-law photoreceiver. The photocurrent is received by a network analyzer, which sweeps the modulation frequency from 10 MHz to 40 GHz and records the system's complex $S_{21}(f)$ transfer function. The method is similar to that used by Devaux, et al., to measure the chirp parameter of intensity modulators [94], but here the modulations of interest are the XAM and XPM due to the waveguide's third-order susceptibility.

As derived in Appendix A, if the continuous-wave pump is constant in time (i.e., not intensity-modulated), then the complex amplitude of the probe emerging from a nonlinear waveguide of length l is given by Eq. (A.23b), which is reproduced here using slightly different notation to fit the current purpose:

$$u_2(l) = \frac{u_2(0)e^{-\alpha l/2}}{1 + 2\gamma_I P_{10} l_{\text{eff}}} \exp\left(i\frac{\gamma_R}{\gamma_I}\ln[1 + 2\gamma_I P_{10} l_{\text{eff}}]\right) \tag{4.1}$$

where P_{10} is the pump-power inserted into the waveguide, $u_2(0)$ is the complex amplitude of the probe inserted into the waveguide (normalized such that $|u_2(0)|^2 = P_{20}$), α is the propagation loss, $l_{\text{eff}} = (1 - e^{-\alpha l})/\alpha$ is the effective nonlinear length, l is the waveguide's physical length, and γ is the effective nonlinear parameter.

Small-signal analysis is now used to evaluate the effect of a sinusoidally modulated, time-varying pump. The pump entering the waveguide is assumed to take the form

$$P_1(t) = P_{10} + \Delta P \sin \Omega t, \tag{4.2}$$

where P_{10} is the average pump power, ΔP is the modulation amplitude, and Ω is the modulation frequency. The quantity $2\gamma_I P_{10} l_{\text{eff}}$ is assumed to be a small parameter, much less than unity, and the quantity $2\gamma_I \Delta P l_{\text{eff}}$ is necessarily even smaller. For the

experiments presented later, the ratio $\Delta P/P_{10}$ is typically 0.25 or smaller, depending on the RF power supplied to the Mach-Zehnder modulator. Inserting Eq. (4.2) into Eq. (4.1) and expanding the magnitude and phase of $u_2(l)$ to leading order, we obtain the following approximate expression for the time-varying probe signal emerging from the waveguide

$$u_2(t) = \sqrt{P_{20}} e^{-i\omega_0 t} \exp\left[i2\gamma l_{\text{eff}} \Delta P \sin \Omega t\right] \tag{4.3}$$

where ω_0 is the optical frequency and all the time-independent factors have been absorbed into $\sqrt{P_{20}}$. The fast-varying optical oscillation has been introduced in order to consider the dispersive effect of the fiber spool following the waveguide.

Using the Jacobi–Anger expansion, Eq. (4.3) can be expanded in a set of discrete spectral components:

$$u_2(t) = \sqrt{P_{20}} e^{-i\omega_0 t} \sum_{m=-\infty}^{\infty} J_m(z) e^{im\Omega t} \tag{4.4}$$

where $J_m(z)$ is the m^{th} Bessel function, and we have introduced the complex factor z to simplify the algebra

$$z \equiv 2(\gamma_R + i\gamma_I) l_{\text{eff}} \Delta P \tag{4.5}$$

In a dispersive fiber of length L, each spectral component ω of the signal acquires a phase shift of $\beta(\omega)L$, and the probe signal emerging from the spool of fiber is therefore

$$u_2'(t) = \sqrt{P_{20}} e^{-i\omega_0 t} \sum_{m=-\infty}^{\infty} J_m(z) e^{im\Omega t} e^{i\beta(\omega_0 - n\Omega)L} \tag{4.6}$$

The dispersion relation of the fiber is modeled by expanding to second order about

the probe's optical frequency

$$\beta(\omega) \approx \beta_0 + \beta_1(\omega - \omega_0) + \frac{\beta_2}{2}(\omega - \omega_0)^2 \tag{4.7}$$

Using Eq. (4.7) in Eq. (4.6), the probe signal emerging from the dispersive fiber is given by

$$u_2'(t) = \sqrt{P_{20}} e^{-i(\omega_0 t - \beta_0 L)} \sum_{m=-\infty}^{\infty} J_m(z) e^{im\Omega(t-\beta_1 L)} e^{im^2\beta_2\Omega^2 L/2} \tag{4.8}$$

Finally, shifting to the retarded time-frame $\tau \equiv t - \beta_1 L$, the probe signal simplifies to

$$u_2'(\tau) = \sqrt{P_{20}} e^{-i(\omega_0\tau + (\omega_0\beta_1 - \beta_0)L)} \sum_{m=-\infty}^{\infty} J_m(z) e^{im\Omega\tau} e^{im^2\beta_2\Omega^2 L/2} \tag{4.9}$$

At the receiver, the square-law photodetector with responsivity $\mathcal{R}$ produces a photocurrent of

$$i(\tau) = \mathcal{R}|u_2'(\tau)|^2 = \mathcal{R}P_{20} \sum_m \sum_n \left[J_m^*(z) J_n(z) e^{i(n-m)\Omega\tau} e^{i(n^2-m^2)\beta_2\Omega^2 L/2} \right] \tag{4.10}$$

This photocurrent is then detected by the network analyzer, which uses a homodyne detection method to mix the received signal with a sinusoidal signal at frequency Ω provided by its internal local oscillator (the same RF signal used to drive the Mach-Zehnder modulator at frequency Ω). The detection is therefore sensitive only to the AC components of Eq. (4.10) which oscillate sinusoidally at frequency Ω. To calculate these components, Eq. (4.10) is expanded in z to first order, and the terms that contribute are: $(m, n) = (0, 1); (0, -1); (1, 0)$ and $(-1, 0)$. After some algebra, the relevant components of the photocurrent reduce to

$$i(\tau) = -2\mathcal{R}P_{20}|z| \sin\left(\beta_2\Omega^2 L/2 + \phi\right) \sin\Omega\tau \tag{4.11}$$

Re-writing Eq. (4.11) in terms of the dispersion parameter D and the cyclic frequency f, an equivalent expression is

$$i(\tau) = 2\mathcal{R}P_{20}|z| \sin\left(\frac{\pi\lambda^2 DLf^2}{c} - \phi\right) \sin(2\pi f\tau) \tag{4.12}$$

where the dispersion parameter is given by $D = -2\pi c\beta_2/\lambda^2$. The factors $|z|$ and ϕ represent the magnitude and phase of the complex coefficient z. The phase ϕ is directly related to the nonlinear loss tangent of the waveguide through

$$\tan\phi = \frac{\gamma_I}{\gamma_R} = \frac{\lambda\alpha_2}{4\pi n_2} \tag{4.13}$$

Using the definitions given by Eqs. (2.55), an equivalent expression is

$$\tan\phi = \frac{\mathbf{Im}\{\chi^{(3)}_{\text{eff}}\}}{\mathbf{Re}\{\chi^{(3)}_{\text{eff}}\}} \tag{4.14}$$

4.3 Measurements of the nonlinear loss tangent

Figure 4.4(b) shows the measured frequency-dependence of the magnitude of the system's S_{21} transfer function for four different waveguides. The waveguide dimensions, compositions, propagation losses and calculated mode shapes are given in Fig. 4.4(a). According to Eq. (4.12), the amplitude of the received photocurrent will vanish at certain modulation frequencies, leading to nulls in the measured $S_{21}(f)$ trace. The data markers in Fig. 4.4(b) emphasize the positions of the nulls of each trace. A null occurs whenever the quantity $\pi\lambda^2 DLf^2/c - \phi$ is an integer-multiple of π. Therefore, the square of each null-frequency is given by

$$f_u^2 = \frac{c}{2DL\lambda^2}\Big(2u + \frac{2}{\pi}\phi\Big), \qquad u = 0, 1, 2... \tag{4.15}$$

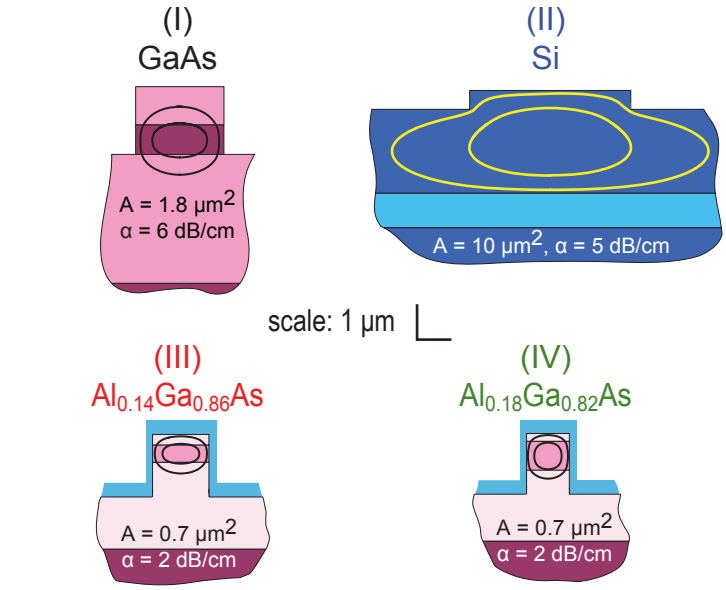

(a)

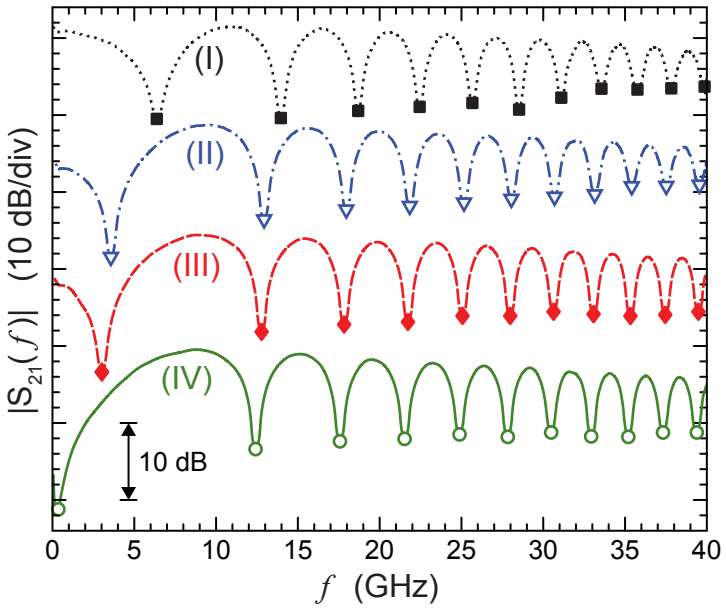

(b)

Figure 4.4: (a) Cross sections and mode properties of four waveguides. The contours indicate the −5- and −15-dB levels of the electric field for the TE eigenstate. (b) Representative $S_{21}(f)$ measurement for each waveguide (offset for clarity).

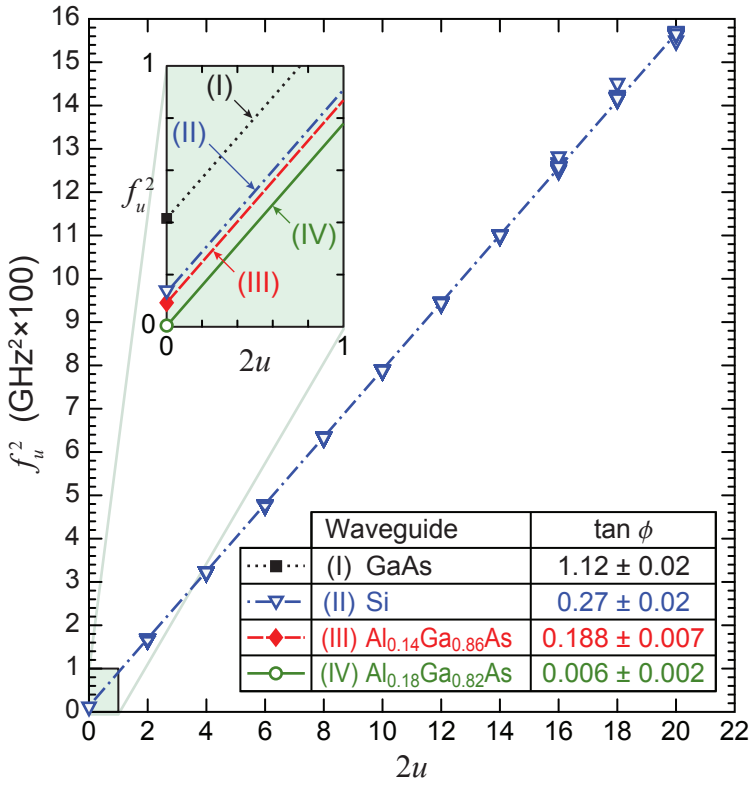

Figure 4.5: f_u^2 vs. $2u$ for the silicon waveguide (II) obtained from 30 consecutive $S_{21}(f)$ measurements. Inset: similar linear fits for all four waveguides considered, enlarged to show the difference in the intercepts. The table lists the nonlinear loss tangent of each waveguide, calculated using a linear regression of the null-frequencies, and the uncertainty is estimated using the 95% confidence bounds obtained from the least-squares fit.

By plotting f_u^2 as a function of $2u$, we obtain a line whose slope and intercept are related to the dispersion-length product of the fiber-spool and the phase ϕ, respectively.

Figure 4.5 plots f_u^2 vs. $2u$ for the silicon waveguide derived from 30 independently measured $S_{21}(f)$ traces. The data clearly demonstrate the linear behavior predicted by Eq. (4.15). The inset to Fig. 4.5 plots an enlarged region near the origin, with best-fit lines for all four of the waveguides considered. The key in the figure tabulates the value of the nonlinear loss tangent determined for each of the waveguides. The nonlinear loss tangents are calculated using a linear regression of the null-frequencies, and the uncertainties listed in the table reflect the 95% confidence bounds obtained from the least-squares fits.

Among the waveguides considered, the GaAs waveguide exhibits the highest nonlinear loss tangent of $\gamma_I/\gamma_R = 1.12 \pm 0.02$, followed by the silicon waveguide, which has $\gamma_I/\gamma_R = 0.27 \pm 0.02$. The remaining two waveguides were composed of $Al_xGa_{1-x}As$ alloys, where the bandgap increases with mole-fraction x. For $x = 0.14$, we obtained $\gamma_I/\gamma_R = 0.188 \pm 0.007$. When the aluminum fraction is increased to $x = 0.18$, the measured nonlinear loss tangent is $\gamma_I/\gamma_R = 0.006 \pm 0.002$, indicating that the nonlinearity becomes almost entirely refractive, as expected, when the bandgap exceeds twice the photon energy [59].

For the silicon waveguide (II), the optical mode is almost entirely contained within the silicon ridge, and we therefore expect the measured nonlinear loss tangent to closely match that of bulk silicon. The nonlinear refraction and two-photon-absorption coefficients of bulk silicon were independently measured by Ryan Suess,

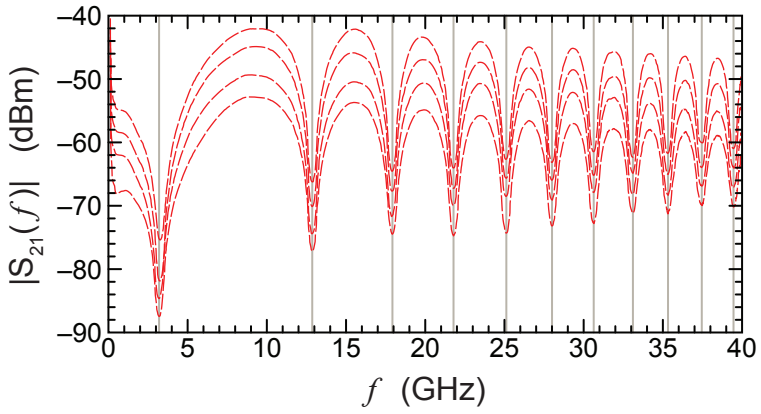

Figure 4.6: $S_{21}(f)$ measurements from the $Al_{0.14}Ga_{0.86}As$ waveguide, obtained by increasing the pump intensity in 3-dB steps.

a graduate-student researcher in the University of Maryland's Photonics Research Laboratory. Using a z-scan experiment with light polarized along the $\langle 110 \rangle$ direction of bulk silicon, he found $\tan\phi = \lambda_0 \alpha_2/(4\pi n_2) = 0.27 \pm 0.03$, in perfect agreement with the waveguide measurements reported here, and consistent with widely accepted values from the literature [21].

One advantage of the swept-frequency measurement presented in this chapter is that it does not require knowledge of the coupling efficiency into the waveguide, a key source of uncertainty in most nonlinear measurements. To illustrate this, Fig. 4.6 plots four independently measured $S_{21}(f)$ traces obtained by successively increasing the pump power in 3-dB increments. As predicted, the measured result scales, but the positions of the nulls remain unchanged.

4.4 Summary

A new method for measuring the nonlinear loss tangent of optical waveguides is presented. The technique uses a swept-frequency measurement of cross-amplitude and cross-phase modulation to circumvent the uncertainties associated with incomplete or inaccurate knowledge of the propagation loss, the optical power, the coupling efficiency, and the effective mode area. The technique uses quasi-continuous-wave light sources, and therefore does not suffer from uncertainty related to optical pulse-shapes or repetition rates.

A mathematical description of the technique is provided. The derivation is based upon a small-signal analysis of the solution to the coupled-wave equations that describe the interaction of the pump and probe in the nonlinear waveguide. The approach is an adaptation of that used by Devaux, et al., to measure the chirp of optical modulators [94].

Because bulk silicon is a well-studied nonlinear material, we use a large-area silicon waveguide as a benchmark test to verify the validity of the new technique. The measured nonlinear loss tangent of the silicon waveguide agrees perfectly with independent measurements made using other methods. The technique is also applied to measure the nonlinear loss tangents of a GaAs waveguide and two bandgap-engineered AlGaAs waveguides. The AlGaAs measurements show that by increasing the mole fraction x in the alloy to $x = 0.18$, two-photon absorption can effectively be eliminated in the telecommunications C-band.

Chapter 5: The non-instantaneous optical nonlinearity of a-Si:H

5.1 Overview

Hydrogenated amorphous silicon (a-Si:H) is a promising material for optical processing in integrated silicon photonics. Films of a-Si:H can be deposited at low temperatures (in the range of 250 to 400°C) using plasma-enhanced chemical vapor deposition (PECVD), which means the material is back-end-of-the-line compatible with standard CMOS fabrication techniques. This means that, in principle, a-Si:H photonic structures can readily integrate with silicon-on-insulator photonic and electronic circuits. And, as a deposit-able waveguide material, a-Si:H poses the intriguing possibility of easy on-chip vertical stacking and vertical coupling of nonlinear photonic components [95].

Given these attractive qualities, nonlinear photonics using a-Si:H is a very active field of research. Within the last few years, many groups have published studies of the nonlinear properties of a-Si:H waveguides [44, 49, 50, 91, 95–107], and an exciting array of applications has been demonstrated: ultrafast all-optical switching [100], wavelength conversion [50,101], correlated pair generation [102,106], supercontinuum generation [103], high-speed waveform sampling [97], ultrafast pulse characterization [104], on-chip net parametric gain [49,108] and wavelength-agile optical

parametric oscillation [105]. This list continues to grow rapidly.

Because a-Si:H has been reported to have a quasi-bandgap of ∼1.7 eV, which is larger than the two-photon energy at telecommunications wavelengths, it should exhibit small two-photon absorption compared to crystalline silicon (c-Si). However, in contrast to c-Si, the nonlinear characteristics of a given specimen of a-Si:H depend strongly on the fabrication conditions. Presumably, the extent of disorder in the amorphous silicon and the extent to which hydrogen atoms terminate dangling bonds impact the amount of nonlinear absorption, but a cause-and-effect relationship between fabrication conditions and the nonlinear traits of a-Si:H has yet to be established. Published values of the nonlinear loss tangent of a-Si:H waveguides span a broad range, including $\tan\phi = 0.2$ [91], 0.12 [96], 0.038 [49, 97], 0.026 [98], 0.016 [99], and 0.015 [44].

However, as defined, the nonlinear loss tangent only describes instantaneous nonlinear properties. Even with a small $\tan\phi$, a waveguide can possess a non-instantaneous nonlinearity that can significantly limit the efficiency of nonlinear signal processing. For example, in crystalline silicon, delayed free-carrier absorption severely impairs the performance of many nonlinear devices. Thus, understanding the nature of the non-instantaneous nonlinearity of a-Si:H is crucial to engineering future photonic devices from this promising material. On this topic, it is important to point out that in crystalline silicon devices, the effects of free carriers can at least be mitigated through the incorporation of p–n junctions [109]. At present, this degree of freedom has not been demonstrated for devices composed of hydrogenated amorphous silicon, a fact which further highlights the need to understand the non-

instantaneous nonlinearity of a-Si:H.

Unfortunately, reports of the delayed nonlinearity of a-Si:H vary considerably, and a generally accepted model to describe the non-instantaneous behavior has yet to emerge. Ikeda et al. published one of the first studies of the third-order nonlinearity in a-Si:H [40]. They performed side-by-side z-scan measurements on thin samples of non-hydrogenated amorphous silicon (a-Si), a-Si:H, c-Si and SiO_2. Noting that the closed-aperture z-scan for a-Si was inverted with respect to that for SiO_2, the authors concluded that the dominant nonlinearity in a-Si (and, by extension, a-Si:H) must be non-instantaneous refraction and absorption from a long-lived free-carrier plasma. Additionally, their open-aperture z-scan measurements showed that the a-Si and a-Si:H samples displayed very large nonlinear absorption in comparison to c-Si, despite having a larger bandgap. To explain the combination of enhanced nonlinear absorption and the presumed free-carrier refractive nonlinearity, the authors constructed a model in which free carriers were generated via "two-step" or "two-state" absorption (TSA). In the TSA model, they assumed that sequential one-photon absorptions, facilitated by mid-gap electronic states, generated free carriers at an enhanced rate relative to what might be expected from 2PA alone. However, other groups have disputed the applicability of the TSA model to describe their a-Si:H samples. For example, Narayanan and Preble [96] conducted measurements of the power-dependent transmission of short pulses through an a-Si:H waveguide, and they attributed the nonlinear transmission to a combination of 2PA and FCA, as in crystalline silicon. Likewise, Kuyken et al. [97] and Lacava et al. [98] relied on the 2PA+FCA model to explain their transient nonlinear absorption measurements.

One very thorough method for characterizing the non-instantaneous nonlinearity in a waveguide is the heterodyne pump-probe measurement. This time-resolved technique is simultaneously sensitive to the phase and amplitude of the probe, and can distinguish between cross-amplitude modulation (XAM) and cross-phase modulation (XPM). In the first heterodyne pump-probe measurements reported on an a-Si:H waveguide [91], both the amplitude and phase of the probe demonstrated a non-instantaneous response. The non-instantaneous phase change exhibited the same sign as the instantaneous Kerr effect, opposite to the phase shift expected for free-carrier dispersion. However, the observed transient was short-lived and weak, making it difficult to draw definite conclusions about the non-instantaneous nonlinearity of their waveguide. In contrast, in a more recent heterodyne pump-probe measurement of an a-Si:H waveguide [99], no delayed absorption or refraction were observed.

This chapter presents a study of the non-instantaneous nonlinearity of an a-Si:H nanowire waveguide using a variety of experimental techniques. The waveguide studied here is similar to the one presented in [50] and [105]. For comparison, the same experiments are conducted on a c-Si nanowire of comparable dimensions. The experiments include: (1) a modified version of the nonlinear loss tangent experiment described in Chap. 4; (2) a phase-insensitive transient absorption experiment using a continuous-wave probe and pulsed pump, similar to those in [97] and [98]; and (3) a two-frequency heterodyne pump-probe experiment described in [93].

Taken together, these experiments show that the a-Si:H waveguide demonstrates essentially zero instantaneous nonlinear absorption, but it does exhibit ap-

preciable non-instantaneous nonlinear absorption and refraction. Moreover, the delayed portion of the waveguide's pump-probe amplitude transient scales in direct proportion to the applied pump power, indicating the non-instantaneous nonlinearity is effectively a third-order nonlinearity rather than a combination of instantaneous two-photon absorption followed by free-carrier absorption. Finally, the phase-transient measurements show that the non-instantaneous nonlinear refraction has the same sign as the instantaneous Kerr refraction, which cannot be attributed to the dispersive effect of free carriers.

5.2 The a-Si:H and c-Si nanowire waveguides

Both the waveguides studied here were fabricated by Mr. Ke-Yao Wang, a graduate-student researcher in the Integrated Photonics Laboratory at Johns Hopkins University. The a-Si:H nanowire is fabricated by PECVD deposition of an a-Si:H film onto a silicon wafer, which has a 3-μm thermal oxide layer. In the a-Si:H film deposition chamber, a gas flow of 1200 sccm made up of helium with 5% silane is kept at a pressure of 900 mT with 50 W RF power. The substrate is maintained at approximately 300°C for low-temperature deposition. A layer of silicon dioxide is deposited as a hard mask to reduce effects from direct etching with organic resists. Electron beam lithography followed by chlorine-based inductively coupled plasma (ICP) etching is used to pattern the waveguide. Inverse adiabatic tapers are patterned on both ends of the waveguide to facilitate optical coupling [110].[1] The

[1]Because the core layer is very thin in the vertical dimension, using a flare-structure in this case would lead to a horizontally elongated mode at the facet, which would be detrimental to coupling.

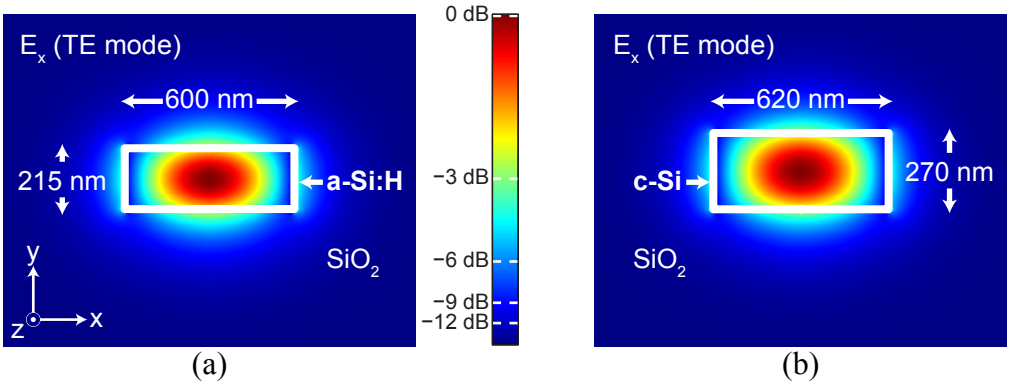

Figure 5.1: False-color images of the calculated mode for (a) the a-Si:H nanowire and (b) the c-Si nanowire. The images show the magnitude of the x-component of the electric field for the TE eigenstate.

a-Si:H core layer is 215 nm thick and 600 nm wide. A 1-μm-thick SiO_2 layer is deposited over the waveguide via PECVD for an optical cladding. The c-Si waveguide is fabricated on a SOI (silicon-on-insulator) platform with a 3-μm buried oxide. The same patterning techniques are used and the c-Si waveguide has similar dimensions: 270 nm thick and 620 nm wide, with a 1-μm SiO_2 cladding.

In all the experiments presented here, only the TE eigenmode of the waveguide is excited. The calculated TE eigenmodes are shown in Fig. 5.1 with overlays to indicate the cross-sectional composition of each waveguide. Both nanowire waveguides are 1 cm long and have a linear loss of approximately 3 dB/cm, measured using the cutback technique (for a description of this technique, see e.g., [111]). The two waveguides have slightly different cross-sectional dimensions and the propagation losses are not quite state-of-the-art [33, 45], but these factors should not affect the overall characteristics of the non-instantaneous nonlinearities, which are compared in the following analysis.

5.3 Nonlinear loss tangent measurements

The measurements presented in this section were made using variants of the nonlinear-loss-tangent technique described in Chap. 4. The experimental setup is depicted in Fig. 5.2. The operation of the experiment is identical to that described in Sect. 4.2, except experiments are performed with and without the spool of dispersive fiber installed in the setup. The fiber-to-waveguide coupling is estimated to be −8 dB for the c-Si and a-Si:H waveguides, and in both cases approximately 25 mW of pump power and 1 mW of probe power are launched into the waveguide.

The experiments conducted without the spool of fiber installed in the setup are considered first. In this configuration, the measurement characterizes the cross-amplitude modulation as a function of modulation frequency. As shown in the blue traces of Fig. 5.3(a), the crystalline silicon waveguide shows 10 dB higher cross-amplitude modulation at frequencies below approximately 50 MHz, but reaches a

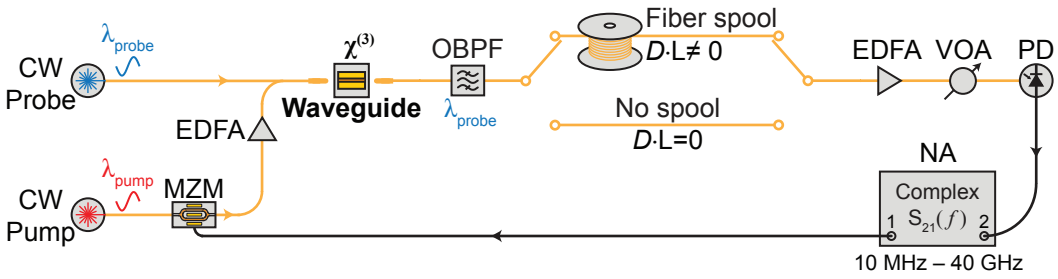

Figure 5.2: The experimental setup used to measure the nonlinear properties of the nanowires. The setup is shown with and without an optional spool of dispersive fiber. CW: continuous-wave; EDFA: erbium-doped fiber amplifier; MZM: Mach-Zehnder modulator; OBPF: optical band-pass filter; VOA: variable optical attenuator; PD: high-speed photodiode.

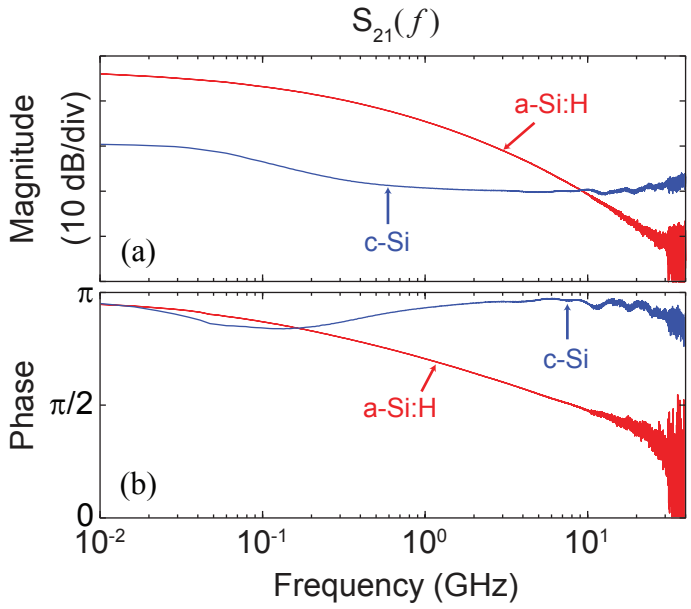

Figure 5.3: (a) Magnitude and (b) phase of S_{21} vs. the modulation frequency for the case with no dispersive fiber in the setup. Red traces represent the a-Si:H nanowire while blue traces represent the c-Si nanowire.

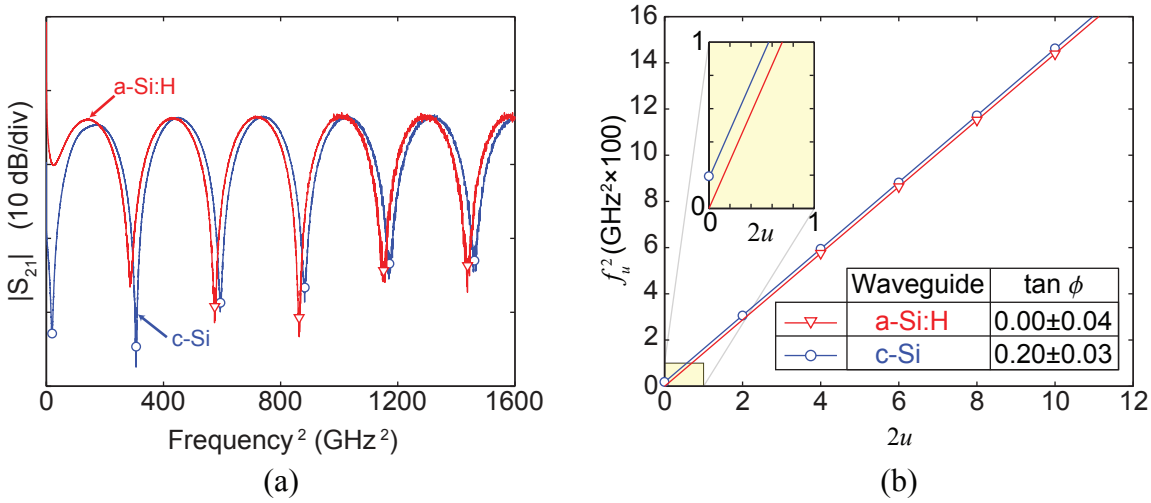

Figure 5.4: (a) The magnitude of S_{21} vs. the square of the modulation frequency with dispersive fiber in the setup. (b) f_u^2 vs. $2u$ for both waveguides obtained from 10 consecutive $S_{21}(f)$ measurements. Inset: The same linear fits for both waveguides, enlarged to show the difference in the intercepts.

plateau at higher frequencies. Apart from a small dip near this corner frequency, the phase of the $S_{21}(f)$ measurement, shown in Fig. 5.3(b), asymptotically approaches π in both the high and low frequency limits. The phase of $S_{21}(f)$ (which should not be confused with the optical phase of the probe wave) is an indication that the nonlinearity is absorptive: when the pump is stronger, the probe signal becomes absorbed, thereby causing their envelopes to be exactly π out of phase with one another. The higher XAM observed at low modulation frequencies is caused by free carrier absorption in the c-Si waveguide. The -3-dB roll-off point in this curve falls at approximately $f_c = 85$ MHz, which corresponds to an estimated free-carrier lifetime of $1/(2\pi f_c) = 1.9$ ns, in good agreement with other reports for similarly sized c-Si waveguides [92]. The high-frequency plateau in the XAM spectrum is well explained by non-degenerate two-photon absorption between the pump and probe – an instantaneous absorptive nonlinear effect that occurs across all modulation frequencies. In Appendix B, the theory of free carriers is employed to model the c-Si behavior observed in Figs. 5.3(a) and 5.3(b).

In contrast, for the a-Si:H waveguide, the magnitude of $S_{21}(f)$ falls monotonically with the modulation frequency, similar to the behavior of a low-pass filter. Although it was not possible to measure the asymptotic phase response beyond 40 GHz, the phase undergoes a net shift of $-\pi/2$ over the frequency range observed, again suggesting a low-pass response. In the limit of low modulation frequency, the a-Si:H waveguide exhibits significantly stronger XAM than its c-Si counterpart. Yet, the absence of a high-frequency plateau in the magnitude measurement indicates that instantaneous two-photon absorption is absent or negligible for a-Si:H.

Because of the apparent absence of two-photon absorption, the slower nonlinearity cannot be adequately described by free carrier absorption, as was the case for the c-Si. The −3-dB roll-off point in this curve falls at approximately $f_c = 105$ MHz, which corresponds to an estimated lifetime of $1/(2\pi f_c) = 1.5$ ns. It is important to note that the optical powers launched into the c-Si and a-Si:H waveguides were similar (about 25 mW of pump power in both cases), and the delayed nonlinear absorption of the a-Si:H is a strong effect.

The same measurements were then repeated with a 25-km spool of SMF fiber installed after the device, which permits measurement of the ratio of XAM to XPM, as detailed in Chap. 4. Provided this ratio is independent of the modulation frequency, one can determine the nonlinear loss tangent by linear regression to find the intercept point of Eq. (4.15), as shown in Figs. 5.4(a) and 5.4(b). For the a-Si:H waveguide, the non-instantaneous nonlinearity shifts and obscures the two lowest-order nulls ($u = 0$ and 1). But, based on the data of Fig. 5.3(a), the magnitude of the non-instantaneous component to the nonlinearity can be safely ignored for modulation frequencies above 20 GHz. Therefore, the first two nulls are excluded in order to apply Eq. (4.15), which was derived under the assumption of a purely instantaneous nonlinearity. This permits an estimate of the instantaneous nonlinear loss tangent by considering only the high-frequency asymptotic behavior. Figure 5.4(b) shows a fit of the null-frequencies for $u = 2$ through 5 to a straight line to obtain the slope and intercept of Eq. (4.15). The fit yields $\tan\phi = 0.00 \pm 0.04$, which confirms the absence of instantaneous nonlinear absorption in the a-Si:H waveguide.

For c-Si, the non-instantaneous nonlinear absorption is relatively insignificant

compared to the instantaneous effects, so all of the nulls ($u = 0$ through 5) are included in the fitting procedure. The linear regression yields $\tan\phi = 0.20 \pm 0.03$, which is in good agreement with the nonlinear loss tangent expected for bulk c-Si (which, as stated in Chap. 4, is 0.27±0.03). A slight reduction from the bulk-value is expected since a significant portion of the optical mode samples the SiO_2 cladding in this nanowire waveguide.

5.4 Transient absorption using a continuous-wave probe

The experimental setup used to measure transient absorption in the nanowires is depicted in Fig. 5.5. A passively mode-locked fiber laser produces hyperbolic-secant-squared pump pulses with a pulse-width of 2 ps. The repetition rate of the pump laser is 10 MHz, and the center-wavelength is 1530 nm. A separate external-cavity laser produces the continuous-wave probe at 1560 nm. The co-polarized pump

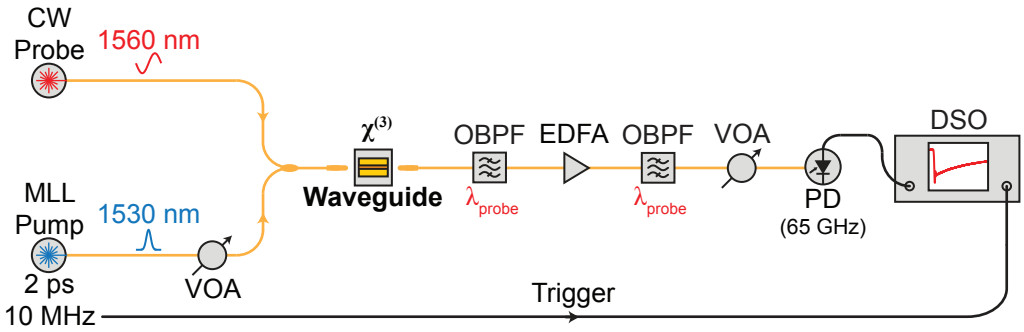

Figure 5.5: The experimental setup used to measure transient nonlinear absorption in the nanowires. MLL: mode-locked fiber laser; CW: continuous-wave; VOA: variable optical attenuator; OBPF: optical band-pass filter; EDFA: erbium-doped fiber amplifier; PD: high-speed photodiode; DSO: digital sampling oscilloscope.

and probe are combined and launched into the TE eigenstate of the waveguide using a polarization-maintaining lensed fiber. The fiber-to-waveguide coupling loss for both waveguides is about 8 dB. For all the experiments presented in this section, the probe power coupled into the waveguide is 1 mW, and the power of the pump is adjusted using a variable optical attenuator to observe the scaling of the transient absorption with pump power. The highest achievable peak power of the pump pulses is about 8.4 W in the input lensed fiber, or about 1.3 W of peak power into the waveguide. At the output of the waveguide, the pump is suppressed using optical bandpass filters and the probe is amplified by an erbium-doped fiber amplifier. The probe is detected using a 65-GHz photodiode, and the transient absorption response is recorded on a 30-GHz digital sampling oscilloscope.

The transient absorption data for the a-Si:H and c-Si waveguides are shown in Figs. 5.6(a) and 5.6(b), respectively. Data was collected over a time-window of 100 ns (the full inter-pulse interval). However, to emphasize the scaling of the transients close to $t = 0$, Figs. 5.6(a) and 5.6(b) only show the data through $t = 400$ ps. The top axes in Figs. 5.6(a) and 5.6(b) show the transient absorption of the probe for four pump powers, where the pump power has been incremented in 3-dB steps. The transients are normalized to their average value prior to the arrival of the pump (i.e., $P(t)/P_0$). The bottom axes show the same data, but the normalized $P(t)$ has been subtracted from 1 (i.e., fractional absorption $= 1 - P(t)/P_0$). The fractional absorption data are plotted in dBr, decibels relative to the extremum in the transient for the highest pump power. Graphing the data in this manner makes clear the scaling of the transients as a function of pump power. In these traces,

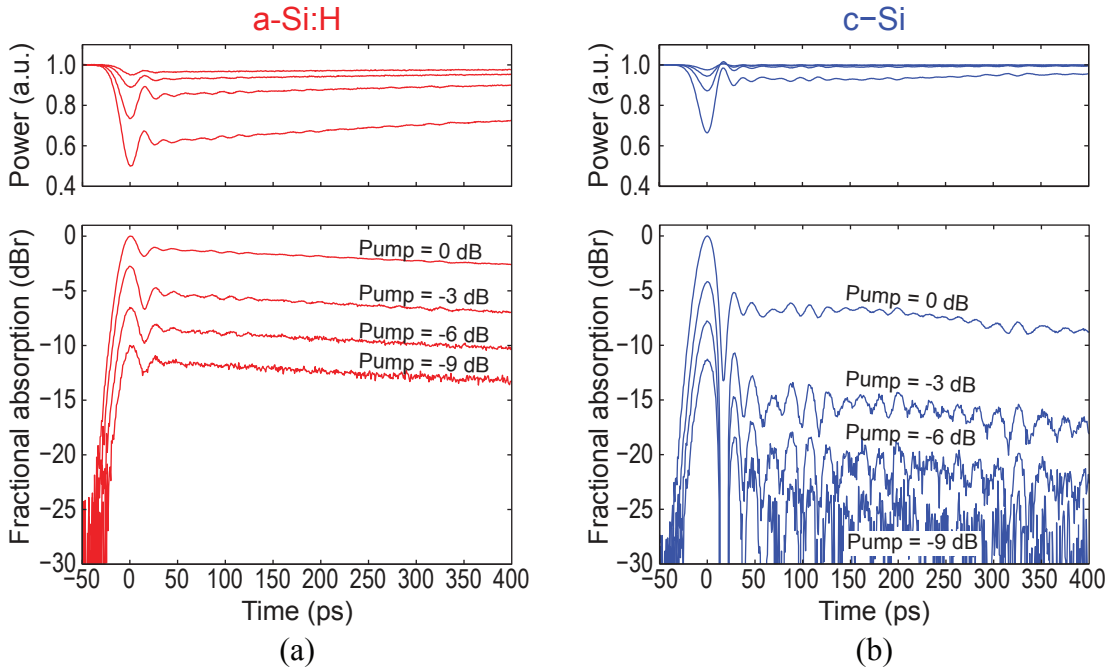

Figure 5.6: Transient absorption of the probe for (a) the a-Si:H nanowire and (b) the c-Si nanowire. Top: normalized probe power vs. time. Bottom: Fractional absorption of the probe vs. time. Zero time-delay is registered to the extremum in each transient and positive time indicates time since the extremum.

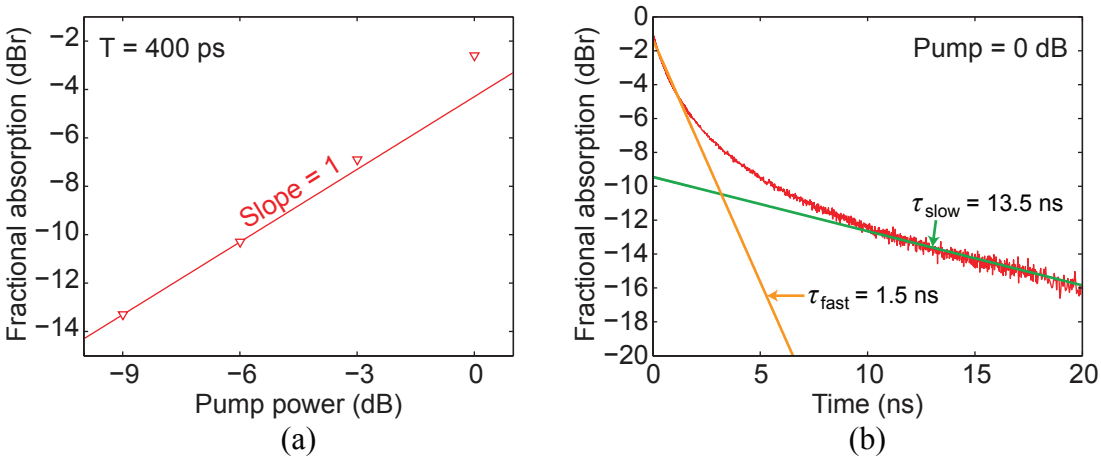

Figure 5.7: (a) Fractional absorption of the probe versus the applied pump power for the a-Si:H waveguide. The solid red line is a guide for the eye, not a fit-line. (b) Transient absorption of the probe (the same as the highest-power trace in Fig. 5.6(a), but the scale is adjusted to show a longer interval).

the abrupt recovery at about $t = 25$ ps and the fast ripples afterward are caused by the impulse response of the detector, which has not been deconvolved from the experimental results.

For the c-Si nanowire, the instantaneous part of the transient occurring at $t = 0$ is distinct from the non-instantaneous recovery, and scales in direct proportion to the pump power, as expected for non-degenerate two-photon absorption. On the other hand, the long-lived, non-instantaneous portion of the transient scales approximately with the square of the pump power (i.e., the transient response increases in roughly 6-dB increments each time the pump increases by 3 dB). This scaling behavior is well-explained by free-carrier absorption, wherein the free carrier population is created by degenerate 2PA of the pump pulses and therefore scales in proportion to P_{pump}^2 [23]. The observed $1/e$ lifetime of the c-Si transient (excluding the instantaneous portion) is approximately 2 ns, which roughly agrees with the $S_{21}(f)$ measurements presented in Fig. 5.3(a).

In contrast to the c-Si result, the a-Si:H nanowire exhibits a very different scaling relationship: The entire transient response is observed to scale roughly in direct proportion to the pump power (i.e., the transient response increases in 3-dB increments as the pump power is increased by 3 dB), with no clear separation between the instantaneous and non-instantaneous components. This power-scaling is illustrated in Fig. 5.7(a), which shows the fractional absorption versus the applied power for a fixed time-delay of 400 ps. Figure 5.7(b) shows the fractional absorption data for the highest pump power over a larger time interval of 20 ns. While the time-dependent fractional absorption cannot be described by a simple mono-exponential

function, it can be divided into two regions, one dominated by a fast exponential decay (with $\tau_{\text{fast}} = 1.5$ ns) and the other by a slow exponential decay (with $\tau_{\text{slow}} = 13.5$ ns). The observed $1/e$ response time of the a-Si:H is 1.5 ns, which agrees with the $S_{21}(f)$ measurements presented in Fig. 5.3(a). However, that the transients scale linearly with pump power indicates that the non-instantaneous response cannot be attributed to free-carrier effects. A better description of the nonlinear response would be through another third-order-nonlinearity effect, perhaps related to mid-gap states or other intermediate electronic states with nanosecond lifetimes.

5.5 Heterodyne pump-probe measurements

The transient absorption measurements described in the preceding section only characterize the cross-absorption modulation between the pump and probe. To characterize the phase response as well, a two-frequency heterodyne pump-probe setup was employed, depicted in Fig. 5.8. This setup was built by Mr. Ryan Suess and Mr. Mehdi Jadidi, graduate researchers in the Photonics Research Laboratory of the University of Maryland. A thorough explanation of the experimental technique is given in [93].

The pump and probe pulses are produced by two electronically synchronized mode-locked fiber lasers (Menlo Systems). The pulses emitted by both lasers have a central wavelength of 1560 nm and pulse-width of 100 fs. The first laser generates only the pump pulses, while the output of the second laser is split evenly to provide the reference and probe pulses, which precede and succeed the pump pulse, respec-

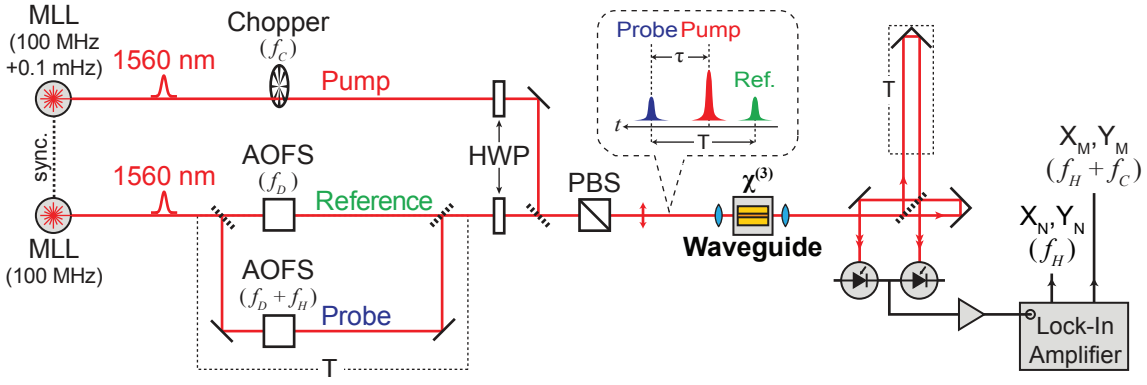

Figure 5.8: The two-frequency heterodyne pump-probe experiment. The inset shows the relative timing of the reference, pump and probe pulses. MLL: mode-locked laser; AOFS: acousto-optic frequency shifter; HWP: half waveplate; PBS: polarizing beam splitter.

tively. The time-offset between the probe and reference pulses is fixed at $T = 830$ ps. The repetition rate of the probe/reference laser was fixed at 100 MHz, while the pump laser was adjusted to a rate of 100 MHz + 0.1 mHz, which causes the time delay between the pump and probe pulses to continuously sweep at a rate of 1 ps/s.

Acousto-optic frequency shifters (AOFS) introduce a blue-shift to the probe and reference pulses. The reference pulses are up-shifted by $f_D = 35$ MHz while the probe pulses are up-shifted by $f_D + f_H = 35.0625$ MHz (f_D denotes the resonant drive frequency of the AOFS). The detection ultimately relies on measuring the heterodyne beat between the probe and reference, which has a frequency $f_H = 62.5$ kHz. The pump beam is mechanically chopped at $f_C = 1$ kHz. For a given pump-probe delay, τ, chopping the pump allows comparison of phase and amplitude of the probe with the pump on (when the chopper wheel allows the pump to pass) relative to the phase and amplitude of the probe with the pump off (when the chopper blade occludes the pump).

The probe/reference and pump beams pass through separate half waveplates (used to adjust the power in each beam), and the beams are combined using a beam splitter. A polarizing beam splitter prior to the coupling optics passes only the horizontal component of the electric field, in order to excite only the TE eigenstate of the waveguide. Because the optical pulse-width is roughly 100 fs, free-space optics are used to couple light into and out of the waveguide (for a pulse-width this short, the dispersion introduced by even a short segment of optical fiber would substantially change the pulse shape). A high-numerical-aperture aspheric lens (60×, N.A.= 0.65) launches the light into the waveguide. In the waveguide, XAM and XPM modify

the amplitude and phase of the probe as a function of the pump-probe delay. At the output of the waveguide, the light is collimated by a microscope objective, and directed into a Michelson interferometer, which realigns the probe and reference pulses in time. The two complementary outputs from the interferometer are recorded using a balanced detector, which suppresses the common mode noise of the pump. A dual-phase lock-in amplifier simultaneously detects both quadratures at both the heterodyne frequency, f_H, and at the first upper sideband of the heterodyne frequency, $f_H + f_C$. From these two measurements, one can calculate the cross-phase modulation $\Delta\phi$ as the time delay τ is swept [93].

Figure 5.9 compares the phase transients for the a-Si:H and c-Si waveguides. The unphysical leading edge in the a-Si:H transient can be attributed to a difference between the pulse-shapes used in the two experiments. For the a-Si:H experiment, the average probe power launched into the waveguide is estimated to be 0.3 μW while the average launched pump power is 264 μW. For the c-Si experiment, the average probe power launched into the waveguide is estimated to be 0.46 μW, while the average launched pump power is 431 μW.

The heterodyne measurements shown in Fig. 5.9 reveal that the delayed amplitude transient observed during the transient absorption experiments is accompanied by a corresponding non-instantaneous phase transient for both waveguides. The phase transient recorded for the c-Si nanowire agrees well with previously published results [92]. However, the a-Si:H waveguide is seen to behave dramatically differently from the c-Si waveguide: The non-instantaneous phase transient is positive (indicating a non-instantaneous pump-induced increase in refractive index), while

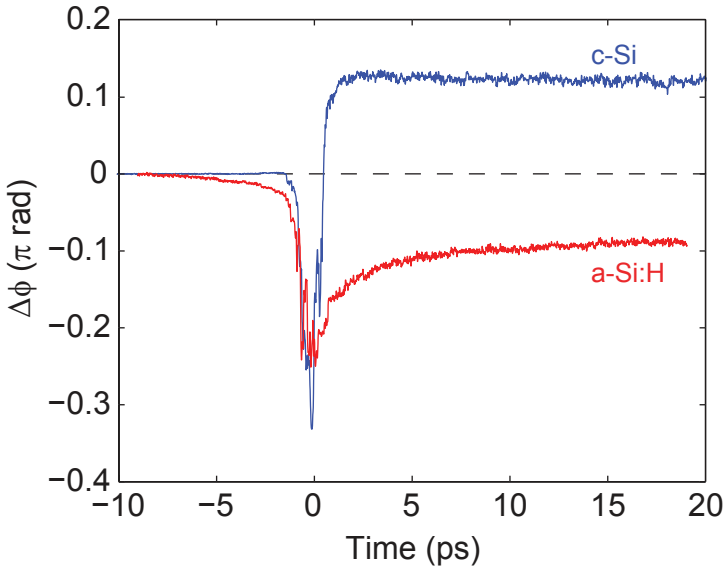

Figure 5.9: Time-resolved phase transients for the a-Si:H (red) and c-Si (blue) nanowires. In these experiments, the launched pump powers were 264 μW and 431 μW, respectively.

for c-Si it is negative, as expected for free-carrier dispersion. This result, which confirms earlier reports from Shoji et al. [91], provides further evidence that the non-instantaneous nonlinearity of a-Si:H is not attributable to free carriers.

5.6 Discussion

Taken together, these measurements thoroughly characterize the non-instantaneous nonlinear response of this a-Si:H nanowire. Though the results do not indicate the precise microscopic origin of the delayed nonlinear response, several features emerge that are different from what is commonly observed in crystalline silicon.

First, this a-Si:H waveguide does not exhibit instantaneous two-photon absorption; this fact alone indicates free carriers are not responsible for the non-instantaneous component of the nonlinearity. The absence of instantaneous two-photon absorption is consistent with at least one earlier study of a-Si:H [107], but at odds with most previous reports [44, 91, 96–99]. On this point, it bears repetition that the optical properties of a-Si:H depend on how it is deposited and processed. Fabrication-dependence of the instantaneous nonlinear absorption could explain the variety of nonlinear-absorption characteristics reported in the literature.

Second, this a-Si:H nanowire shows a significant non-instantaneous amplitude and phase response, with a characteristic lifetime of $\sim$1.5 ns. The delayed phase shift is clearly positive, in the same direction as the instantaneous Kerr phase shift, which contradicts what is commonly observed for free-carrier dispersion. We know of one previous publication in which a similar result was documented for an a-Si:H

waveguide [91]. But, in that report the effect was much weaker, and the authors attributed it to carriers.

Third, the magnitude of the cross-absorption transient is observed to scale in proportion to $P_{\text{pump}}P_{\text{probe}}$. This fact, together with the sign of the non-instantaneous nonlinear phase shift and the absence of two-photon absorption, means the non-instantaneous nonlinearity cannot be attributed to free carrier effects. The observed power-scaling of the absorption transient is similar to that predicted by the two-state-absorption model (with the instantaneous two-photon absorption coefficient set to zero) proposed by Ikeda, et al [40]. However, the two-state-absorption model attributes the delayed response to free-carrier absorption and dispersion, which is not commensurate with the results observed here.

Phenomenologically, the observed response is best described as instantaneous intensity-dependent nonlinear refraction coupled with delayed intensity-dependent nonlinear absorption and refraction. The sign of the nonlinear refraction is positive for the instantaneous and non-instantaneous components. Without further information, we refrain from assigning a particular physical mechanism(s) to the observed phenomena.

Despite the non-instantaneous nonlinearity, a-Si:H remains very promising for integrated nonlinear photonics, especially pulsed applications where only a fraction of the delayed absorption is sampled by the field. Understanding the dependence of the nonlinearity of a-Si:H on the conditions of the deposition is an important research goal and it is left as future work to perform linear spectroscopy of a-Si:H films deposited under various conditions. Doing so, we hope to gain insight into the

microscopic origins of the nonlinearity in this material and identify paths towards the mitigation of nonlinear losses.

5.7 Summary

This section presents the results of a range of both quasi-continuous-wave and pulsed measurements of the non-instantaneous nonlinear response of an amorphous hydrogenated silicon waveguide. The response of the amorphous hydrogenated silicon waveguide is compared to that of a crystalline silicon waveguide having comparable dimensions.

Quasi-continuous-wave cross-phase and cross-amplitude modulation measurements reveal that both materials exhibit nanosecond-scale phase and amplitude nonlinearities. However at sufficiently high modulation frequencies, the a-Si:H waveguide shows a purely refractive nonlinearity, signifying the absence of instantaneous two-photon absorption. Transient absorption measurements and heterodyne pump-probe measurements are presented. In all cases, the observations of the delayed response of a-Si:H are seen to be inconsistent with an interpretation as free-carrier effects.

These results show that the nature of and origin of the non-instantaneous nonlinearity in amorphous-hydrogenated silicon is more complex than is ordinarily assumed for crystalline silicon waveguides, and that existing models for the nonlinearity must be re-examined before conclusions can be drawn about the suitability and merits of this material for nonlinear optical processing.

Chapter 6: Conclusions and future work

This dissertation documents research of nonlinear waveguides, with the intent to determine their suitability for all-optical processing. The research consists mainly of measurements of the nonlinear properties of AlGaAs and hydrogenated amorphous silicon waveguides, two material platforms which are potentially better for all-optical processing than crystalline silicon. To build a complete understanding of the waveguides, several types of experiments are performed on both systems, and the nonlinear properties are measured using quasi-continuous-wave lasers and pulsed lasers. Additionally, a new continuous-wave technique is developed and applied to measure the ratio of nonlinear loss to nonlinear refraction in waveguides.

The explorations of the AlGaAs waveguides focus on wavelength conversion via continuous-wave four-wave mixing. The core-bandgaps of the waveguides are engineered to suppress two-photon absorption, which is confirmed by measuring the power-dependent nonlinear transmission and spectral-broadening of the waveguides. The fabrication of the waveguides is controlled to achieve low propagation loss and near-zero group-velocity dispersion. The resulting combination of waveguide-characteristics leads to enhancement of the bandwidth and efficiency of continuous-wave four-wave mixing. The observed continuous-wave conversion efficiencies are or-

ders of magnitude better than those of any previously reported AlGaAs waveguides, and comparable to those achieved in any passive semiconductor or glass waveguides.

A new continuous-wave technique to measure the nonlinear loss tangent is described. The technique employs a swept-frequency measurement of the ratio of cross-amplitude to cross-phase modulation. The result is a direct probe of the nonlinear loss tangent, which circumvents the uncertainties associated with incomplete or inaccurate knowledge of the propagation loss, the pulse-shape, the optical power, the coupling efficiency, and/or the effective mode area. The method is applied to measure the nonlinear loss tangent of a GaAs waveguide, two bandgap-engineered AlGaAs waveguides, a large-area crystalline silicon waveguide, a crystalline silicon nanowire waveguide, and a hydrogenated amorphous silicon nanowire waveguide. In Chap. 4, the technique is applied to characterize only instantaneous nonlinearities. But, Chap. 5 describes how the method can be extended to characterize non-instantaneous, frequency-dependent nonlinearities, too.

A detailed study of an amorphous-hydrogenated silicon waveguide is presented, and its nonlinear response is compared to that of a similarly sized crystalline silicon nanowire. The hydrogenated amorphous silicon waveguide is observed to exhibit an instantaneous refractive nonlinearity without any instantaneous nonlinear absorption. However, it also exhibits a nanosecond-timescale non-instantaneous nonlinearity which is both absorptive and refractive. The measurements show that the delayed nonlinearity of the amorphous-hydrogenated silicon is inconsistent with an interpretation as free-carrier effects, and the origin of the non-instantaneous nonlinearity is more complex than is ordinarily assumed for crystalline silicon waveguides.

Existing models for the nonlinearity of amorphous-hydrogenated silicon must be re-examined before conclusions can be drawn about its suitability and merits for nonlinear optical processing.

6.1 Future work

6.1.1 AlGaAs waveguides

Looking forward, one clear near-term objective for the AlGaAs-waveguide project is to fabricate a waveguide capable of net parametric gain. Four-wave-mixing-based parametric gain has been demonstrated in nearly every competing chip-compatible waveguide-system (e.g., see [35] for crystalline silicon, [46, 47] for silicon nitride, [48] for Hydex, [49,108] for hydrogenated amorphous silicon, and [55] for a chalcogenide optical chip). The results of Chap. 3 show that we are tantalizingly close to being able to fabricate an anomalous-dispersion AlGaAs waveguide with sufficiently low propagation loss to achieve this milestone: Only a modest reduction in the waveguide-width is necessary. It is important to note that for the competing material systems just mentioned, it has only been possible to achieve parametric gain by harnessing the high peak power of short optical pulses, or by building the waveguide into a ring-resonator configuration. We have already demonstrated that it is possible to fabricate AlGaAs waveguides which exhibit negligible nonlinear absorption, high nonlinearity, sub-dB/cm propagation loss and high average-power tolerance. If we can push the fabrication limits to produce an anomalous-dispersion bandgap-engineered AlGaAs waveguide with sub-dB/cm propagation loss, preliminary sim-

ulations show that it may be possible to demonstrate *continuous-wave*, single-pass net parametric gain. Such a demonstration would be a substantial accomplishment for chip-based all-optical processing, and would make AlGaAs waveguides unique among the competing chip-based waveguides.

In the longer term, another path forward for the AlGaAs-waveguide project is to develop chip-based waveguides for second-order nonlinear processes. Among the competing material systems which are appropriate for integrated photonics, III-V semiconductors stand alone as being non-centrosymmetric. This property means that, in addition to being a good $\chi^{(3)}$-material, bulk AlGaAs also exhibits a large $\chi^{(2)}$, which makes it an excellent candidate for second-order processes such as sum- and difference-frequency generation and second-harmonic generation. These processes are especially useful for wavelength-converting signals over very large spectral distances, and could substantially increase the wavelength-agility of chip-based light sources. Therefore it would be highly desirable to develop chip-based AlGaAs waveguides for efficient second-order nonlinear photonics. In this context, it is unfortunate that AlGaAs is isotropic (thus non-birefringent). The chief difficulty to implement efficient second-order processes in AlGaAs waveguides is therefore to achieve phase-matching of the nonlinear interaction (phase-matching of second order processes in bulk materials usually relies on birefringence phase-matching). Nonetheless, a great deal of research has already focused on using AlGaAs and other III-V crystals for chip-based second-order photonics (for example, see Refs. [112–116]). By combining our ability to fabricate low-loss AlGaAs waveguides with novel cross-sectional designs to achieve form birefringence, we may be able to achieve significant future gains

in the efficiency and bandwidth of second-order integrated nonlinear photonics.

6.1.2 Hydrogenated amorphous silicon waveguides

Despite the fact that we have observed non-instantaneous nonlinear absorption in amorphous-hydrogenated silicon, it remains an extremely promising and important material for integrated nonlinear photonics. As a deposit-able, CMOS-compatible, highly nonlinear material, it has real potential to revolutionize integrated nonlinear silicon photonics. The ability to deposit low-loss nonlinear a-Si:H waveguides points to the possibility of building three-dimensional, vertically integrated nonlinear photonic structures, which could eliminate some of the geometrical problems associated with routing signals in planar integrated photonic circuits.

The observations of our experimental work to date have been inconclusive as to the physical mechanisms which generate the delayed nonlinearity of a-Si:H. The immediate goal is therefore to design experiments which allow direct observations of these physical mechanisms, and subsequently to build a physical model for the system akin to the two-photon-absorption/free-carrier-absorption model typically used to understand the nonlinear dynamics of crystalline silicon. This goal is complicated by the fact that the physics of this amorphous material depends on the conditions used to deposit it.

Moving forward, the first step should be to perform absorption spectroscopy of the possible mid-gap states of a-Si:H. Experiments should be conducted on a range of samples fabricated under various conditions, to determine how the formation of

mid-gap states depends on the fabrication. By building a complete picture of the states available to the system, we hope to construct a physical model to explain the nonlinearity of the material, which may help to identify paths towards mitigating the delayed nonlinearity by appropriately tailoring the deposition and fabrication.

Absorption spectroscopy is very simple in principle. But in practice, it will likely be difficult to obtain meaningful results. High-quality amorphous silicon can only be deposited in relatively thin films and must be deposited on a substrate. Therefore the interaction length of the optical absorption in the thin film will obviously be small, and the signal-to-noise ratio in the absorption spectrum will be correspondingly small. Additionally, the influence of the substrate will need to be subtracted from the experimental observations to isolate the absorption spectrum of the hydrogenated-amorphous silicon. Nonetheless, these experiments will be key to building a complete understanding of the nonlinear dynamics of hydrogenated-amorphous silicon.

Appendix A: Approximate solutions to the coupled-wave equations

This Appendix provides analytical solutions to Eqs. (2.65a-c) subject to certain approximations and initial conditions, which will be explained in the following. The provided solutions are useful to model the experimental results presented in Chapter 3. For convenience, Eqs. (2.65a-c) are reproduced here as a starting point:

$$\frac{\mathrm{d}u_p}{\mathrm{d}z} = -\frac{\alpha}{2}u_p + i\gamma|u_p|^2u_p + i2\gamma|u_s|^2u_p + i2\gamma|u_i|^2u_p + i2\gamma u_p^* u_s u_i \exp(i\Delta\beta z) \quad \text{(A.1a)}$$

$$\frac{\mathrm{d}u_s}{\mathrm{d}z} = -\frac{\alpha}{2}u_s + i\gamma|u_s|^2u_s + i2\gamma|u_p|^2u_s + i2\gamma|u_i|^2u_s + i\gamma u_p^2 u_i^* \exp(-i\Delta\beta z) \quad \text{(A.1b)}$$

$$\frac{\mathrm{d}u_i}{\mathrm{d}z} = -\frac{\alpha}{2}u_i + i\gamma|u_i|^2u_i + i2\gamma|u_p|^2u_i + i2\gamma|u_s|^2u_i + i\gamma u_p^2 u_s^* \exp(-i\Delta\beta z) \quad \text{(A.1c)}$$

where u_j with $j \in \{p, s, i\}$ is the complex slowly varying envelope of the pump, signal, or idler, respectively. The u_j are normalized such that $|u_j|^2$ represents the power carried by the j^{th} wave. We assume all three waves are linearly polarized such that they excite only one of the waveguide's fundamental polarization eigenstates. The absorption coefficient, α, describes the linear optical loss specific to the excited eigenstate. The group-velocity mismatch, $\Delta\beta$, determined by the dispersion-profile of the excited eigenstate, is given by $\Delta\beta \equiv \beta(\omega_s) + \beta(\omega_i) - 2\beta(\omega_p)$, where $\beta(\omega)$ is the frequency-dependent effective propagation constant.

The complex nonlinear parameter associated with the excited polarization

eigenstate, γ, is given by

$$\gamma = \gamma_R + i\gamma_I \equiv \frac{1}{A_{\text{eff}}}\left(n_2\frac{\omega}{c} + i\frac{\alpha_2}{2}\right) \tag{A.2}$$

where n_2, α_2 and A_{eff} are, respectively, the Kerr refraction coefficient, the two-photon-absorption coefficient and the effective mode area of the eigenstate in question. We assume the waveguide exhibits only the instantaneous nonlinear effects described by these two coefficients.

To be consistent with the design of many of the experiments presented in Chapter 3, by construction, we take the frequency spacing between the signal and idler to be sufficiently small such that $\Delta\beta \approx 0$. We also enforce the condition $|u_p|^2 \gg |u_s|^2 \gg |u_i|^2$, so that we may ignore all nonlinear effects except those proportional to $|u_p|^2$. And, we take the power in the idler wave to be zero at the waveguide's input port, $|u_i(0)|^2 = 0$. Setting $\Delta\beta = 0$ and maintaining only the most important terms, Eqs. (A.1a-c) thus reduce to

$$\frac{\mathrm{d}u_p}{\mathrm{d}z} = -\frac{\alpha}{2}u_p + i\gamma|u_p|^2u_p \tag{A.3a}$$

$$\frac{\mathrm{d}u_s}{\mathrm{d}z} = -\frac{\alpha}{2}u_s + i2\gamma|u_p|^2u_s \tag{A.3b}$$

$$\frac{\mathrm{d}u_i}{\mathrm{d}z} = -\frac{\alpha}{2}u_i + i2\gamma|u_p|^2u_i + i\gamma u_p^2u_s^* \tag{A.3c}$$

In the absence of any nonlinearity, we expect the fields to decay as $\exp(-\alpha z/2)$. So, we re-normalize the fields in terms of a new variable, $\tilde{u}_j(z)$, according to

$$u_j \equiv \tilde{u}_j e^{-\alpha z/2}, \qquad j \in \{p, s, i\} \tag{A.4}$$

Rewriting the coupled equations in terms of the $\tilde{u}_j$ gives

$$\frac{\mathrm{d}\tilde{u}_p}{\mathrm{d}z} = i\gamma|\tilde{u}_p|^2\tilde{u}_p e^{-\alpha z} \tag{A.5a}$$

$$\frac{\mathrm{d}\tilde{u}_s}{\mathrm{d}z} = i2\gamma|\tilde{u}_p|^2\tilde{u}_s e^{-\alpha z} \tag{A.5b}$$

$$\frac{\mathrm{d}\tilde{u}_i}{\mathrm{d}z} = i\gamma\left[2|\tilde{u}_p|^2\tilde{u}_i + \tilde{u}_p^2\tilde{u}_s^*\right] e^{-\alpha z} \tag{A.5c}$$

To proceed, we change variables to a new "effective distance," ν, which is related to the physical propagation distance z according to

$$\nu \equiv \int_0^z e^{-\alpha z'}\,\mathrm{d}z' = \frac{1-e^{-\alpha z}}{\alpha} \tag{A.6}$$

Using the chain rule, the derivatives in Eqs. (A.5a-c) can be rewritten with ν as the independent variable

$$\frac{\mathrm{d}\tilde{u}_j}{\mathrm{d}z} = \frac{\mathrm{d}\tilde{u}_j}{\mathrm{d}\nu}\frac{\mathrm{d}\nu}{\mathrm{d}z} = \frac{\mathrm{d}\tilde{u}_j}{\mathrm{d}\nu}e^{-\alpha z} \tag{A.7}$$

Using (A.7), the coupled equations transform to the following very simple form

$$\frac{\mathrm{d}\tilde{u}_p}{\mathrm{d}\nu} = i\gamma|\tilde{u}_p|^2\tilde{u}_p \tag{A.8a}$$

$$\frac{\mathrm{d}\tilde{u}_s}{\mathrm{d}\nu} = i2\gamma|\tilde{u}_p|^2\tilde{u}_s \tag{A.8b}$$

$$\frac{\mathrm{d}\tilde{u}_i}{\mathrm{d}\nu} = i\gamma\left[2|\tilde{u}_p|^2\tilde{u}_i + \tilde{u}_p^2\tilde{u}_s^*\right] \tag{A.8c}$$

In similar fashion to Section 2.5, we can re-write the $\tilde{u}_j$ using phasor notation, $\tilde{u}_j = m_j \exp(i\phi_j)$, where m_j and ϕ_j represent the ν-dependent magnitude and phase of $\tilde{u}_j$. Separating Eq. (A.8a) into its real and imaginary components gives, respectively,

$$\frac{\mathrm{d}m_p}{\mathrm{d}\nu} = -\gamma_I m_p^3 \qquad\qquad \frac{\mathrm{d}\phi_p}{\mathrm{d}\nu} = \gamma_R m_p^2 \tag{A.9}$$

The first equation in (A.9) can be solved directly:

$$m_p^2(\nu) = \frac{m_p^2(0)}{1 + 2\gamma_I m_p^2(0)\nu} \tag{A.10}$$

Then, inserting Eq. (A.10) into the second (A.9)-equation and integrating, we have

$$\phi_p(\nu) - \phi_p(0) = \frac{\gamma_R}{2\gamma_I} \ln\left[1 + 2\gamma_I m_p^2(0)\nu\right] \tag{A.11}$$

Now working with the equation for the signal, we can substitute Eq. (A.10) into Eq. (A.8b) to obtain

$$\frac{1}{\tilde{u}_s}\frac{\mathrm{d}\tilde{u}_s}{\mathrm{d}\nu} = \frac{i2\gamma m_p^2(0)}{1 + 2\gamma_I m_p^2(0)\nu}, \tag{A.12}$$

which integrates to give

$$\tilde{u}_s(\nu) = \frac{\tilde{u}_s(0)}{1 + 2\gamma_I m_p^2(0)\nu} \exp\left(i\frac{\gamma_R}{\gamma_I} \ln\left[1 + 2\gamma_I m_p^2(0)\nu\right]\right) \tag{A.13}$$

If we assume, without loss of generality, that $\phi_p(0) = 0$, then we can re-cast Eq. (A.13) in terms of Eqs. (A.10) and (A.11) as

$$\tilde{u}_s(\nu) = \tilde{u}_s(0)\frac{m_p^2(\nu)}{m_p^2(0)} \exp\left(i2\phi_p(\nu)\right) = \frac{\tilde{u}_s(0)}{m_p^2(0)}\tilde{u}_p^2(\nu) \tag{A.14}$$

Finally, we turn to Eq. (A.8c), which can be re-written as

$$\frac{\mathrm{d}\tilde{u}_i}{\mathrm{d}\nu} - i2\gamma|\tilde{u}_p|^2\tilde{u}_i = i\gamma\tilde{u}_p^2\tilde{u}_s^* \tag{A.15}$$

Both $\tilde{u}_p$ and $\tilde{u}_s$ are known, so Eq. (A.15) is a linear, inhomogeneous differential equation with ν-dependent coefficients, which can be solved using the following integrating factor

$$M(\nu) = \exp\left[-i2\gamma \int_0^\nu |\tilde{u}_p(\nu')|^2 \,\mathrm{d}\nu'\right] \tag{A.16}$$

$$= \frac{m_p^2(0)}{\tilde{u}_p^2(\nu)} \tag{A.17}$$

where the integration and exponentiation required to derive (A.17) from (A.16) are nearly identical to the steps used to go from (A.12) to (A.14).

Multiplying Eq. (A.15) by the integrating factor, we have

$$\frac{\mathrm{d}}{\mathrm{d}\nu}\left[\frac{\tilde{u}_i(\nu)}{\tilde{u}_p^2(\nu)}\right] = i\gamma\tilde{u}_s^* \tag{A.18}$$

Then, substituting Eq. (A.14) into the RHS of Eq. (A.18) and integrating, we obtain

$$\frac{\tilde{u}_i(\nu)}{\tilde{u}_p^2(\nu)} = i\gamma\frac{\tilde{u}_s^*(0)}{m_p^2(0)}\int_0^\nu \left[\tilde{u}_p^*(\nu')\right]^2 \mathrm{d}\nu' \tag{A.19}$$

where we have enforced the previously stated initial condition that the idler is absent at the waveguide's input port, $\tilde{u}_i(0) = 0$. The integral in Eq. (A.19) can be computed by the inserting the ν-dependent complex amplitude of the pump, given by combining Eqs. (A.10) and (A.11):

$$\begin{aligned}\int_0^\nu [\tilde{u}_p^*(\nu')]^2\,\mathrm{d}\nu' =& \int_0^\nu \frac{m_p^2(0)}{1+2\gamma_I m_p^2(0)\nu'}\exp\left\{-i\frac{\gamma_R}{\gamma_I}\ln[1+2\gamma_I m_p^2(0)\nu']\right\}\mathrm{d}\nu' \\ =&\frac{i}{2\gamma_R}\exp\left\{-i\frac{\gamma_R}{\gamma_I}\ln[1+2\gamma_I m_p^2(0)\nu]\right\} - \frac{i}{2\gamma_R} \\ =&\frac{i}{2\gamma_R}\left[\exp\left(-i2\phi_p\left(\nu\right)\right) - 1\right]\end{aligned} \tag{A.20}$$

Now, rearranging Eq. (A.19) and inserting the result from (A.20) to solve for $\tilde{u}_i(\nu)$, we have

$$\begin{aligned}\tilde{u}_i(\nu) =& i\gamma\frac{\tilde{u}_s^*(0)}{m_p^2(0)}\tilde{u}_p^2(\nu)\int_0^\nu [\tilde{u}_p^*(\nu')]^2\,\mathrm{d}\nu' \\ =& i\gamma\frac{\tilde{u}_s^*(0)}{m_p^2(0)}m_p^2(\nu)\exp(i2\phi_p(\nu))\times\frac{i}{2\gamma_R}[\exp(-i2\phi_p(\nu)) - 1] \\ =& -\frac{\gamma}{2\gamma_R}\frac{\tilde{u}_s^*(0)}{1+2\gamma_I m_p^2(0)\nu}[1-\exp(i2\phi_p(\nu))]\end{aligned} \tag{A.21}$$

Simplifying this expression, we arrive at

$$\tilde{u}_i(\nu) = \frac{\gamma}{\gamma_R}\tilde{u}_s^*(0)e^{i\phi_p(\nu)}\frac{\sin(\phi_p(\nu))}{1+2\gamma_I m_p^2(0)\nu} \tag{A.22}$$

Putting all these results together, we can construct expressions for the slowly varying envelopes of the pump, signal and idler waves. At the output plane of a waveguide whose physical length is L, we have

$$u_p(L) = \frac{m_p(0)e^{-\alpha L/2}}{\sqrt{1+2\gamma_I m_p^2(0)L_{\text{eff}}}}\exp\left\{i\frac{\gamma_R}{2\gamma_I}\ln[1+2\gamma_I m_p^2(0)L_{\text{eff}}]\right\} \tag{A.23a}$$

$$u_s(L) = \frac{m_s(0)e^{-\alpha L/2}}{1+2\gamma_I m_p^2(0)L_{\text{eff}}}\exp\left\{i\Big(\phi_s(0)+\frac{\gamma_R}{\gamma_I}\ln[1+2\gamma_I m_p^2(0)L_{\text{eff}}]\Big)\right\} \tag{A.23b}$$

$$\begin{aligned} u_i(L) = &\frac{\gamma}{\gamma_R}\sin\Big(\frac{\gamma_R}{2\gamma_I}\ln[1+2\gamma_I m_p^2(0)L_{\text{eff}}]\Big)\frac{m_s(0)e^{-\alpha L/2}}{1+2\gamma_I m_p^2(0)L_{\text{eff}}} \\ &\times\exp\left\{i\Big(-\phi_s(0)+\frac{\gamma_R}{2\gamma_I}\ln[1+2\gamma_I m_p^2(0)L_{\text{eff}}]\Big)\right\} \end{aligned} \tag{A.23c}$$

where L_{eff} is the effective nonlinear length, given by $L_{\text{eff}} = [1-\exp(-\alpha L)]/\alpha$.

Many of the continuous-wave four-wave-mixing results presented in Chap. 3 are stated in terms of the "conversion efficiency." We choose to define the conversion efficiency, η_{FWM}, as the ratio of the power carried by the idler wave at the output to the power of the signal at the input,

$$\eta_{\text{FWM}} \equiv \frac{P_i(L)}{P_s(0)} = \frac{|u_i(L)|^2}{|u_s(0)|^2} \tag{A.24}$$

Written in terms of Eqs. (A.23b) and (A.23c), the conversion efficiency is

$$\eta_{\text{FWM}} = e^{-\alpha L}\left\{\frac{|\gamma|}{\gamma_R}\frac{\sin\left(\frac{\gamma_R}{2\gamma_I}\ln[1+2\gamma_I m_p^2(0)L_{\text{eff}}]\right)}{1+2\gamma_I m_p^2(0)L_{\text{eff}}}\right\}^2 \tag{A.25}$$

Using the definitions in Eqs. (2.55) and (2.56), we can re-cast the conversion effi-

ciency in terms of n_2, α_2 and the input pump intensity, I_{p0},

$$\eta_{\mathrm{FWM}} = e^{-\alpha L}\left\{\left(1+\frac{c^2}{4\omega^2}\frac{\alpha_2^2}{n_2^2}\right)^{1/2}\frac{\sin(\frac{\omega n_2}{c\,\alpha_2}\ln[1+\alpha_2 I_{p0}L_{\mathrm{eff}}])}{1+\alpha_2 I_{p0}L_{\mathrm{eff}}}\right\}^2 \tag{A.26}$$

Alternatively, the conversion efficiency can be expressed in terms of the scalar effective susceptibility and the two-photon-absorption coefficient

$$\eta_{\mathrm{FWM}} = e^{-\alpha L}\left\{\frac{|\chi^{(3)}|}{\chi_R^{(3)}}\frac{\sin(\frac{\chi_R^{(3)}}{2\chi_I^{(3)}}\ln[1+\alpha_2 I_{p0}L_{\mathrm{eff}}])}{1+\alpha_2 I_{p0}L_{\mathrm{eff}}}\right\}^2 \tag{A.27}$$

It is sometimes the case that the two-photon absorption in a waveguide is vanishingly small. In the limit $\alpha_2 \to 0$, then $\ln[1+\alpha_2 I_{p0}L_{\mathrm{eff}}]$ approaches $\alpha_2 I_{p0}L_{\mathrm{eff}}$, and Eq. (A.26) reduces to

$$\lim_{\alpha_2\to 0}[\eta_{\mathrm{FWM}}] = e^{-\alpha L}\sin^2\left(\frac{\omega}{c}n_2 I_{p0}L_{\mathrm{eff}}\right) \tag{A.28}$$

However, care is needed in applying these equations. From the outset, we assumed $P_p \gg P_s \gg P_i$. It is only in this limit that the above solutions are valid (but none of the expressions derived above actually enforce this condition). In essence, we have assumed that the conversion efficiency must be small for Eq. (A.28) to apply. In other words, the assumption $P_s \gg P_i$ implies that $\sin^2\left(\frac{\omega}{c}n_2 I_{p0}L_{\mathrm{eff}}\right) \ll 1$, in which case Eq. (A.28) can be reduced to

$$\eta_{\mathrm{FWM}} = e^{-\alpha L}\left(\frac{\omega}{c}n_2 I_{p0}L_{\mathrm{eff}}\right)^2 \tag{A.29}$$

Eq. (A.29) is frequently the expression used to model continuous-wave four-wave-mixing observations found in the literature. It is valid in the limits of low conversion efficiency and vanishingly small two-photon absorption.

Appendix B: Free-carrier-induced frequency-dependence of XAM and XPM

If the cross-amplitude and cross-phase modulations measured by the apparatus described in Chap. 4 are frequency-dependent – as is the case when the waveguide displays non-negligible delayed absorption and refraction – then the small-signal analysis used to derive Eq. (4.3) fails. This Appendix provides a quantitative description of how the presence of free carriers modifies the observations of the cross-modulation measurements of the c-Si waveguide, which are presented in Sect. 5.3. The mathematical model constructed in the following is used to simulate the crystalline-silicon data appearing in Figs. 5.3(a), 5.3(b) and 5.4(a).

The starting point is Eq. (90) of Ref. [23], which was derived to describe free-carrier effects on four-wave mixing. The equation is reproduced here, but the effects of linear propagation have been ignored:

$$\frac{\partial}{\partial z}\tilde{u}(z,t) = i\gamma_e|\tilde{u}(z,t)|^2\tilde{u}(z,t) + i\gamma_f\tilde{u}(z,t)\int_{-\infty}^{t} e^{-(t-t')/\tau_c}|\tilde{u}(z,t')|^4\,\mathrm{d}t' \qquad \text{(B.1)}$$

Here, γ_e represents the waveguide's electronic nonlinear parameter, which describes the instantaneous nonlinear effects of two-photon absorption and Kerr refraction. It is the same nonlinear parameter defined in Eq. (2.56), but the subscript 'e' has been inserted to prevent confusing it with γ_f. The free-carrier population is assumed to

decay mono-exponentially in time, with a $1/e$ lifetime given by τ_c. The strength of the free-carrier effects is determined by the complex free-carrier nonlinear parameter γ_f,

$$\gamma_f = \frac{\alpha_2}{2\hbar\omega A_{\text{eff}}^2} \frac{n_{\text{mat}}(\omega)}{n_{\text{eff}}(\omega)} \left[\frac{\omega}{c} \sigma_n(\omega) + i \frac{\sigma_a(\omega)}{2} \right] \tag{B.2}$$

where the frequency-dependent factors n_{mat}, n_{eff}, σ_n and σ_a represent, respectively, the refractive index of the core material, the effective refractive index of the mode, the free-carrier-dispersion cross section and the free-carrier-absorption cross section.

The approach employed here is essentially the same as that used to derive the coupled-wave equations for continuous-wave four-wave mixing, Eqs. (2.65). However, in this case, the optical field is permitted to have 6 monochromatic components, three which describe the sinusoidally modulated pump, and three which describe the cross-modulated probe:

$$\begin{aligned} \tilde{u}(z,t) = {} & u_1(z)e^{-i\omega_1 t} + u_{1+}(z)e^{-i(\omega_1+\Omega)t} + u_{1-}(z)e^{-i(\omega_1-\Omega)t} \\ & + u_2(z)e^{-i\omega_2 t} + u_{2+}(z)e^{-i(\omega_2+\Omega)t} + u_{2-}(z)e^{-i(\omega_2-\Omega)t} \end{aligned} \tag{B.3}$$

where $u_1(z)$, $u_{1+}(z)$ and $u_{1-}(z)$ represent the z-dependent complex amplitudes of the main tone of the pump and its upper and lower sidebands, respectively. Similarly, $u_2(z)$, $u_{2+}(z)$ and $u_{2-}(z)$ represent the main tone of the probe and its upper and lower sidebands. The RF modulation frequency is given by Ω. As usual, the complex amplitudes are normalized such that $|u_j|^2 = P_j$, where P_j represents the power carried by the j^{th} wave.

Using Eq. (B.3), evaluation of the integral expression in Eq. (B.1) leads to a sequence of Lorentzian terms. The pump is assumed to be much stronger than

the probe, and the modulation depth of each is assumed to be small, such that $|u_1(z)| \gg |u_2(z)| > |u_{1\pm}(z)| \gg |u_{2\pm}(z)|$. It is also assumed that the frequency-difference between the pump and probe is much larger than the RF modulation frequency: $|\omega_1 - \omega_2| \gg \Omega$. The process of inserting Eq. (B.3) into Eq. (B.1), evaluating the integral, separating the equations for each frequency component, and retaining only the most important terms therefore leaves the following 6 coupled-wave equations:

$$\frac{\partial u_1}{\partial z} = i\gamma_e |u_1|^2 u_1 + i4\gamma_f \tau_c |u_1|^4 u_1 \tag{B.4a}$$

$$\begin{aligned}\frac{\partial u_{1+}}{\partial z} &= i\gamma_e \left[u_1^2 u_{1-}^* + 2|u_1|^2 u_{1+}\right] \\ &\quad + i\gamma_f \left[4\tau_c |u_1|^4 u_{1+} + L\left(2|u_1|^2 u_1^2 u_{1-}^* + 2|u_1|^4 u_{1+}\right)\right]\end{aligned} \tag{B.4b}$$

$$\begin{aligned}\frac{\partial u_{1-}}{\partial z} &= i\gamma_e \left[u_1^2 u_{1+}^* + 2|u_1|^2 u_{1-}\right] \\ &\quad + i\gamma_f \left[4\tau_c |u_1|^4 u_{1-} + L^*\left(2|u_1|^4 u_{1-} + 2|u_1|^2 u_1^2 u_{1+}^*\right)\right]\end{aligned} \tag{B.4c}$$

$$\frac{\partial u_2}{\partial z} = i2\gamma_e |u_1|^2 u_2 + i4\gamma_f \tau_c |u_1|^4 u_2 \tag{B.4d}$$

$$\begin{aligned}\frac{\partial u_{2+}}{\partial z} &= i\gamma_e \left[2|u_1|^2 u_{2+} + 2u_1 u_{1-}^* u_2 + 2u_1^* u_{1+} u_2\right] \\ &\quad + i4\gamma_f \tau_c |u_1|^4 u_{2+} \\ &\quad + i\gamma_f L \left[2|u_1|^2 u_1 u_{1-}^* u_2 + 2|u_1|^2 u_1^* u_{1+} u_2\right]\end{aligned} \tag{B.4e}$$

$$\begin{aligned}\frac{\partial u_{2-}}{\partial z} &= i\gamma_e \left[2|u_1|^2 u_{2-} + 2u_1 u_{1+}^* u_2 + 2u_1^* u_{1-} u_2\right] \\ &\quad + i4\gamma_f \tau_c |u_1|^4 u_{2-} \\ &\quad + i\gamma_f L^* \left[2|u_1|^2 u_1^* u_{1-} u_2 + 2|u_1|^2 u_1 u_{1+}^* u_2\right]\end{aligned} \tag{B.4f}$$

where L is a frequency-dependent Lorentzian factor, centered about $\Omega = 0$, which

is given by

$$L = \frac{\frac{1}{\tau_c} + i\Omega}{\frac{1}{\tau_c^2} + \Omega^2} \tag{B.5}$$

Unfortunately, Eqs. (B.4a–f) do not permit analytical solutions, but it is straightforward to solve them numerically. The time-varying field inserted at $z = 0$ is assumed to consist of a sinusoidally modulated pump and a continuous-wave probe (which has yet to acquire any modulation):

$$\begin{aligned} \tilde{u}(z=0,t) &= u_1(0)[1 + M\sin(\Omega t)]e^{-i\omega_1 t} + u_2(0)e^{-i\omega_2 t} \\ &= u_1(0)e^{-i\omega_1 t} + i\frac{M}{2}u_1(0)e^{-i(\omega_1+\Omega)t} - i\frac{M}{2}u_1(0)e^{-i(\omega_1-\Omega)t} + u_2(0)e^{-i\omega_2 t}, \end{aligned} \tag{B.6}$$

where M is the modulation depth. From the second line in Eq. (B.6), we can make the following associations:

$$u_{1+}(0) = i\frac{M}{2}u_1(0) \qquad \text{and} \qquad u_{1-}(0) = -i\frac{M}{2}u_1(0) \tag{B.7}$$

Without loss of generality, we take the phase associated with the complex amplitude of the main tone of the pump, u_1, to be zero at $z = 0$. The probe is generated by a second laser, and therefore the phase of the inserted probe, $u_2(0)$, is allowed to take any value on the interval $[-\pi, \pi)$. The probe-sidebands are assumed to be absent at the input port. Taking the same approach used in the discussion surrounding Eqs. (3.26) and (3.27), it can be shown that (under the above assumptions) the phases associated with the probe-sidebands, $\phi_{2\pm}$, auto-initialize to specific values at $z = 0$. For example, the phase of $u_{2+}(0)$ is

$$\phi_{2+}(0) = \tan^{-1}\left(\frac{\mathbf{Im}\{x\}}{\mathbf{Re}\{x\}}\right) \tag{B.8}$$

Table B.1: Parameters used to calculate the frequency-dependent XAM and XPM of the c-Si nanowire waveguide.

	Value	Notes
A_{eff}	$0.1\mu\text{m}^2$	estimated
$n_{\text{mat}}/n_{\text{eff}}$	≈ 1	estimated
L	1 cm	measured
n_2	0.45×10^{-17} m^2/W	taken from [21]
α_2	0.8×10^{-11} m/W	taken from [21]
σ_a	1.45×10^{-17} cm^2	taken from [23]
σ_n	-5.3×10^{-21} cm^3	taken from [23]
τ_c	1.9 ns	measured
$\lvert u_1(0)\rvert^2$	25 mW	measured
$\lvert u_2(0)\rvert^2$	1 mW	measured

where the quantity x is given by

$$x = \left[i\gamma_e \left(u_1 u_{1-}^* u_2 + u_1^* u_{1+} u_2 \right) + i\gamma_f L \left(|u_1|^2 u_1 u_{1-}^* u_2 + |u_1|^2 u_1^* u_{1+} u_2 \right) \right]_{z=0}$$

A similar relation exists for $\phi_{2-}(0)$.

The $S_{21}(f)$ transfer function expected for the c-Si waveguide of Sect. 5.3 is calculated by numerically integrating Eqs (B.4a-f) subject to the initial conditions given above. Table B.1 lists the parameters used in the calculations. For the case of no dispersive fiber in the setup, the experiment is sensitive only to cross-amplitude modulation, and the $S_{21}(f)$ transfer function recorded by the network analyzer obeys the following proportionality:

$$S_{21}(f) \propto \left[u_2^* u_{2-} + u_2 u_{2+}^* \right]_{z=l} \tag{B.9}$$

where l is the length of the waveguide. Figure B.1 shows the simulated data alongside

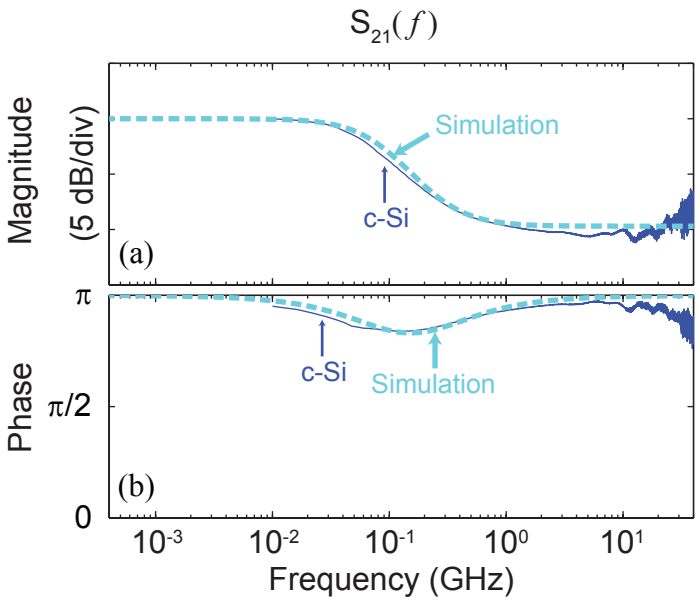

Figure B.1: (a) Normalized magnitude and (b) phase of S_{21} vs. the modulation frequency for the c-Si waveguide when the dispersive spool is omitted from the setup. The experimental data, shown in dark blue, are the same as those plotted in Fig. 5.3. The dashed cyan lines represent the result of the simulation.

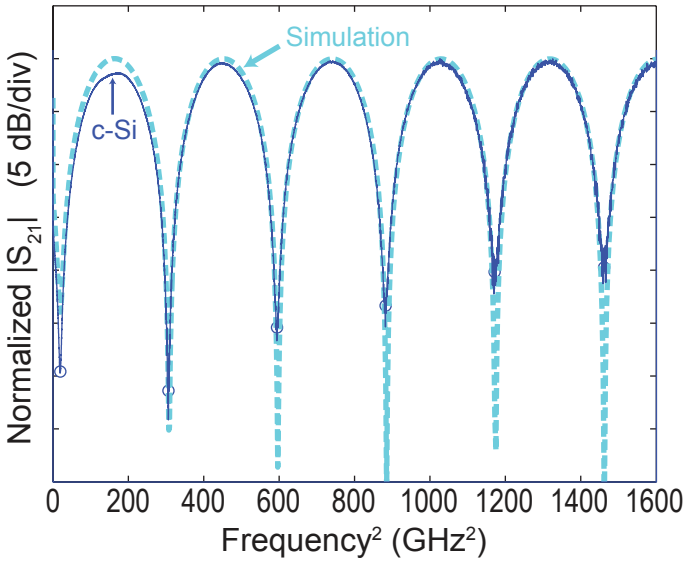

Figure B.2: Measured and simulated magnitude of S_{21} vs. the square of the modulation frequency with dispersive fiber in the setup. The solid blue line is the measured result (the same as the crystalline-silicon experimental data of Fig. 5.4). The dashed cyan line is the result of the simulation.

the measured data. The agreement between the two is very good.

The analysis can be extended to consider the experiment with the dispersive spool installed in the setup. As the probe propagates in the fiber, each of the three spectral components accumulate different amounts of phase due to the fiber-dispersion. The $S_{21}(f)$ transfer function recorded by the network analyzer is therefore proportional to

$$S_{21}(f) \propto [u_2^* u_{2-}]_{z=l} \times e^{i\Omega^2 \beta_2 l_{\text{spool}}/2} + [u_2 u_{2+}^*]_{z=l} \times e^{-i\Omega^2 \beta_2 l_{\text{spool}}/2} \tag{B.10}$$

where l again represents the length of the waveguide, l_{spool} is the length of the fiber-spool and β_2 is the group-velocity dispersion. The dispersion-length product of the fiber-spool was calculated from the measured data using the fit to Eq. (4.15), as shown in Fig. 5.4(b). The calculated dispersion-length product is $\beta_2 l_{\text{spool}} = -5.52 \times 10^{-22}$ s^2, consistent with that expected for 25 km of single-mode fiber. The dashed cyan line in Fig. B.2 is the result of the simulation, and the blue solid line represents the same measured data shown in Fig. 5.4(a). The simulated data agree well with the measured data.

Bibliography

[1] G. T. Reed and A. P. Knights. *Silicon Photonics: an introduction*. Jon Wiley & Sons, Chicester, 1st edition, 2004.

[2] A. Biberman and K. Bergman. Optical interconnection networks for high-performance computing systems. *Reports on Progress in Physics*, 75(4):046402, 2012.

[3] A. Shacham, K. Bergman, and L. P. Carloni. Photonic Networks-on-Chip for Future Generations of Chip Multiprocessors. *IEEE Transactions on Computers*, 57(9):1246–1260, 2008.

[4] K. Bergman, L. P. Carloni, A. Biberman, J. Chan, and G. Hendry. *Photonic Network-on-Chip Design*. Springer, New York, 1st edition, 2014.

[5] B. Jalali and S. Fathpour. Silicon Photonics. *Journal of Lightwave Technology*, 24(12):4600–4615, 2006.

[6] J. Shah. Microsystems Technology Office: Photonically Optimized Embedded Microprocessors (POEM). `http://www.darpa.mil/Our_Work/MTO/Programs/Photonically_Optimized_Embedded_Microprocessors_(POEM).aspx`, 2014. [Online; accessed 11-September-2014].

[7] C. Monat, C. Grillet, M. Collins, A. Clark, J. Schroeder, C. Xiong, J. Li, L. O'Faolain, T. F. Krauss, B. J. Eggleton, and D. J. Moss. Integrated optical auto-correlator based on third-harmonic generation in a silicon photonic crystal waveguide. *Nature Communications*, 5:3246, 2014.

[8] R. Soref. The Past, Present, and Future of Silicon Photonics. *IEEE Journal of Selected Topics in Quantum Electronics*, 12(6):1678–1687, 2006.

[9] J. Leuthold, C. Koos, and W. Freude. Nonlinear silicon photonics. *Nature Photonics*, 4(8):535–544, 2010.

[10] D. Liang and J. E. Bowers. Recent progress in lasers on silicon. *Nature Photonics*, 4(8):511–517, 2010.

[11] D. J. Moss, R. Morandotti, A. L. Gaeta, and M. Lipson. New CMOS-compatible platforms based on silicon nitride and Hydex for nonlinear optics. *Nature Photonics*, 7(8):597–607, 2013.

[12] R. W. Boyd. *Nonlinear Optics*. Academic Press, London, 3rd edition, 2008.

[13] J. Hansryd, P. A. Andrekson, M. Westlund, J. Li, and P.-O. Hedekvist. Fiber-Based Optical Parametric Amplifiers and Their Applications. *IEEE Journal of Selected Topics in Quantum Electronics*, 8(3):506–520, 2002.

[14] K. Inoue. Four-Wave Mixing in an Optical Fiber in the Zero-Dispersion Wavelength Region. *Journal of Lightwave Technology*, 10(11):1553–1561, 1992.

[15] A. Apiratikul, W. Astar, G. M. Carter, and T. E. Murphy. 10-Gb/s Wavelength and Pulse Format Conversion Using Four-Wave Mixing in a GaAs Waveguide. *IEEE Photonics Technology Letters*, 22(12):872–874, 2010.

[16] A. B. Fallakhair, K. S. Li, and T. E. Murphy. WGMODES. `http://www.photonics.umd.edu/software/wgmodes/`. [Online; accessed 18-August-2014].

[17] A. B. Fallahkhair, K. S. Li, and T. E. Murphy. Vector Finite Difference Modesolver for Anisotropic Dielectric Waveguides. *Journal of Lightwave Technology*, 26(11):1423–1431, 2008.

[18] S. Gehrsitz, F. K. Reinhart, C. Gourgon, N. Herres, A. Vonlanthen, and H. Sigg. The refractive index of $Al_xGa_{1-x}As$ below the band gap: Accurate determination and empirical modeling. *Journal of Applied Phyics*, 87(11):7825–7837, 2000.

[19] R. S. Grant. Effective non-linear coefficients of optical waveguides. *Optical and Quantum Electronics*, 28(9):1161–1173, 1996.

[20] K. W. DeLong, B. Rochford, and G. I. Stegeman. Effect of two-photon absorption on all-optical guided-wave devices. *Applied Physics Letters*, 55(18):1823–1825, 1989.

[21] M. Dinu, F. Quochi, and H. Garcia. Third-order nonlinearities in silicon at telecom wavelengths. *Applied Physics Letters*, 82(18):2954–2956, 2003.

[22] M. Sheik-Bahae, D. C. Hutchings, D. J. Hagan, and E. W. Van Stryland. Dispersion of Bound Electronic Nonlinear Refraction in Solids. *IEEE Journal of Quantum Electronics*, 27(6):1296–1309, 1991.

[23] Q. Lin, O. J. Painter, and G. P. Agrawal. Nonlinear optical phenomena in silicon waveguides: Modeling and applications. *Optics Express*, 15(25):16604–16644, 2007.

[24] A. Villeneuve, C. C. Yang, G. I. Stegeman, C.-H. Lin, and H.-H. Lin. Nonlinear refractive-index and two-photon-absorption near half the band gap in AlGaAs. *Applied Physics Letters*, 62(20):2465–2467, 1993.

[25] J. S. Aitchison, D. C. Hutchings, J. U. Kang, G. I. Stegeman, and A. Villeneuve. The Nonlinear Optical Properties of AlGaAs at the Half Band Gap. *IEEE Journal of Quantum Electronics*, 33(3):341–348, 1997.

[26] S. J. B. Yoo. Wavelength Conversion Technologies for WDM Network Applications. *Journal of Lightwave Technology*, 14(6):955–966, 1996.

[27] T. Durhuus, B. Mikkelsen, C. Joergensen, S. L. Danielsen, and K. E. Stubkjaer. All-Optical Wavelength Conversion by Semiconductor Optical Amplifiers. *Journal of Lightwave Technology*, 14(6):642–954, 1996.

[28] K. K. Chow, K. Kukuchi, T. Nagashima, T. Hasegawa, S. Ohara, and N. Sugimoto. Four-wave mixing based widely tunable wavelength conversion using 1-m dispersion-shifted bismuth-oxide photonic crystal fiber. *Optics Express*, 15(23):15418–15423, 2007.

[29] J. P. Mack, T. U. Horton, W. Astar, K. J. Ritter, and J. M. Carter. Polarization Insensitive Wavelength Conversion by FWM of Multiformat DWDM Signals Using Birefringent PCF. *IEEE Journal of Selected Topics in Quantum Electronics*, 18(2):909–915, 2012.

[30] V. G. Ta'eed, L. Fu, M. Pelusi, M. Rochette, I. C. M. Littler, D. J. Moss, and B. J. Eggleton. Error free all optical wavelength conversion in highly nonlinear As-Se chalcogenide glass fiber. *Optics Express*, 14(22):10371–10376, 2006.

[31] J. Fukuda, K. Yamada, T. Shoji, M. Takahashi, T. Tsuchizawa, T. Watanabe, J.-i. Takahashi, and S.-i. Itabashi. Four-wave mixing in silicon wire waveguides. *Optics Express*, 13(12):4629–4637, 2005.

[32] H. K. Tsang, C. S. Wong, T. K. Liang, I. E. Day, S. W. Roberts, A. Harpin, J. Drake, and M. Asghari. Optical dispersion, two-photon absorption and self-phase modulation in silicon waveguides at 1.5 μm wavelength. *Applied Physics Letters*, 80(3):416–418, 2002.

[33] J. Cardenas, C. B. Poitras, J. T. Robinson, K. Preston, L. Chen, and M. Lipson. Low loss etchless silicon photonic waveguides. *Optics Express*, 17(6):4752–4757, 2009.

[34] M. A. Foster, A. C. Turner, M. Lipson, and A. L. Gaeta. Nonlinear optics in photonic nanowires. *Optics Express*, 16(2):1300–1320, 2008.

[35] M. A. Foster, A. C. Turner, J. E. Sharping, B. S. Schmidt, M. Lipson, and A. L. Gaeta. Broad-band optical parametric gain on a silicon photonic chip. *Nature*, 441(7096):960–963, 2006.

[36] M. A. Foster, A. C. Turner, R. Salem, M. Lipson, and A. L. Gaeta. Broad-band continuous-wave parametric wavelength conversion in silicon nanowaveguides. *Optics Express*, 15(20):12949–12958, 2007.

[37] W. Mathlouthi, H. Rong, and M. Paniccia. Characterization of efficient wavelength conversion by four-wave mixing in sub-micron silicon waveguides. *Optics Express*, 16(21):16735–16745, 2008.

[38] K. Ikeda, R. E. Saperstein, N. Alic, and Y. Fainman. Thermal and Kerr nonlinear properties of plasma-deposited silicon nitride/ silicon dioxide waveguides. *Optics Express*, 16(17):12987–12994, 2008.

[39] M. Ferrera, L. Razzari, D. Duchesne, R. Morandotti, Z. Yang, M. Liscidini, J. E. Sipe, S. Chu, B. E. Little, and D. J. Moss. Low-power continuous-wave nonlinear optics in doped silica glass integrated waveguide structures. *Nature Photonics*, 2:737–740, 2008.

[40] K. Ikeda, Y. Shen, and Y. Fainman. Enhanced optical nonlinearity in amorphous silicon and its application to waveguide devices. *Optics Express*, 15(26):17761–17771, 2007.

[41] J. F. Bauters, M. J. R. Heck, D. John, D. Dai, M.-C. Tien, J. S. Barton, A. Leinse, R. G. Heideman, D. J. Blumenthal, and J. E. Bowers. Ultra-low-loss high-aspect-ratio Si_3N_4 waveguides. *Optics Express*, 19(4):3163–3174, 2011.

[42] D. Duchesne, M. Ferrera, L. Razzari, R. Morandotti, B. E. Little, S. T. Chu, and D. J. Moss. Efficient self-phase modulation in low loss, high index doped silica glass integrated waveguides. *Optics Express*, 17(3):1865–1870, 2009.

[43] A. Pasquazi, M. Peccianti, Y. Park, B. E. Little, S. T. Chu, R. Morandotti, J. Azaña, and D. J. Moss. Sub-picosecond phase-sensitive optical pulse characterization on a chip. *Nature Photonics*, 5(10):618–623, 2011.

[44] C. Grillet, L. Carletti, C. Monat, P. Grosse, B. Ben Bakir, S. Menezo, J. M. Fedeli, and D. J. Moss. Amorphous silicon nanowires combining high nonlinearity, FOM and optical stability. *Optics Express*, 20(20):22609–22615, 2012.

[45] R. Takei, S. Manako, E. Omoda, Y. Sakakibara, M. Mori, and T. Kamei. Sub-1 dB/cm submicrometer-scale amorphous silicon waveguide for backend on-chip optical interconnect. *Optics Express*, 22(4):4779–4788, 2014.

[46] J. S. Levy, A. Gondarenko, M. A. Foster, A. C. Turner-Foster, A. L. Gaeta, and M. Lipson. CMOS-compatible multiple-wavelength oscillator for on-chip optical interconnects. *Nature Photonics*, 4(1):37–40, 2009.

[47] Y. Okawachi, K. Saha, J. S. Levy, H. Wen, M. Lipson, and A. L. Gaeta. Octave-spanning frequency comb generation in a silicon nitride chip. *Optics Letters*, 36(17):3398–3400, 2011.

[48] A. Pasquazi, Y. Park, J. Azaña, R. Morandotti, B. E. Little, S. T. Chu, and D. J. Moss. Efficient wavelength conversion and net parametric gain via Four Wave Mixing in a high index doped silica waveguide. *Optics Express*, 18(8):7634–7641, 2010.

[49] B. Kuyken, S. Clemmen, S. K. Selvaraja, W. Bogaerts, D. Van Thourhout, P. Emplit, S. Massar, G. Roelkens, and R. Baets. On-chip parametric amplification with 26.5 dB gain at telecommunications wavelengths using CMOS-compatible hyrdogenated amorphous silicon waveguides. *Optics Letters*, 36(4):552–554, 2011.

[50] K.-Y. Wang and A. C. Foster. Ultralow power continuous-wave frequency conversion in hydrogenated amorphous silicon waveguides. *Optics Letters*, 37(8):1331–1333, 2012.

[51] J. Hu, V. Tarasov, N. Carlie, N.-N. Feng, L. Petit, A. Agarwal, K. Richardson, and L. Kimerling. Si-CMOS-compatible lift-off fabrication of low-loss planar chalcogenide waveguides. *Optics Express*, 15:11798–11807, 2007.

[52] D.-Y. Choi, S. Madden, D. A. Bulla, R. Wang, A. Rode, and B. Luther-Davies. Submicrometer-Thick Low-Loss As_2S_3 Planar Waveguides for Nonlinear Optical Devices. *IEEE Photonics Technology Letters*, 22:495–497, 2010.

[53] B. J. Eggleton, B. Luther-Davies, and K. Richardson. Chalcogenide photonics. *Nature Photonics*, 5:141–148, 2011.

[54] M. D. Pelusi, F. Luan, S. Madden, D.-Y. Choi, D. A. Bulla, B. Luther-Davies, and B. J. Eggleton. Wavelength Conversion of High-speed Phase and Intensity Modulated Signals Using a Highly Nonlinear Chalcogenide Glass Chip. *IEEE Photonics Technology Letters*, 22(1):3–5, 2010.

[55] M. R. E. Lamont, B. Luther-Davies, D.-Y. Choi, S. Madden, X. Gai, and B. J. Eggleton. Net-gain from a parametric amplifier on a chalcogenide optical chip. *Optics Express*, 16:20374–20381, 2008.

[56] A. Boskovic, S. V. Chernikov, and J. R. Taylor. Direct continuous-wave measurement of n_2 in various types of telecommunication fiber at 1.55 μm. *Optics Letters*, 21(24):1966–1968, 1996.

[57] G. A. Siviloglou, S. Suntsov, R. El-Ganainy, R. Iwanow, G. I. Stegeman, D. N. Christodoulides, R. Morandotti, D. Modotto, A. Locatelli, C. De Angelis, F. Pozzi, C. R. Stanley, and M. Sorel. Enhanced third-order nonlinear effects in optical AlGaAs nanowires. *Optics Express*, 14(20):9377–9384, 2006.

[58] K. Dolgaleva, W. C. Ng, L. Qian, J. S. Aitchison, M. C. Camasta, and M. Sorel. Broadband self-phase modulation, cross-phase modulation, and four-wave mixing in 9-mm-long AlGaAs waveguides. *Optics Letters*, 35(24):4093–4095, 2010.

[59] K. Dolgaleva, W. C. Ng, L. Qian, and J. S. Aitchison. Compact highly-nonlinear AlGaAs waveguides for efficient wavelength conversion. *Optics Express*, 19(13):12440–12455, 2011.

[60] B. M. Cannon, T. Mahmood, W. Astar, P. Apiratikul, G. Porkolab, P. Boudra, T. Mohsenin, C. J. K. Richardson, and G. M. Carter. All-optical amplitude-phase transmultiplexing of RZ-OOK and RZ-BPSK to RZ-QPSK by polarization-insensitive XPM using a nonlinear birefringent AlGaAs waveguide. *Optics Express*, 21(17):19885–19899, 2013.

[61] C. Lacava, V. Pusino, P. Minzioni, M. Sorel, and I. Cristiani. Nonlinear properties of AlGaAs waveguides in continuous wave operation regime. *Optics Express*, 22(5):5291–5298, 2014.

[62] G. A. Porkolab, P. Apiratikul, B. Wang, S. H. Guo, and C. J. K. Richardson. Low propagation loss AlGaAs waveguides fabricated with plasma-assisted photoresist reflow. *Optics Express*, 22(7):7733–7743, 2014.

[63] E. Kapon and R. Bhat. Low-loss single-mode GaAs/AlGaAs optical waveguides grown by organometallic vapor phase epitaxy. *Applied Physics Letters*, 50(23):1628–1630, 1987.

[64] J. Meier, W. S. Mohammed, A. Jugessur, L. Qian, M. Mojahedi, and J. S. Aitchison. Group velocity inversion in AlGaAs nanowires. *Optics Express*, 15(20):12755–12762, 2007.

[65] A. C. Turner, C. Manolatou, B. S. Schmidt, M. Lipson, M. A. Foster, J. E. Sharping, and A. L. Gaeta. Tailored anomalous group-velocity dispersion in silicon channel waveguides. *Optics Express*, 14(10):4357–4362, 2006.

[66] G. P. Agrawal. *Nonlinear Fiber Optics*. Academic Press, San Diego, 3rd edition, 2001.

[67] J. U. Kang, A. Villeneuve, M. Sheik-Bahae, and G. I. Stegeman. Limitation due to three-photon absorption on the useful spectral range for nonlinear optics in AlGaAs below half band gap. *Applied Physics Letters*, 65(2):147–149, 1994.

[68] P. Apiratikul. *Semiconductor Waveguides for Nonlinear Optical Signal Processing*. PhD Dissertation, Department of Electrical and Computer Engineering, University of Maryland, 2009.

[69] L. Yin and G. P. Agrawal. Impact of two-photon absorption on self-phase modulation in silicon waveguides. *Optics Letters*, 32(14):2031–2033, 2007.

[70] V. Van, T. A. Ibrahim, K. Ritter, P. P. Absil, F. G. Johnson, R. Grover, J. Goldhar, and P.-T. Ho. All-Optical Nonlinear Switching in GaAs–AlGaAs Microring Resonators. *IEEE Photonics Technology Letters*, 14(1):74–76, 2002.

[71] C. Husko, S. Combrié, Q. V. Tran, F. Raineri, C. W. Wong, and A. De Rossi. Non-trivial scaling of self-phase modulation and three-photon absorption in III-V photonic crystal waveguides. *Optics Express*, 17(25):22442–22451, 2009.

[72] G. W. Rieger, K. S. Virk, and J. F. Young. Nonlinear propagation of ultrafast 1.5 μm pulses in high-index-contrast silicon-on-insulator waveguides. *Applied Physics Letters*, 84(6):900–902, 2004.

[73] R. Dekker, A. Driessen, T. Wahlbrink, C. Moormann, J. Niehusmann, and M. Först. Ultrafast Kerr-induced all-optical wavelength conversion in silicon waveguides using 1.55 μm femtosecond pulses. *Optics Express*, 14(18):8336–8346, 2006.

[74] R. Pleban, A. Azari, R. Salem, and T. E. Murphy. SSPROP. `http://www.photonics.umd.edu/software/ssprop/`. [Online; accessed 3-September-2014].

[75] N. Shibata, R. P. Braun, and R. G. Waarts. Phase-Mismatch Dependence of Efficiency of Wave Generation Through Four-Wave Mixing in a Single-Mode Optical Fiber. *IEEE Journal of Quantum Electronics*, QE-23(7):1205–1210, 1987.

[76] J. R. Ong, R. Kumar, R. Aguinaldo, and S. Mookherjea. Efficient CW Four-Wave Mixing in Silicon-on-Insulator Micro-Rings with Active Carrier Removal. *IEEE Photonics Technology Letters*, 25(17):1699–1702, 2013.

[77] A. M. Darwish, E. P. Ippen, H. Q. Le, J. P. Donnelly, and S. H. Groves. Optimization of four-wave mixing conversion efficiency in the presence of nonlinear loss. *Applied Physics Letters*, 69(6):737–739, 1996.

[78] B. Jalali. Nonlinear optics in the mid-infrared. *Nature Photonics*, 4:506–508, 2010.

[79] K. Inoue and T. Mukai. Signal wavelength dependence of gain saturation in a fiber optical parametric amplifier. *Optics Letters*, 26(1):10–12, 2001.

[80] R. H. Stolen and J. E. Bjorkholm. Parametric Amplification and Frequency Conversion in Optical Fibers. *IEEE Journal of Quantum Electronics*, QE-18(7):1062–1072, 1982.

[81] A. Apiratikul, J. J. Wathen, G. A. Porkolab, B. Wang, L. He, T. E. Murphy, and C. J. K. Richardson. Enhanced continuous-wave four-wave mixing efficiency in nonlinear AlGaAs waveguides. *Optics Express*, 22(22):26814–26824, 2014.

[82] V. Mizrahi, K. W. DeLong, G. I. Stegeman, M. A. Saifi, and M. J. Andrejco. Two-photon absorption as a limitation to all-optical switching. *Optics Letters*, 14(20):1140–1142, 1989.

[83] J. S. Aitchison, M. K. Oliver, E. Kapon, E. Colas, and P. W. E. Smith. Role of two-photon absorption in ultrafast semiconductor optical switching devices. *Applied Physics Letters*, 56(14):1305–1307, 1990.

[84] M. Asobe, K. Suzuki, T. Kanamori, and K. Kubodera. Nonlinear refractive index measurement in chalcogenide-glass fibers by self-phase modulation. *Applied Physics Letters*, 60(10):1153–1154, 1992.

[85] C.-Y. Tai, J. Wilkinson, N. Perney, M. Netti, F. Cattaneo, C. Finlayson, and J. Baumberg. Determination of nonlinear refractive index in a Ta_2O_5 rib waveguide using self-phase modulation. *Optics Express*, 12(21):5110–5116, 2004.

[86] Y. Ruan, B. Luther-Davies, W. Li, A. Rode, V. Kolev, and S. Madden. Large phase shifts in As_2S_3 waveguides for all-optical processing devices. *Optics Letters*, 30(19):2605–2607, 2005.

[87] A. Villeneuve, C. C. Yang, G. I. Stegeman, C. N. Ironside, G. Scelsi, and R. M. Osgood. Nonlinear Absorption in a GaAs Waveguide Just Above Half the Band Gap. *IEEE Journal of Quantum Electronics*, 30(5):1172–1175, 1994.

[88] T.-K. Liang and H.-K. Tsang. Nonlinear Absorption and Raman Scattering in Silicon-on-Insulator Optical Waveguides. *IEEE Journal of Selected Topics in Quantum Electronics*, 10(5):1149–1153, 2004.

[89] H. Q. Le, W. D. Goodhue, and K. Rauschenbach. Measurement of third-order optical nonlinear susceptibility using four-wave mixing in a single-mode ridge waveguide. *Optics Letters*, 15(20):1126–1128, 1990.

[90] L. Prigent and J.-P. Hamaide. Measurement of Fiber Nonlinear Kerr Coefficient by Four-Wave Mixing. *IEEE Photonics Technology Letters*, 5(9):1092–1095, 1993.

[91] Y. Shoji, T. Ogasawara, T. Kamei, Y. Sakakibara, S. Suda, K. Kintaka, H. Kawashima, M. Okano, T. Hasama, H. Ishikawa, and M. Mori. Ultrafast nonlinear effects in hydrogenated amorphous silicon wire waveguide. *Optics Express*, 18(6):5668–348, 2010.

[92] A. R. Motamedi, A. H. Nejadmalayeri, A. Khilo, F. X. Kärtner, and E. P. Ippen. Ultrafast nonlinear optical studies of silicon nanowaveguides. *Optics Express*, 20(4):4085–4101, 2012.

[93] R. J. Suess, M. M. Jadidi, K. Kim, and T. E. Murphy. Characterization of optical nonlinearities in nanoporous silicon waveguides via pump-probe heterodyning technique. *Optics Express*, 22(14):17466–17477, 2014.

[94] F. Devaux, Y. Sorel, and J. F. Kerdiles. Simple Measurement of Fiber Dispersion and of Chirp Parameter of Intensity Modulated Light Emitter. *Journal of Lightwave Technology*, 11(12):1937–1940, 1993.

[95] A. Harke, M. Krause, and J. Mueller. Low-loss singlemode amorphous silicon waveguides. *Electronics Letters*, 41(25):1377–1379, 2005.

[96] K. Narayanan and S. F. Preble. Optical nonlinearities in hydrogenated-amorphous silicon waveguides. *Optics Express*, 18(9):8998–9005, 2010.

[97] B. Kuyken, H. Ji, S. Clemmen, S. K. Selvaraga, H. Hu, M. Pu, M. Galili, P. Jeppesen, G. Morthier, S. Massar, L. K. Oxenløwe, G. Roelkens, and R. Baets. Nonlinear properties of and nonlinear processing in hydrogenated amorphous silicon waveguides. *Optics Express*, 19(26):B146–B153, 2011.

[98] C. Lacava, P. Minzioni, E. Baldini, L. Tartara, J. M. Fedeli, and I. Cristiani. Nonlinear characterization of hydrogenated amorphous silicon waveguides and analysis of carrier dynamics. *Applied Physics Letters*, 103:141103, 2013.

[99] J. Matres, G. C. Ballesteros, P. Gautier, J-M Fédéli, J. Martí, and C. J. Oton. High nonlinear figure-of-merit amorphous silicon waveguides. *Optics Express*, 21(4):3932–3940, 2013.

[100] J. S. Pelc, K. Rivoire, S. Vo, C. Santori, D. A. Fattal, and R. G. Beausoleil. Picosecond all-optical switching in hydrogenated amorphous silicon microring resonators. *Optics Express*, 22(4):3797–3810, 2014.

[101] S. Suda, K. Tanizawa, Y. Skakakibara, T. Kamei, K. Nakanishi, E. Itoga, T. Ogasawara, R. Takei, H. Kawashima, S. Namiki, M. Mori, T. Hasama, and H. Ishikawa. Pattern-effect-free all-optical wavelength conversion using a hydrogenated amorphous silicon waveguide with ultra-fast carrier decay. *Optics Letters*, 37(8):1382–1384, 2012.

[102] S. Clemmen, A. Perret, S. K. Selvaraja, D. van Thourhout, R. Baets, Ph. Emplit, and S. Massar. Generation of correlated photons in hydrogenated amorphous-silicon waveguides. *Optics Letters*, 35(20):3483–3485, 2010.

[103] S. Uvin, U. D. Dave, B. Kuyken, S. Selvaraja, F. Leo, and G. Roelkens. Mid-infrared to telecom-band stable supercontinuum generation in hydrogenated amorphous silicon waveguides. in *Proceedings of IEEE Photonics Conference* (IEEE, 2013), pp. 380–381.

[104] K. G. Petrillo, K.-Y. Wang, A. C. Foster, and M. A. Foster. Highly sensitive ultrafast pulse characterization using hydrogenated amorphous silicon waveguides. *Optics Express*, 21(25):31229–31238, 2013.

[105] K.-Y. Wang, M. A. Foster, and A. C. Foster. Wavelength-agile near-IR chip-based optical parametric oscillator using a deposited silicon waveguide. in *CLEO: 2013 Postdeadline*, OSA Postdeadline Paper Digest (online) (Optical Society of America, 2013), paper CTh5D.7.

[106] K.-Y. Wang, V. G. Velev, K. F. Lee, A. S. Kowligy, P. Kumar, M. A. Foster, A. C. Foster, and Y.-P. Huang. Multichannel photon-pair generation using hydrogenated amorphous silicon waveguides. *Optics Letters*, 39(4):914–916, 2014.

[107] X. Gai, D.-Y. Choi, and B. Luther-Davies. Negligible nonlinear absorption in hydrogenated amorphous silicon at 1.55 μm for ultra-fast nonlinear signal processing. *Optics Express*, 22(8):9948–9958, 2014.

[108] K.-Y. Wang and A. C. Foster. GHz Near-IR Optical Parametric Amplifier using a Hydrogenated Amorphous Silicon Waveguide. in *CLEO: 2014*, OSA Technical Digest (online) (Optical Society of America, 2014), paper SW3I.7.

[109] A. C. Turner-Foster, M. A. Foster, J. S. Levy, C. B. Poitras, R. Salem, A. L. Gaeta, and M. Lipson. Ultrashort free-carrier lifetime in low-loss silicon nanowaveguides. *Optics Express*, 18(4):3582–3591, 2010.

[110] V. R. Almeida, R. R. Panepucci, and M. Lipson. Nanotaper for compact mode conversion. *Optics Letters*, 28(15):1302–1304, 2003.

[111] Y. A. Vlasov and S. J. McNab. Losses in single-mode silicon-on-insulator strip waveguides and bends. *Optics Express*, 12(8):1622–1631, 2004.

[112] A. Fiore, S. Janz, L. Delobel, P. van der Meer, P. Bravetti, V. Berger, E. Rosencher, and J. Nagle. Second-harmonic generation at $\lambda = 1.6$ μm in AlGaAs/Al_2O_3 waveguides using birefringence phase matching. *Applied Physics Letters*, 72(23):2942–2944, 1998.

[113] J. B. Khurgin, M. W. Pruessner, T. H. Stievater, and W. S. Rabinovich. Suspended AlGaAs waveguides for tunable difference frequency generation in mid-infrared. *Optics Letters*, 33(24):2904–2906, 2008.

[114] C. Xiong, W. Pernice, K. K. Ryu, C. Schuck, K. Y. Fong, T. Palacios, and H. X. Tang. Integrated GaN photonic circuits on silicon (100) for second harmonic generation. *Optics Express*, 19(11):10462–10470, 2011.

[115] X. Yu, L. Scaccabarozzi, J. S. Harris, P. S. Kuo, and M. M. Fejer. Efficient continuous wave second harmonic generation pumped at 1.55 μm in quasi-phase-matched AlGaAs waveguides. *Optics Express*, 13(26):10742–10748, 2005.

[116] A. Chowdhury, H. M. Ng, M. Bhardwaj, and N. G. Weimann. Second-harmonic generation in periodically poled GaN. *Applied Physics Letters*, 83(6):1077–1079, 2003.